

Numerical Simulation of Baroclinic Jovian Vortices

Thesis by

Richard K. Achterberg

In Partial Fulfillment of the Requirements

for the Degree of

Doctor of Philosophy

California Institute of Technology

Pasadena, California

1992

(submitted 3 October 1991)

To my parents

Acknowledgements

I am deeply indebted to my thesis advisor, Professor Andrew Ingersoll, for introducing me to the subject of Jovian atmospheric dynamics, for his many suggestions of interesting research topics, and for the occasional necessary reminder that my computer models need to be compared with real observational data. This work would not have been possible without his advice, support and encouragement.

I also wish to thank my academic advisor, Professor Yuk Yung, for his advice over the years, and my first proposition advisor, Professor David Stevenson, for providing me with my first serious opportunity to do scientific research as a lowly first-year grad student. Many thanks are due to Bob Sharp, whose wonderful field trips around southern California (and Hawaii!) were one of the high points of my stay at Caltech.

I have received invaluable assistance from many of my fellow grad students. Special thanks go to Arie Grossman and Don Rudy for all of their aid in learning to use the department's computer facilities, and to Tim Dowling for many interesting and helpful discussions about Jovian atmospheric dynamics. A very big thank you also to Alden Consolver and Bridget Landry for helping me to retain my sanity over the last couple of years. Thank you also to Mark, Julie, Walter, Don B., Michelle, and all of the other grad students who helped to make my time at Caltech enjoyable.

A very big thank you goes to Kay Campbell and the rest of the administrative staff for all of their assistance in dealing with the administrative details of life at Caltech.

Last of all, and most importantly, I thank my parents for all of their encouragement and support, both emotional and financial.

Abstract

This thesis consists of two papers on the dynamics of Jovian planet atmospheres. The first paper discusses the uses of a normal-mode expansion in the vertical for modeling the dynamics of Jupiter's atmosphere. The second paper uses a non-linear numerical model based on the normal-mode expansion of the first paper to study the dynamics of baroclinic vortices. The abstracts for the two papers are reproduced below.

Paper 1:

We propose a non-linear, quasi-geostrophic, baroclinic model of Jovian atmospheric dynamics, in which vertical variations of velocity are represented by a truncated sum over a complete set of orthogonal functions obtained by a separation of variables of the linearized quasi-geostrophic potential vorticity equation. A set of equations for the time variation of the mode amplitudes in the non-linear case is then derived. We show that for a planet with a neutrally stable, fluid interior instead of a solid lower boundary, the barotropic mode represents motions in the interior, and is not affected by the baroclinic modes. One consequence of this is that a normal-mode model with one baroclinic mode is dynamically equivalent to a one layer model with solid lower topography. We also show that for motions in Jupiter's cloudy lower troposphere, the stratosphere behaves nearly as a rigid lid, so that the normal-mode model is applicable to Jupiter. We test the accuracy of the normal-mode model for Jupiter using two simple problems: forced, vertically propagating Rossby waves, using two and three baroclinic modes, and baroclinic instability, using two baroclinic modes. We find that the normal-mode model provides qualitatively correct results, even with only a very limited number of vertical degrees of freedom.

Paper 2:

We examine the evolution of baroclinic vortices in a time dependent, nonlinear numerical model of a Jovian atmosphere. The model uses a normal-mode expansion

in the vertical, using the barotropic and first two baroclinic modes (Achterberg and Ingersoll 1989). Our results for the stability of baroclinic vortices on an f -plane in the absence of a mean zonal flow are consistent with previous results in the literature, although the presence of the deep fluid interior on the Jovian planets appears to shift the stability boundaries to smaller length scales. The presence of a mean zonal shear flow acts to stabilize vortices against instability, significantly modifies the finite amplitude form of baroclinic instabilities, and combined with internal barotropic instability (Gent and McWilliams 1986) produces periodic oscillations in the latitude and longitude of the vortex as observed at the level of the cloud tops. This instability may explain some, but not all, observations of longitudinal oscillations of vortices on the outer planets. Oscillations in aspect ratio and orientation of stable elliptical vortices in a zonal shear flow are observed in this baroclinic model, as in simpler two-dimensional models (Kida 1981). The meridional propagation and decay of vortices on a β -plane is inhibited by the presence of a mean zonal flow. The direction of propagation of a vortex relative to the mean zonal flow depends upon the sign of the meridional potential vorticity gradient; combined with observations of vortex drift rates, this may provide a constraint on model assumption for the flow in the deep interior of Jupiter.

Table of Contents

Acknowledgments	iv
Abstract	v
Table of Contents	vii
List of Figures	vii
List of Tables	x
1. A Normal-Mode Approach to Jovian Atmospheric Dynamics	1
1. Introduction	5
2. Normal-Mode Model	7
3. Application of the Model to Jupiter	15
4. Test of Normal-Mode Model: Forced Rossby Waves	31
5. Test of Normal Mode Model: Baroclinic Instability	38
6. Conclusions	58
7. References	59
2. Numerical Simulation of Baroclinic Jovian Vortices	65
1. Introduction	69
2. Model Description	74
3. Vortices on an f -plane With No Zonal Flow	77
4. Effects of a Barotropic Mean Zonal Shear	110
5. Effects of β	156
6. Application to Jovian Planets	173
7. Appendix A: Energy in the Normal-Mode Model	196
8. References	200

List of Figures
Paper 1:

1.1 Temperature profiles for Jupiter's atmosphere.	16
1.2 Model static stability profile.	20

1.3	Reflection coefficients and response function for the standard model. . .	26
1.4	Vertical structure Φ_i for the first two peaks in the response function in the standard model	28
1.5	Reflection coefficients and response function for the standard model with an added NH_4SH cloud.	32
1.6	Reflection coefficients and response function for equilibrium hydrogen.	34
1.7	Velocity profiles used in baroclinic instability calculations	40
1.8	Contour plot of growth rates for $s = 1.769$	42
1.9	Contour plot of growth rates for $s = -0.214$	44
1.10	Contour plot of growth rates for $U = 79.5 \text{ m s}^{-1}$	46
1.11	Contour plot of growth rates for $U = -79.5 \text{ m s}^{-1}$	48
1.12	Phase speed and growth rates for $s = 1.769$, $U = 0.531 \text{ m s}^{-1}$	52
1.13	Phase speed and growth rates for $s = 1.769$, $k = 4.56 \times 10^{-3} \text{ km}^{-1}$	54
1.14	Phase speed and growth rates for $k = 1.69 \times 10^{-3} \text{ km}^{-1}$, $U = -79.5 \text{ m s}^{-1}$	56
Paper 2:		
2.1	Structure of the barotropic and first two baroclinic modes	78
2.2a	Example of horizontal fragmentation.	84
2.2b	86
2.3	Kinetic and potential energy as a function of time for the run shown in Fig. 2.2.	88
2.4a	Example of tripole formation.	90
2.4b	92
2.5	Kinetic and potential energy as a function of time for the run shown in Fig. 2.4.	94
2.6	Example of tripole formation for a vortex with the same sign of vorticity at all altitudes.	98
2.7	Example of vertical fragmentation.	100
2.8	Kinetic and potential energy as a function of time for the run shown in Fig. 2.7.	102
2.9	Regime diagram for the behavior of vortices on the f -plane with no mean	

zonal flow.	104
2.10a Example of a vortex rotating counter to the mean zonal flow.	112
2.10b	114
2.11a Example of a vortex rotating counter to the mean zonal flow at some altitudes.	116
2.11b	118
2.12 Shape and orientation oscillations of a stable vortex in a mean zonal shear.	120
2.13 Time variation of the energy conversion terms for a stable vortex in a mean zonal shear	122
2.14a Effect of mean zonal shear on horizontal fragmentation	126
2.14b	128
2.15 Time variation of the energy conversion terms for the case shown in Fig. 2.14.	130
2.16a Effect of mean zonal shear on tripole formation.	132
2.16b	134
2.17 Time variation of the energy conversion terms for the case shown in Fig. 2.16.	136
2.18a Effect of mean zonal shear on vertical fragmentation.	140
2.18b	142
2.19a Example of positional oscillations of a vortex.	144
2.19b Example of positional oscillations of a vortex.	146
2.20a Regime diagram for the behavior of vortices on an f -plane with mean zonal flow $U_0 = 0.5$	148
2.20b As Fig. 2.20a, but with $U_0 = 1.0$	150
2.21a Behavior of a vortex on a β -plane with no mean zonal shear flow.	158
2.21b Behavior of a vortex on a β -plane with a mean zonal shear flow	160
2.22 Effect of changing U_0 on the propagation and decay of vortices	162
2.23 Dominant terms contributing to the time rate of change of the first mode streamfunction $(\partial\psi_1/\partial t)$ for the stable vortex on a β -plane	166

2.24	Effect of changing β on the propagation and decay of vortices	168
2.25	Effect of changing λ_1^2 on the propagation and decay of vortices	170
2.26a	Latitude and longitude of the vortex for $\alpha = 0.5$, $\lambda_1^2 = 0.03$, $U_0 = 0.5$ and $\beta = 0.1$ as a function of time	174
2.26b	Latitude and longitude of the vortex for $\alpha = 0.5$, $\lambda_1^2 = 0.03$, $U_0 = 0.5$ and $\beta = 0.2$ as a function of time	176
2.27	Positional oscillations of Neptune's Second Dark Spot, compared with a model vortex.	182
2.28a	Positional oscillations of a perturbed vortex	184
2.28b	186
2.29	Trajectories of vortices in a mean zonal flow with curvature.	192

List of Tables

Paper 1:

1.1	Parameters of Jupiter Normal-Mode Models.	31
-----	--	----

Paper 2:

2.1	Parameters for Normal-Mode Model of Jupiter.	76
2.2	f -plane Simulations With No Zonal Flow.	106
2.3	f -plane Simulations with zonal flow.	152

Paper 1

A Normal-Mode Approach to Jovian Atmospheric Dynamics

A Normal-Mode Approach to Jovian Atmospheric Dynamics

Richard K. Achterberg and Andrew P. Ingersoll

Division of Geological and Planetary Sciences
California Institute of Technology
Pasadena, California 91125

Published in *Journal of the Atmospheric Sciences*
1 August 1989

Contribution number 4721 from the Division of Geological and Planetary Sciences,
California Institute of Technology, Pasadena, California 91125.

Abstract

We propose a non-linear, quasi-geostrophic, baroclinic model of Jovian atmospheric dynamics, in which vertical variations of velocity are represented by a truncated sum over a complete set of orthogonal functions obtained by a separation of variables of the linearized quasi-geostrophic potential vorticity equation. A set of equations for the time variation of the mode amplitudes in the non-linear case is then derived. We show that for a planet with a neutrally stable, fluid interior instead of a solid lower boundary, the barotropic mode represents motions in the interior, and is not affected by the baroclinic modes. One consequence of this is that a normal-mode model with one baroclinic mode is dynamically equivalent to a one layer model with solid lower topography. We also show that for motions in Jupiter's cloudy lower troposphere, the stratosphere behaves nearly as a rigid lid, so that the normal-mode model is applicable to Jupiter. We test the accuracy of the normal-mode model for Jupiter using two simple problems: forced, vertically propagating Rossby waves, using two and three baroclinic modes, and baroclinic instability, using two baroclinic modes. We find that the normal-mode model provides qualitatively correct results, even with only a very limited number of vertical degrees of freedom.

1.1. Introduction

Numerical models of Jupiter's zonal jets and large circulating ovals generally focus on horizontal structure. The vertical structure of wind and pressure, and interactions with Jupiter's fluid interior, are either ignored or handled with simplifying assumptions. For example, the 1-layer models (Williams 1975; Maxworthy and Redekopp 1976; Williams and Yamagata 1984; Williams and Wilson 1988) have only a single degree of freedom in the vertical. The $1\frac{1}{2}$ layer models (Ingersoll and Cuong 1981; Marcus 1988; Dowling and Ingersoll 1988,1989) have only one degree of freedom associated with a thin upper weather layer. Latitudinally varying bottom topography simulates the steady zonal motions in a much deeper, adiabatic lower layer, but only the top layer motions are free to change. Other models (Williams 1979; Read and Hide 1984; Read 1986) have two or more vertical degrees of freedom, but assume a flat, rigid lower boundary. The upper boundary condition — expressing the fact that the density approaches zero at the top of the atmosphere — is not adequately treated in any of the models. Not only are the models quantitatively inaccurate, but they fail qualitatively to simulate many important processes such as baroclinic instability and vertical propagation of energy. For instance, Gierasch *et al.* (1979) and Conrath *et al.* (1981) have shown that the presence or absence of the deep lower layer has a large effect on the growth rates of baroclinic instabilities, indicating that a baroclinic model of Jupiter needs the proper lower boundary condition.

The sources of the deficiencies are both observational and conceptual. The visible and infrared observations of the Jovian planets (summarized by Ingersoll *et al.* 1984) provide detailed information down to cloud top levels (500 to 700 mbar). Winds are defined by tracking clouds in *Voyager* images (Ingersoll *et al.* 1981; Mitchell *et al.* 1981; Hatzes *et al.* 1981; Limaye *et al.* 1982; Limaye 1986; Mac Low and Ingersoll 1986; Dowling and Ingersoll 1988). Infrared observations measure the abundances of water,

ammonia and other gases for pressures less than about 5 bars (Conrath and Gierasch 1986; Bjoraker *et al.* 1986a,b), and provide information about the thermal structure above the cloud tops (Gierasch *et al.* 1986). The *Voyager* radio occultation experiment probed the region from 1 mbar to 1000 mbar (Lindal *et al.* 1981), providing profiles of temperature vs. pressure, but no direct information about winds. Below the ammonia clouds one must rely on wet and dry adiabatic extrapolations, using cosmochemical and spectroscopic estimates for the amount of water and other condensables (Pollack *et al.* 1986; Bjoraker *et al.* 1986a,b). The net effect of these uncertainties has been to discourage investigators from examining the conceptual problems associated with the upper and lower boundary conditions. We wish to rectify this situation. Our goal is to develop a framework for systematically introducing multiple degrees of freedom in the vertical into models of large-scale Jovian atmospheric dynamics. The effect of observational uncertainties can be explored systematically. In this paper, we treat only the simplest dynamical problems, using them as a test of our model. In a later paper we will apply the framework to a non-linear time-dependent numerical model of the Great Red Spot and its interactions with the zonal jets.

We propose a normal-mode (Galerkin) approach to the three-dimensional (baroclinic) quasi-geostrophic (QG) equations, assuming that the stably-stratified section of atmosphere being modeled lies on top of an infinitely deep, adiabatic fluid, which is allowed to have a zonal flow. This deep fluid provides a simple description for the effects of Jupiter's interior on the atmosphere. Vertical variations of the horizontal streamfunction are represented by a summation over orthogonal eigenfunctions resulting from a separation of variables on the linearized QG potential vorticity equation. The QG equations are more restrictive than the primitive equations, yet they are the starting point for much of terrestrial meteorology. The required assumptions are no less plausible for Jupiter than for the Earth, and certainly apply to many

Jovian phenomena. We believe that these well-studied equations provide the best starting point for introducing multiple degrees of freedom in the vertical for models of Jupiter's atmosphere.

The advantages of the normal-mode model over the more common layer model are explained in detail by Flierl (1978). A major advantage of the former is that its derivation also produces a straightforward method for determining the model parameters given the vertical thermal structure of the atmosphere. For a layer model, on the other hand, the model parameters (thickness and density of the layers) are not uniquely determined for a given continuous vertical structure. Furthermore, a layer model does not accurately represent non-linear interactions of baroclinic structures (Flierl 1978).

This paper is organized as follows. In Section 1.2 we derive the equations for the normal-mode model, and discuss the lower boundary condition. Section 1.3 describes the vertical structure of Jupiter's atmosphere, and discusses the applicability of the normal-mode approach and the effect of the upper boundary condition. Sections 1.4 and 1.5 test our normal-mode model by solving simple problems using both the normal-mode model and a continuous vertical structure. These tests demonstrate that a normal-mode model is applicable to the study of large-scale Jovian atmospheric dynamics.

1.2. Normal-Mode Model

Our model is based on the quasi-geostrophic (QG) equation for conservation of potential vorticity on a β -plane in log-pressure coordinates (e.g., Gill 1982; Pedlosky 1987):

$$\frac{D}{Dt} (\nabla^2 \psi + \beta y + \mathcal{L}\psi) = 0, \quad (1.1)$$

where

$$\begin{aligned}\mathcal{L}a &= e^z \frac{\partial}{\partial z} \left(\frac{e^{-z}}{L_D^2} \frac{\partial a}{\partial z} \right), \\ \frac{Da}{Dt} &= \frac{\partial a}{\partial t} + J(\psi, a), \\ J(a, b) &= \frac{\partial a}{\partial x} \frac{\partial b}{\partial y} - \frac{\partial a}{\partial y} \frac{\partial b}{\partial x}.\end{aligned}\tag{1.2}$$

Here ψ is the geostrophic streamfunction, D/Dt is the advective derivative, $z \equiv -\ln(p/p_1)$ with p_1 a reference pressure level, $L_D(z) = NH/f_0$ is the local internal deformation radius, N is the Brunt-Väisälä frequency, $H = RT/g$ is the pressure scale height, T is the temperature, R is the gas constant, g is the gravitational acceleration, and $f = f_0 + \beta y$ is the Coriolis parameter.

The important assumptions implicit in this QG formulation are: $H/L \ll 1$ where H and L are characteristic vertical and horizontal length scales respectively, $U/fL \ll 1$ where U is a characteristic horizontal velocity, and $L/U\tau \ll 1$ where τ is a characteristic time for radiative and viscous dissipation. One further assumes that the frequencies are no larger than U/L and that the scale L is small compared to the planetary radius. The QG equations are usually derived under the assumption $L \sim L_D$, but the case $L_D \rightarrow 0$ can be handled with suitable upper and lower boundary conditions (see Eqs. 1.6 – 1.12 below).

Following Gavrilin (1965) and Flierl (1978), we separate out the vertical structure and write the streamfunction in the form

$$\psi(x, y, z, t) = \sum_{n=0}^N \psi_n(x, y, t) \Phi_n(z),\tag{1.3}$$

where the functions $\Phi_n(z)$ are solutions to the equation

$$\mathcal{L}\Phi_n + \lambda_n^2 \Phi_n = 0.\tag{1.4}$$

Boundary conditions are applied at z_0 and z_2 . Equation (1.4) gives the vertical structure of a Rossby wave with deformation radius λ_n^{-1} (Pedlosky 1987). Substituting

(1.3) and (1.4) into (1.1), multiplying by $e^{-(z-z_1)}\Phi_n dz$, and integrating from z_0 to z_2 , we obtain a set of coupled equations for the ψ_n :

$$\sum_{m=0}^N \delta_{mn} \left[\frac{\partial}{\partial t} (\nabla^2 \psi_m - \lambda_m^2 \psi_m) + \beta \frac{\partial \psi_m}{\partial x} \right] + \sum_{l,m=0}^N \gamma_{lmn} J(\psi_l, \nabla^2 \psi_m - \lambda_m^2 \psi_m) = 0, \quad (1.5)$$

where

$$\delta_{mn} = \int_{z_0}^{z_2} e^{-(z-z_1)} \Phi_m \Phi_n dz,$$

$$\gamma_{lmn} = \int_{z_0}^{z_2} e^{-(z-z_1)} \Phi_l \Phi_m \Phi_n dz.$$

We assume that the Φ_n are normalized so that $\delta_{nn} = 1$, and we define a reference level z_1 in the range $z_0 < z_1 < z_2$.

Application of this model is complicated by the lack of solid upper and lower boundaries. We focus on a thin, stably-stratified, weather layer ($z_1 < z < z_2$) that rests hydrostatically on a much thicker, neutrally-stratified interior layer ($z_0 < z < z_1$). For the upper boundary condition ($z = z_2$) we show in the next section that Jupiter's upper troposphere and stratosphere ($p \lesssim 700$ mbar) act almost as a rigid lid, reflecting ≈ 90 percent of the energy propagating upward from below. Accordingly, we implement the normal-mode model with a rigid lid at $p = p_2 \approx 700$ mbar. The bulk of the paper is devoted to testing the normal-mode and rigid lid assumptions by comparing solutions with these approximations to solutions of the continuous equations with an outgoing wave (radiation boundary condition) assumed at the top of the stratosphere ($p = 1$ mbar).

For the lower boundary condition ($z = z_0$), we assume that vertical motions are zero or suitably bounded at the base of the deep interior layer, whose thickness ($z_1 - z_0$) is much greater than the thickness of the upper weather layer ($z_2 - z_1$). As we will show, solving (1.4) under these assumptions yields a barotropic ($n = 0$) mode with $\lambda_0^2 = 0$ and $\Phi_0 = \text{constant}$ in $z_0 < z < z_2$, plus a set of baroclinic ($n \geq 1$) modes with $\lambda_n^2 > 0$ and non-zero amplitude $\Phi_n \neq 0$ only in the weather layer $z_1 < z < z_2$.

In other words, the appropriate boundary condition on the baroclinic modes at the base of the weather layer ($z = z_1$) is $\Phi_n = 0$.

This boundary condition for the baroclinic modes was discussed by Gierasch *et al.* (1979) and Conrath *et al.* (1981), although they did not consider a barotropic mode which extends into the deep adiabatic region below. Setting the barotropic mode to zero is equivalent to assuming solid-body rotation in Jupiter's interior up to the base of the water cloud (or other source of static stability). More general assumptions include steady, zonal flow $\psi_0 = \psi_0(y)$, or the even more general time-dependent motions of a rotating, isentropic, spherical, fluid body (e.g., Busse 1976; Ingersoll and Pollard 1982; Ingersoll and Miller 1986).

Since the lower boundary condition for the baroclinic modes of the weather layer is crucial to what follows, we repeat the arguments of Gierasch *et al.* (1979) for the β -plane, focussing not on the dynamics of the lower region but rather on its effects at the base of the weather layer. To treat the case $L_D \rightarrow 0$, we decompose (1.1) into the QG vorticity equation and the thermodynamic energy equation:

$$\frac{D}{Dt}(\nabla^2\psi + \beta y) - f_0 e^z \frac{\partial}{\partial z}(e^{-z}w) = 0, \quad (1.6)$$

$$\frac{D}{Dt}\left(\frac{\partial\psi}{\partial z}\right) + f_0 L_D^2 w = 0. \quad (1.7)$$

Here $w = dz/dt$ is the vertical velocity in log-pressure coordinates. Consider a small-amplitude disturbance whose amplitude varies as $\exp(ikx + ily + i\omega t)$. Equations (1.6) and (1.7) then become:

$$i\omega\lambda^2\psi - f_0 e^z \frac{\partial}{\partial z}(e^{-z}w) = 0, \quad (1.8)$$

$$i\omega \frac{\partial\psi}{\partial z} + f_0 L_D^2 w = 0, \quad (1.9)$$

$$\lambda^2 = \left(\frac{k\beta}{\omega}\right) - (k^2 + l^2). \quad (1.10)$$

These equations are equivalent to (1.4), but λ^2 is now a separation constant that depends upon the frequency and horizontal wavenumber.

For the lower region where $L_D^2 = 0$, (1.9) says that $\partial\psi/\partial z = 0$. We exclude the possibility $\omega = 0$, $\partial\psi/\partial z \neq 0$ as it leads to infinitely small-scale oscillations ($\lambda^2 \rightarrow \infty$) in the upper weather layer according to (1.4) and (1.10). With $\psi = \text{constant}$, (1.8) yields

$$w = \frac{i\omega\lambda^2\psi}{f_0} [\exp(z - z_0) - 1] \quad \text{for } z_0 \leq z \leq z_1, \quad (1.11)$$

where we have used the lower boundary condition $w = 0$ at $z = z_0$. At the base of the weather layer ψ and w are continuous, although $\partial\psi/\partial z$ and L_D^2 may be discontinuous. Thus at $z = z_1$ we combine (1.9) and (1.11) to yield

$$\left. \frac{\partial\psi}{\partial z} \right|_{z=z_1} + \lambda^2 L_D^2 [\exp(z_1 - z_0) - 1] \psi|_{z=z_1} = 0. \quad (1.12)$$

This is the required boundary condition at $z = z_1$ for small-amplitude QG motions in the weather layer. The barotropic mode satisfies (1.12) with $\lambda^2 = 0$ and $\partial\psi/\partial z = 0$. The lowest baroclinic modes have a small number of vertical oscillations in the upper weather layer and therefore have $\lambda^2 L_D^2 \sim 1$. However, the great depth of the lower layer means that the exponential in (1.12) is large. This implies that the baroclinic modes have $\psi = 0$ at $z = z_1$, as discussed earlier.

The above results lead to simplifications of Eq. (1.5). The baroclinic modes have $\Phi_n = 0$ at $z = z_1$, and $\partial\Phi_n/\partial z = 0$ at $z = z_2$ which follows from (1.9) with a rigid lid ($w = 0$) at the upper boundary. Thus (1.4) is a Sturm-Liouville system in $z_1 < z < z_2$, with discrete eigenvalues λ_n and orthogonal eigenfunctions Φ_n for $n \geq 1$. The constant δ_{mn} is either 0 or 1, depending upon whether $m \neq n$ or $m = n$, respectively. For the baroclinic modes, the integrals in the definitions of δ_{mn} and γ_{lmn} can be taken from z_1 to z_2 . The magnitudes of the Φ_n will be of order unity if $z_2 - z_1$ is of order unity. Setting the barotropic eigenfunction Φ_0 equal to unity then ensures that all of the eigenfunctions are of the same magnitude in $z_1 < z < z_2$.

The equation for the barotropic mode amplitude $\psi_0(x, y, t)$ is obtained from (1.5) by setting $n = 0$. The integrals go from z_0 to z_2 . With $\Phi_0 = 1$ we have

$\delta_{00} = \gamma_{000} \gg 1$. All the other constants δ_{m0} and γ_{lm0} are of order unity and may be neglected. Since $\lambda_0^2 = 0$ we are left with

$$\frac{\partial}{\partial t} (\nabla^2 \psi_0) + \beta \frac{\partial \psi_0}{\partial x} + J(\psi_0, \nabla^2 \psi_0) = 0, \quad (1.13)$$

which is the usual potential vorticity equation for a barotropic fluid with a rigid lid. Thus the barotropic mode is unaffected by the presence of baroclinic modes (or equivalently, the weather layer does not affect the interior), although the barotropic mode will affect the baroclinic modes.

The separation into a single barotropic mode and set of baroclinic modes with $\psi = 0$ at $z \leq z_1$ does not require a rigid lower boundary at $z = z_0$. A scaling analysis of the non-linear equation (1.6) gives the same result. The argument was given by Ingersoll and Cuong (1981) in the discussion of the $1\frac{1}{2}$ layer model. If the magnitude of w is everywhere consistent with QG scaling in the weather layer, then the great depth of the lower layer implies that the term involving $\partial/\partial z$ in (1.6) is negligible in the lower layer. This leaves

$$\frac{\partial}{\partial t} (\nabla^2 \psi) + \beta \frac{\partial \psi}{\partial x} + J(\psi, \nabla^2 \psi) = 0, \quad (1.14)$$

which is the equation for the barotropic mode derived above. Thus the full equation in the interior region is satisfied by the barotropic mode alone. The baroclinic component of the solution is confined to the upper layer. Continuity of ψ then requires $\Phi_n = 0$ at $z = z_1$ for $n \geq 1$.

A final derivation of the lower boundary condition is given in Section 4 of Gierasch *et al.* (1979). They include non-hydrostatic and ageostrophic effects in the lower layer. Equation (1.1) still holds in the upper layer, since frequencies are small compared to f_0 , and $L \sim L_D$. The motion in the lower layer is a downward-propagating wave whose vertical wavelength is large compared to the horizontal wavelength. The vertical wavelength is therefore much larger than the upper layer thickness ($z_2 - z_1$). A parameter analogous to the ratio of lower layer thickness to upper

layer thickness is large when the frequencies are small. The argument resulting in (1.12) is shown to hold for the non-hydrostatic case as well as for the hydrostatic case.

The derivations of the lower boundary condition by Gierasch *et al.* (1979) treat the adiabatic interior as an infinitely deep constant density fluid on a β -plane, ignoring effects of compressibility and spherical geometry. Our derivation is quasi-geostrophic and ignores ageostrophic and non-hydrostatic effects. The general problem of how the neutrally stable fluid interior of a Jovian planet interacts with the stably stratified atmosphere is poorly understood, and further work is needed in this area.

The equations for the baroclinic mode amplitudes $\psi_n(x, y, t)$ are obtained from (1.5) with $n \geq 1$. A complication arises because the barotropic mode is not orthogonal to the baroclinic modes in $z_1 < z < z_2$. Thus we have $\delta_{0n} = \gamma_{00n} \neq 0$. However, the terms that involve these constants cancel because of (1.13). In fact, the only terms involving ψ_0 in (1.5) are from the double sum with one of the summation indices equal to n and the other equal to zero. This follows from $\Phi_0 = 1$, whence $\gamma_{0mn} = \delta_{mn}$ which is zero unless $m = n$. With these special cases taken into account, the equation for the n^{th} baroclinic mode is

$$\begin{aligned} \frac{\partial}{\partial t} (\nabla^2 \psi_n - \lambda_n^2 \psi_n) + \beta \frac{\partial \psi_n}{\partial x} + J(\psi_0, \nabla^2 \psi_n - \lambda_n^2 \psi_n) + J(\psi_n, \nabla^2 \psi_0) \\ + \sum_{l,m=1}^N \gamma_{lmn} J(\psi_l, \nabla^2 \psi_m - \lambda_m^2 \psi_m) = 0. \end{aligned} \quad (1.15)$$

An energy equation can be obtained by multiplying (1.15) by ψ_n , integrating over x and y , and summing over the modes n . Assuming periodic boundary conditions in x , and either periodicity in y or $\partial\psi/\partial x = 0$ and $\partial^2\bar{\psi}/\partial t\partial y = 0$ at $y = y_1$ and $y = y_2$ (Holton 1979), where $\bar{\psi}$ is the x average of ψ , we obtain

$$\frac{\partial}{\partial t} \sum_n \iint \frac{1}{2} (|\nabla \psi_n|^2 + \lambda_n^2 \psi_n^2) dA = - \sum_n \iint \psi_0 \frac{\partial}{\partial y} \left(\frac{\partial \psi_n}{\partial x} \nabla^2 \psi_n \right) dA. \quad (1.16)$$

The integrand of the left hand side of (1.16) represents the total energy of mode n , while the right hand side describes the conversion of energy from the barotropic mode to the baroclinic modes. This term has the same form as the conversion from mean kinetic energy to eddy kinetic energy (Holton 1979), although our baroclinic modes can have a mean part. Also, our barotropic mode has such large inertia that its amplitude does not change during the interaction.

As we are interested only in the behavior of the weather layer, we do not solve (1.14), but instead make a general assumption which guarantees that it is satisfied. Since $\psi_0 = \psi_0(y)$ is an exact solution of (1.14), we assume that the motion in the deep interior, which corresponds to the barotropic mode, is steady and zonal (solid-body rotation is a special case of this). Although more complicated interior motions, which are not solutions of (1.14) but follow a more general equation for flow in a rotating sphere, are possible, we do not consider them in the context of this model. Regardless of the appropriate equation, a steady zonal flow is likely to be a possible solution for the motions in the interior.

Equation (1.15) may be truncated at any $N \geq 1$. The normal-mode model with $N = 1$ is dynamically equivalent to the reduced gravity single layer model considered by Ingersoll and Cuong (1981). This equivalence may then be used to relate the single layer model to observations. To show this we set $N = 1$ in (1.15) with $\psi_0 = \psi_0(y)$. The equation for a single baroclinic mode then becomes

$$\frac{\partial}{\partial t} (\nabla^2 \psi_1 - \lambda_1^2 \psi_1) + \beta \frac{\partial \psi_1}{\partial x} + J(\psi_0, \nabla^2 \psi_1 - \lambda_1^2 \psi_1) + J(\psi_1, \nabla^2 \psi_0 + \gamma_{111} \nabla^2 \psi_1) = 0. \quad (1.17)$$

Defining $\hat{\psi} = \psi_0 + \gamma_{111} \psi_1$ and $\lambda = \lambda_1$, (1.17) can be manipulated into the form

$$\frac{\partial}{\partial t} (\nabla^2 \hat{\psi} - \lambda \hat{\psi}) + \beta \frac{\partial \hat{\psi}}{\partial x} + J(\hat{\psi}, \nabla^2 \hat{\psi} - \lambda^2 \hat{\psi} + \lambda^2 \psi_0) = 0, \quad (1.18)$$

which is the equation of motion for the single layer model of Ingersoll and Cuong (1981), where $\hat{\psi}$ is the streamfunction in the thin upper layer, ψ_0 is the streamfunction

for the deep lower layer, and λ^{-1} is the deformation radius for the upper layer. This correspondence allows us to relate the radius of deformation and velocity in the single layer model to observations. The observed streamfunction ψ_{obs} is then related to the normal-mode model by

$$\psi_{\text{obs}} = \psi_0 \Phi_0(z_{\text{obs}}) + \psi_1 \Phi_1(z_{\text{obs}}), \quad (1.19)$$

where z_{obs} is the level of the observations and $\Phi_0(z) = 1$. Substituting $\psi_1 = (\hat{\psi} - \psi_0)/\gamma_{111}$ gives

$$\psi_{\text{obs}} = \frac{\Phi_1(z_{\text{obs}})}{\gamma_{111}} \hat{\psi} + \left(1 - \frac{\Phi_1(z_{\text{obs}})}{\gamma_{111}}\right) \psi_0. \quad (1.20)$$

In the next section, we find $\gamma_{111} \approx 1.17$ and $\Phi_1(z_{\text{obs}}) \approx 1.22$ for our standard model of Jupiter's atmosphere described in the next section. This implies that the velocities for the upper layer of a single layer model, computed from $\hat{\psi}$, may be compared directly to velocities observed on Jupiter, with an error of around 5 percent. This simple correspondence between layer and normal-mode models only holds with one baroclinic mode, since in general a N -mode model has more free parameters than a N -layer model. (Flierl 1978, discusses the general problem of calibrating layer models). The single layer model (1.18) conserves an energy-like quantity — the global integral of $\frac{1}{2} (|\nabla \hat{\psi}|^2 + \lambda^2 \hat{\psi}^2)$. This conservation law holds in addition to (1.16) with $N = 1$, but it does not seem to extend to $N \geq 2$.

1.3. Application of the Model to Jupiter

Knowledge of the vertical temperature structure allows us to apply this model to Jupiter. The crucial parameter is the Brunt-Viäsälä frequency $N(z)$, which enters through the local deformation radius $L_D(z) = NH/f_0$ in (1.2) and (1.4). The solutions of (1.4) determine the λ_n and γ_{lmn} according to (1.5), and these constants uniquely define the planet in the normal-mode equation (1.15).

Figure 1.1. Temperature profiles for Jupiter's atmosphere. The open circles are from the *Voyager 2* radio occultation egress data, the asterisks are from the *Voyager 2* radio occultation ingress data, and the solid line is the profile used in our models.

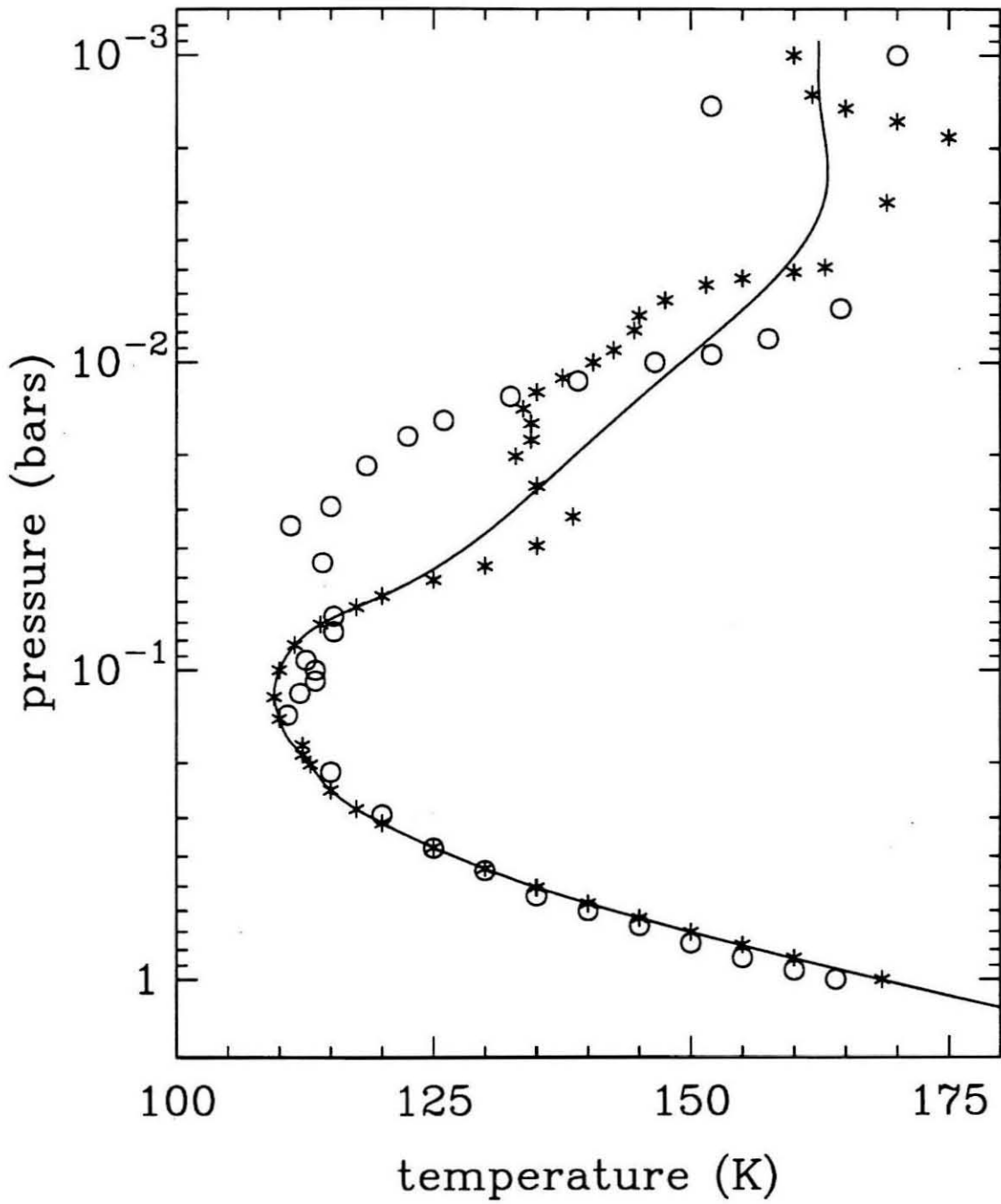


Figure 1.1 shows the temperature profiles measured during the *Voyager* radio occultation experiments (Lindal *et al.* 1981), which cover the pressure range from 1 mbar to 1000 mbar, along with the temperature profile used in our calculations. We used the radio occultation profile for $p < 690$ mbar, and a moist pseudoadiabat (discussed below) for $p > 690$ mbar. The observed cloud-tracked winds refer to the range from approximately 500 mbar to 1000 mbar. This is the location of the ammonia cloud, which is calculated to overlie deeper cloud layers of ammonium hydrosulfide and water (e.g., Weidenschilling and Lewis 1973). The base of the water cloud lies at 3–6 bars, depending upon the water abundance. Below this cloud, the temperature is thought to follow a dry adiabat, reflecting the fact that sunlight does not penetrate into the layers below, and the only source of energy is heat from Jupiter's interior.

Our fundamental assumption is that the observed winds are the surface manifestation of barotropic and baroclinic motions that extend from the ammonia cloud down to the base of the water cloud. This is the weather layer of the previous section. The static stability of the layer, from which $N(z)$ and $L_D(z)$ are derived, is taken to be the difference between the assumed temperature profile and a dry adiabat. Justification for the last assumption comes from the earth's tropics, which are near neutral stability for moist convection, but whose large-scale motions are apparently governed by dry adiabatic processes (e.g., Holton 1979; Gill 1982). This assumption has been applied to Jupiter and Saturn in the past (e.g., Barcilon and Gierasch 1970; Allison and Stone 1983), but there are no direct observations to confirm or deny it.

The Brunt-Viäsälä frequency is expressed in terms of the virtual temperature $T_V(T, p)$ as follows:

$$N^2 = \frac{g^2}{R_d T_V^2} \left(\frac{dT_V}{dz} + \frac{R_d T_V}{C_p(d)} \right), \quad (1.21)$$

where

$$T_V = T/[1 + (\epsilon - 1)e(T)/p]. \quad (1.22)$$

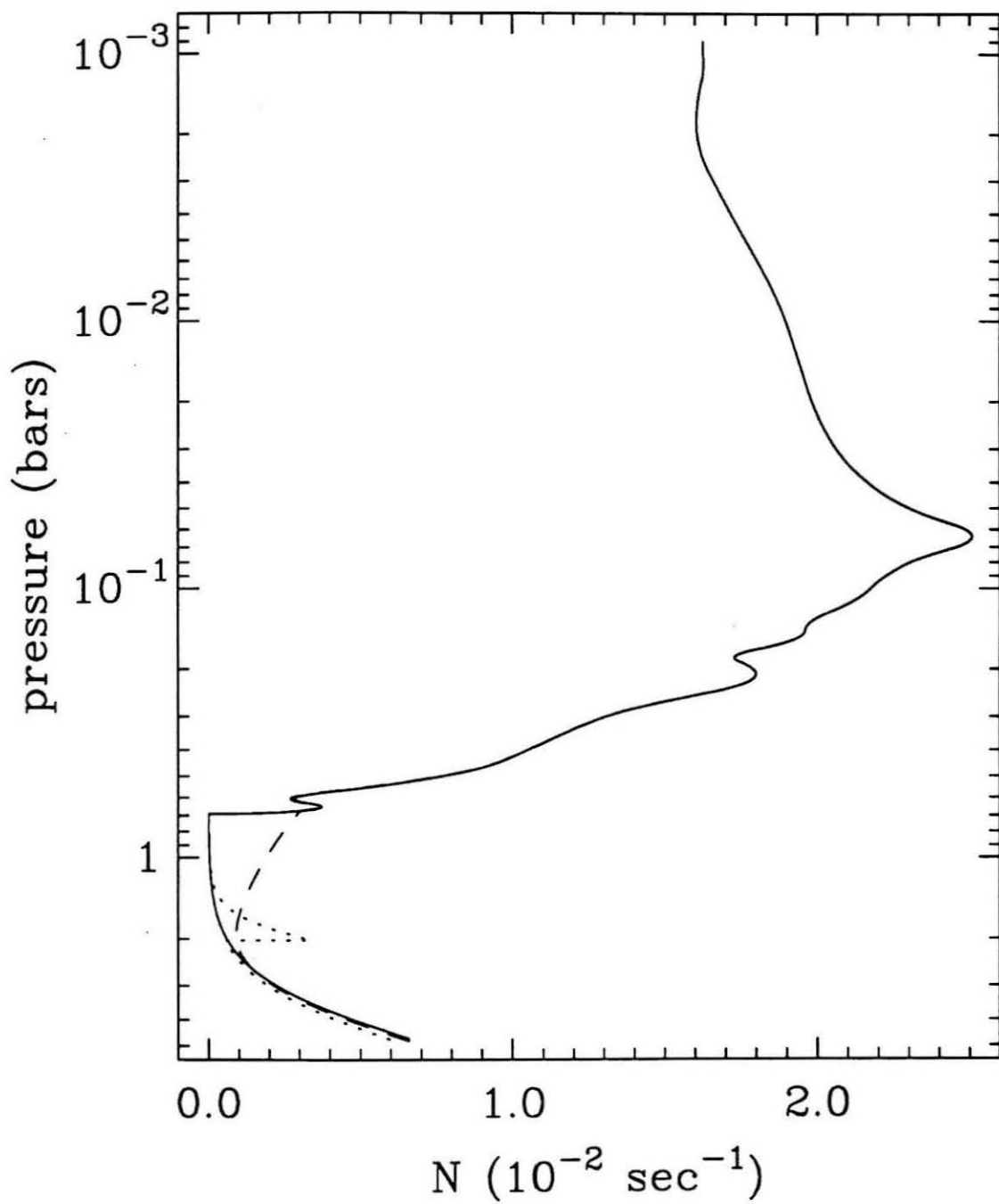
Here R_d is the gas constant of the dry atmosphere, $\epsilon = m_v/m_d$ is the ratio of the molecular weight of water vapor to that of the dry atmosphere, $e(T)$ is the saturation vapor pressure of the condensate, $C_p(d)$ is the specific heat of the dry atmosphere, and $z = -\ln(p/p_1)$ as before. The relation between T and z is taken to be a moist pseudoadiabat, in which moisture is removed as soon as it condenses. Thus we have (e.g., Weidenschilling and Lewis 1973)

$$\frac{dT}{dz} = \frac{RT}{C_p} \frac{\left(1 + \frac{Lf_m}{RT}\right)}{\left(1 + \frac{L^2\epsilon f_m}{RC_p T^2}\right)}, \quad (1.23)$$

where R and C_p are the gas constant and specific heat of the saturated mixture, respectively, L is the latent heat per unit mass of the vapor, and f_m is the mass fraction of water vapor in the saturated atmosphere. With these definitions, N^2 is the difference between $g(d \ln \rho/dh)$ for moist and dry adiabatic processes, respectively, where h is the height in dimensional units. The idea is that the first term in (1.21) represents the temperature profile of the atmosphere, which is set by rapid convective motions occupying only a small fraction of the total surface area. This is analogous to cumulus convection in the Earth's tropics (Riehl and Malkus 1958; Palmén and Newton 1969). The presence of cumulus convection occupying a small fraction of the surface area was used by Lunine and Hunten (1987) to reconcile the observed low water abundance on Jupiter with the abundance predicted by models of planetary formation. The second term represents the collective behavior of the gas during relatively slow, large-scale motions.

The dry gas is assumed to be 89 percent hydrogen and 11 percent helium by volume. Our standard model has water vapor as the only condensable, owing to its relatively large abundance and dominant contribution to the latent heat. The base of the water cloud occurs where the saturation vapor pressure divided by the total pressure is equal to the subcloud mixing ratio. The cloud base is defined to be the

Figure 1.2. Model static stability profile. The solid line is for the standard model. The dotted line is for the standard model with an NH_4SH cloud. The dashed line is for equilibrium hydrogen.



bottom of the weather layer ($z = z_1$) discussed in the preceding section. For comparison with the standard model, we added the effect of an ammonium hydrosulfide (NH_4SH) cloud layer, which is predicted by chemical equilibrium calculations of the cloud structure (Lewis 1969; Weidenshilling and Lewis 1973), although the observational data are inconclusive (e.g., West *et al.* 1986). The NH_4SH cloud produces a small spike in the N^2 profile between 1.3 and 2 bars, as shown in Fig. 1.2, but little change at other pressures. The probable ammonia cloud occurs at pressures less than 700 mbar, where we are using the radio occultation data to determine the temperature structure.

Another problem in calculating the static stability of Jupiter's atmosphere is that the specific heat of hydrogen depends upon the ratio of *ortho*-hydrogen (parallel proton spin vectors) to *para*-hydrogen (anti-parallel proton spins), and the rate at which equilibration between the two forms occurs (Massie and Hunten 1982; Conrath and Gierasch 1984). In our models, we assume that the *ortho*-hydrogen and *para*-hydrogen are in thermal equilibrium; this assumption is consistent with the Voyager IRIS data for Jupiter (Conrath and Gierasch 1984). The rate at which equilibration occurs is also important, as it determines if the heat released from conversion of *ortho*-hydrogen to *para*-hydrogen affects the temperature gradient. For frozen equilibrium hydrogen, the heat of conversion is ignored, while for equilibrium hydrogen it is included. The conditions under which each of these assumptions holds are discussed in detail by Conrath and Gierasch (1984). One necessary condition for the equilibrium case to hold — that the convective time scale be at least as long as the equilibration time (one month or longer) — seems at odds with the Voyager imaging sequences. Calculations of the heat of conversion are given by Massie and Hunten (1982). As shown in Fig. 1.2, the equilibrium case has a larger Brunt-Viäsälä frequency than the frozen equilibrium case. For Jupiter, the difference in temperature gradient between

the equilibrium and frozen equilibrium cases is smaller than the errors in measurement of the temperature gradient, so that either case is possible. On Uranus, however, the lower temperature produces a larger difference between the equilibrium and frozen equilibrium adiabats, and the observed temperature profiles are consistent only with frozen equilibrium (Gierasch and Conrath 1987). We therefore use frozen equilibrium in our standard model, although the equilibrium case is sometimes used for comparison. Since it has been suggested that the temperature gradient in Jupiter's lower troposphere is intermediate between the wet and dry adiabats, we also considered a model in which N^2 is one-half of the wet adiabatic value.

The final obstacle in applying the normal-mode model to Jupiter is the upper boundary condition. An ideal boundary condition would account for all possible processes occurring above the top of the modeled region, and is not feasible. If we assume that there are no mechanical energy sources or partially reflecting layers above the top of the model so that all energy leaving out the top escapes, and that any interactions between modes above the top of the modeled region are negligible, we may use the radiation condition: there is no downward directed energy flux at the top of the model. The radiation condition is still unwieldy with our normal-mode model since the radiation condition will not in general allow normal modes with real eigenvalues λ_n and orthogonal eigenfunctions Φ_n . To obtain real eigenvalues and orthogonal eigenfunctions, we assume the rigid lid boundary condition $d\Phi_n/dz = 0$ (Pedlosky 1987). A rigid lid, however, has the side effect of reflecting energy incident upon it (Lindzen *et al.* 1967). But if the atmosphere without the lid has a level at or below which a large amount of upwardly propagating energy is reflected back down, the region below this level will behave essentially like an atmosphere with a lid, and the use of an artificial lid is justified. We may thus test the rigid lid approximation by calculating how well the model atmosphere with the outgoing wave upper boundary

condition traps vertically propagating energy. This is done in several ways. The first is by calculating how well upward propagating waves are reflected back downward by the upper atmosphere as measured by a reflection coefficient. The second is by determining if there are almost-resonant modes at discrete λ_n . Other tests, involving forced Rossby waves and baroclinic instability are discussed in the next two sections.

To implement the radiation condition, we assume constant temperature above 1 mbar (where the *Voyager* radio occultation data ends), and note that the general solution to (1.4) in this isothermal region is then

$$\Phi_n = A \exp\left(\left(\frac{1}{2} + iq\right)z\right) + B \exp\left(\left(\frac{1}{2} - iq\right)z\right), \quad (1.24)$$

where A and B are complex constants and

$$q = (\lambda_n^2 L_D^2 - \frac{1}{4})^{1/2},$$

with L_D a constant. If we calculate the energy flux for this solution, we find that the first term corresponds to an upward energy flux and the second term to a downward energy flux, so that we need $B = 0$. Taking the ratio of Φ_n to $\partial\Phi_n/\partial z$, we obtain the upper boundary condition for a purely outgoing wave:

$$\frac{\partial\Phi_n}{\partial z} = \left(\frac{1}{2} + iq\right)\Phi_n. \quad (1.25)$$

Calculation of reflection coefficients is done by a method similar to that used by Halevy and Peltier (1985) for barotropic waves. We assume a purely outgoing wave at 1 mbar, and determine the ratio of the downward to upward wave amplitude at $z = z_1$. This ratio is defined as the reflection coefficient \mathcal{R} . Since \mathcal{R} is the ratio of wave amplitudes, the fraction of energy which is reflected is given by \mathcal{R}^2 . To calculate \mathcal{R} , we integrate (1.4) down from 1 mbar, with (1.25) as the upper boundary condition, to the base of the water cloud using a fourth order Runge-Kutta method. An artificial region with constant $L_D = L_D(z_1)$ is added below the base of the water cloud. In this region,

(1.4) has (1.24) as an analytic solution. Since L_D is continuous, the boundary of this region with the water cloud is non-reflecting, so that \mathcal{R} is independent of the details of the added lower region. Applying (1.24) and its first derivative in the added region provides a set of two equations in the two unknowns A and B , which can be solved for $\mathcal{R} = |B/A|$. A similar calculation was done assuming $L_D = L_D(z_1) \exp(z_1 - z)$ in the added region. This functional form also has an analytic solution that allows the upward and downward propagating waves to be identified. As expected, the assumed form for L_D did not affect the results.

We use a similar method to determine the presence of almost-resonant modes. Equation (1.4) is integrated from the top of the model using boundary condition (1.25), to the bottom of the weather layer, where we evaluate a response function

$$r(\lambda) = \left(\frac{1}{L_D^2} \left| \frac{\partial \Phi}{\partial z} \right|_{z=z_1}^2 + \lambda^2 |\Phi|_{z=z_1}^2 \right) / \lambda^2 |\Phi|_{z=z_1}^2. \quad (1.26)$$

The numerator is related to the energy density evaluated at the lower boundary. The denominator is the square of the forcing amplitude, chosen to make $r(\lambda) \geq 1$. Without forcing the denominator would be zero, since $\Phi(z_1) = 0$ when the conditions of the preceding section are satisfied. We define an almost resonant mode as a local maxima of $r(\lambda)$ with $r \gg 1$. Although the choice of response function is somewhat arbitrary (Lindzen and Tung 1976), we tried several response functions, all of which gave similar results.

The results of these calculations are shown in Fig. 1.3 for the standard model at 30° latitude (note that $\lambda_i \propto f_0 \propto \sin(\text{latitude})$) for a water mixing ratio of 10^{-3} by volume. The reflection coefficient \mathcal{R} varies from .90 to .95, with small scale variations due to details of the static stability in the stratosphere, and the response function shows strong peaks at discrete λ_n corresponding to deformation radii λ_n^{-1} of 735, 155, and 88 km. A look at the Φ_n corresponding to the response peaks, as seen in Fig. 1.4, shows that each one has $n - 1$ zeroes in the pressure range between 700 mbar and

Figure 1.3. Reflection coefficients and response function for the standard model.

The solid line is the response function. The dashed line is the reflection coefficient with $L_D(z < z_1) = L_D(z_1)$. The dotted line is the reflection coefficient with $L_D(z < z_1) = L_D(z_1) \exp(z_1 - z)$. Numeric labels are the deformation radii (λ^{-1}) corresponding to peaks in the response function.

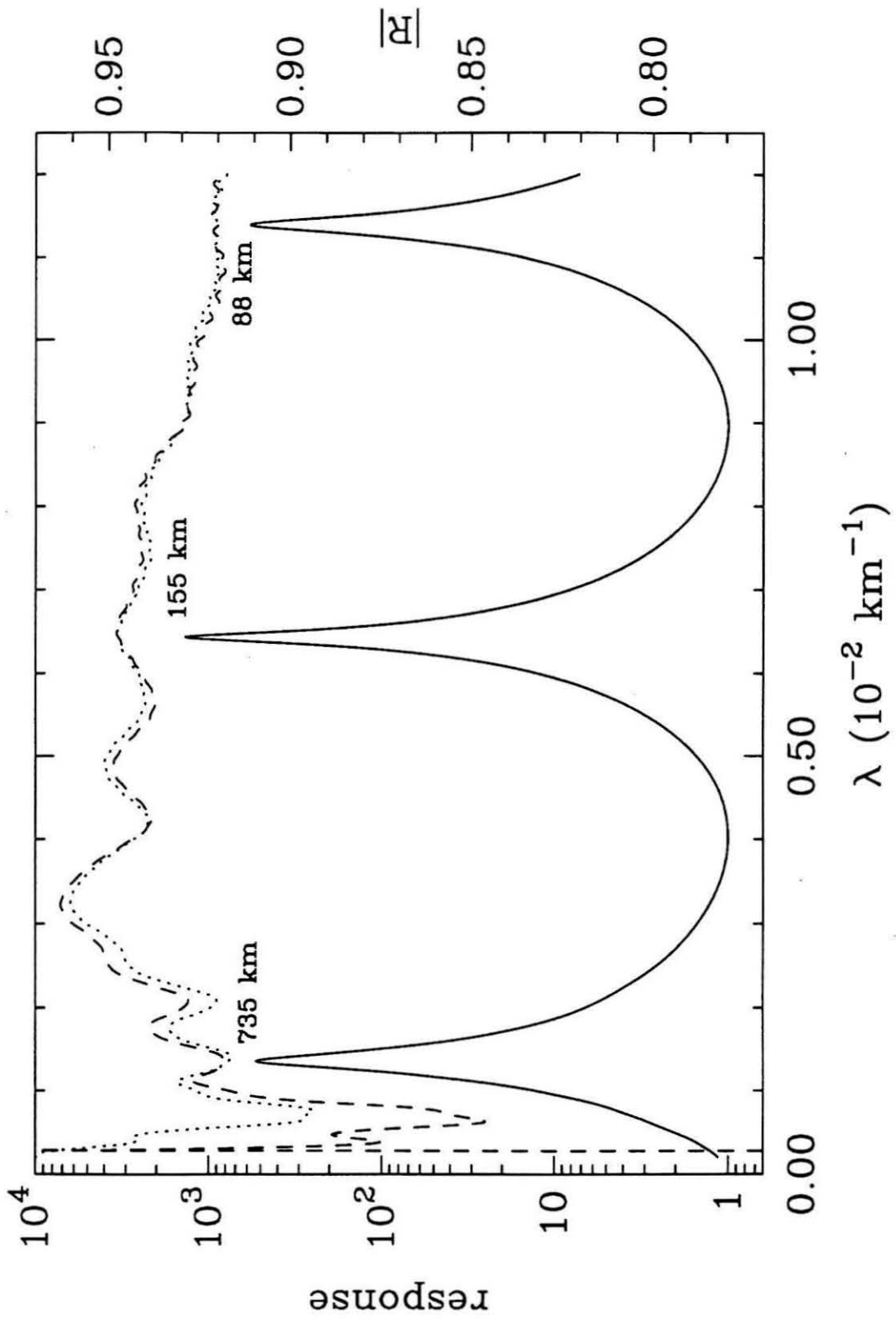
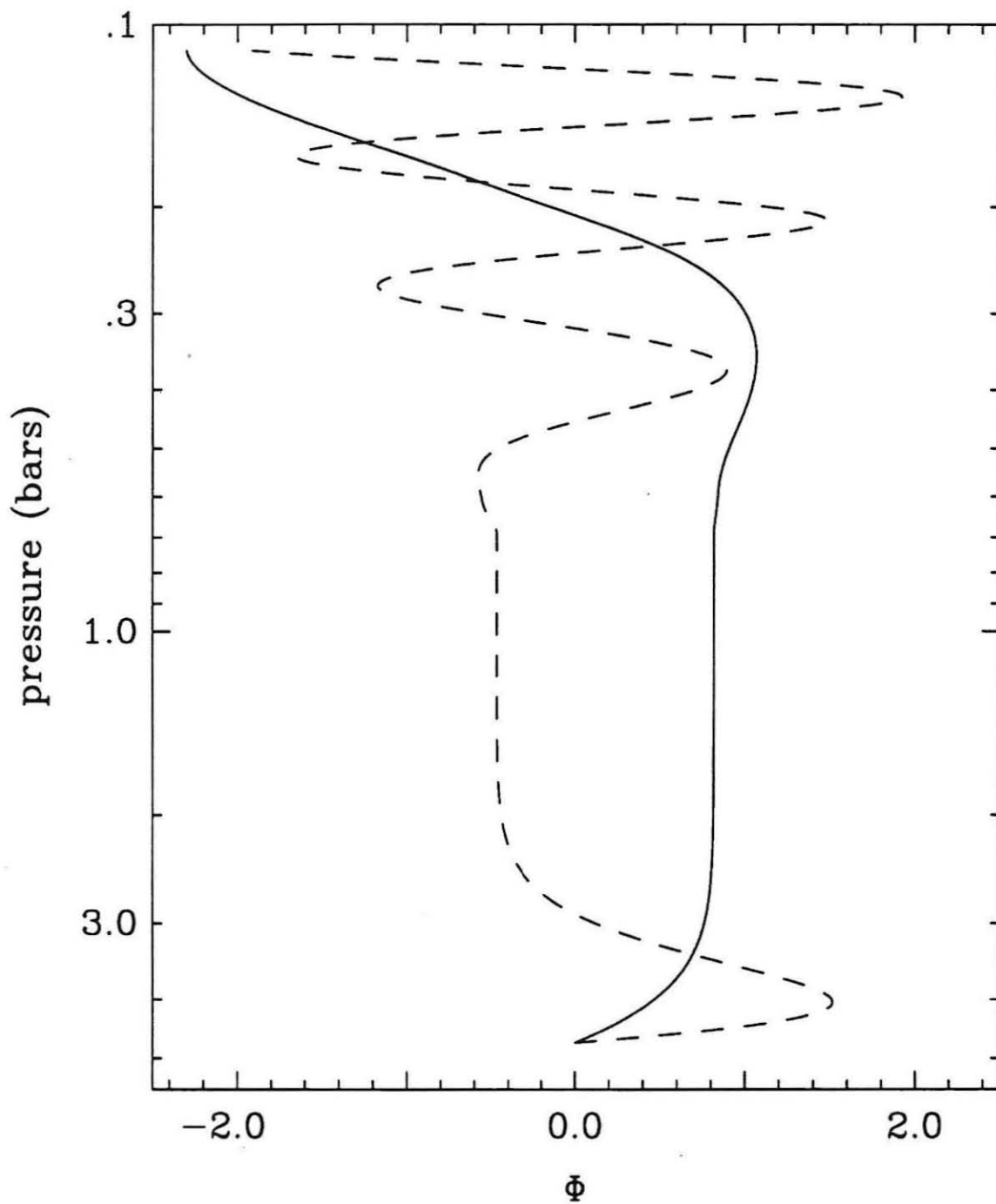


Figure 1.4. Vertical structure Φ_i for the first two peaks in the response function in the standard model, shown at the phase when $\frac{\partial \Phi_i}{\partial z}|_{z=z_1}$ is a maximum. The solid line is for $\lambda^{-1} = 735$ km. The dashed line is for $\lambda^{-1} = 155$ km.



the cloud base — a property of eigenfunctions with a rigid lid. The large reflection coefficients and sharp response peaks are due entirely to vertical variations of the static stability, in contrast to the Earth's atmosphere where variations of the vertical wind shear are necessary to achieve large reflection coefficients (Holton 1979).

Figure 1.5 shows the reflection coefficient and response function with the NH_4SH cloud added. The reflection coefficient is reduced somewhat for values of λ^{-1} between approximately 100 and 500 km. The amplitude of the response peaks are reduced over the standard model, but are still relatively large. Figure 1.6 shows the same calculations repeated using equilibrium hydrogen and no NH_4SH : the reflection coefficient decreases strongly for $\lambda > 3 \times 10^{-3} \text{km}^{-1}$. While the response peaks occur at similar λ as the standard model, only the first peak is strong and sharp. The other peaks are low and broad, as would be expected with a low reflection coefficient. As discussed earlier, the equilibrium hydrogen model does not appear to work for Uranus, and we do not expect it to apply to Jupiter. We also did these calculations for a value of N^2 equal to one-half the wet adiabatic value. This reduction of N^2 has very little effect on either the reflection coefficient or the amplitude of the response peaks, although the values of λ at the peaks are larger by a factor of approximately $\sqrt{2}$. The variation in results for the different assumptions indicates that the response function provides a sensitive test for determining the applicability of the rigid lid and normal-mode approximations.

Since our standard model has a high reflection coefficient and sharp resonances, we are allowed to use a rigid lid. We put this lid at 690 mbar. This choice makes the n^{th} mode of the model with a lid correspond roughly to the n^{th} response peak of the model without a lid for $n = 1, 2$, and 3. With the lid in place, we can calculate the eigenvalues and eigenfunctions of (1.4), and the interaction coefficients γ_{lmn} . The eigenfunctions are normalized so that $\delta_{nn} = 1$. The structure of the modes is nearly

Table 1.1. Parameters of Jupiter Normal-Mode Models.

$f_{\text{H}_2\text{O}}$	λ_1^{-1}	λ_2^{-1}	γ_{111}	γ_{112}	γ_{122}	γ_{222}
5×10^{-3}	1550	389	1.184	-0.1757	0.7936	1.182
2×10^{-3}	985	228	1.174	-0.1574	0.8029	1.304
1×10^{-3}	693	154	1.176	-0.1506	0.8125	1.368
5×10^{-4}	486	106	1.184	-0.1470	0.8228	1.418
2×10^{-4}	300	64	1.200	-0.1453	0.8375	1.470
1×10^{-4}	208	44	1.214	-0.1454	0.8497	1.503

Note: the units of λ_n^{-1} are kilometers and are for $\pm 30^\circ$ latitude; γ_{lmn} are dimensionless; $f_{\text{H}_2\text{O}}$ is the water mole fraction.

identical to the functions shown in Fig. 1.4 for $p > 690$ mbar except for the normalization: the normalized modes have $\Phi_1(690 \text{ mbar}) = 1.26$, and $\Phi_2(690 \text{ mbar}) = -0.708$. The values of λ_n^{-1} and γ_{lmn} are summarized in Table 1.1 for various values of the water abundance (note that $f_{\text{H}_2\text{O}}$ in Table 1.1 is the mole fraction). The deformation radii λ_n^{-1} vary approximately as the square root of the water abundance. Such variation is expected from (1.21) and (1.23), which indicate that N is proportional to $f_{\text{H}_2\text{O}}^{1/2}$, whence L_D and λ_n^{-1} should also vary as $f_{\text{H}_2\text{O}}^{1/2}$ according to (1.2) and (1.4). Although we do not show figures, the reflection coefficients remain high and the response functions remain peaked in the range examined ($10^{-4} \leq f_{\text{H}_2\text{O}} \leq 5 \times 10^{-3}$). The values for $f_{\text{H}_2\text{O}} = 10^{-3}$ are used for all subsequent calculations involving the normal-mode model with a lid.

1.4. Test of Normal-Mode Model: Forced Rossby Waves

A further test of the normal-mode approach is to apply broad-band forcing at the base of the water cloud ($z = z_1$) using the radiation condition (1.25) at 1 mbar. We then determine how well that solution is approximated in $z_1 < z < z_2$ by an expansion in the eigenfunctions obtained with a lid. By “broad-band” we mean that the amplitude imposed at $z = z_1$ is independent of λ , which is related to the frequency and horizontal wavenumber by (1.10). We expect the spectral density $d(\text{energy})/d\lambda$

Figure 1.5. Reflection coefficients and response function for the standard model with an added NH_4SH cloud. The solid line is the response function. The dashed line is the reflection coefficient with $L_D(z < z_1) = L_D(z_1)$. The dotted line is the reflection coefficient with $L_D(z < z_1) = L_D(z_1) \exp(z_1 - z)$. Numeric labels are the deformation radii (λ^{-1}) corresponding to peaks in the response function.

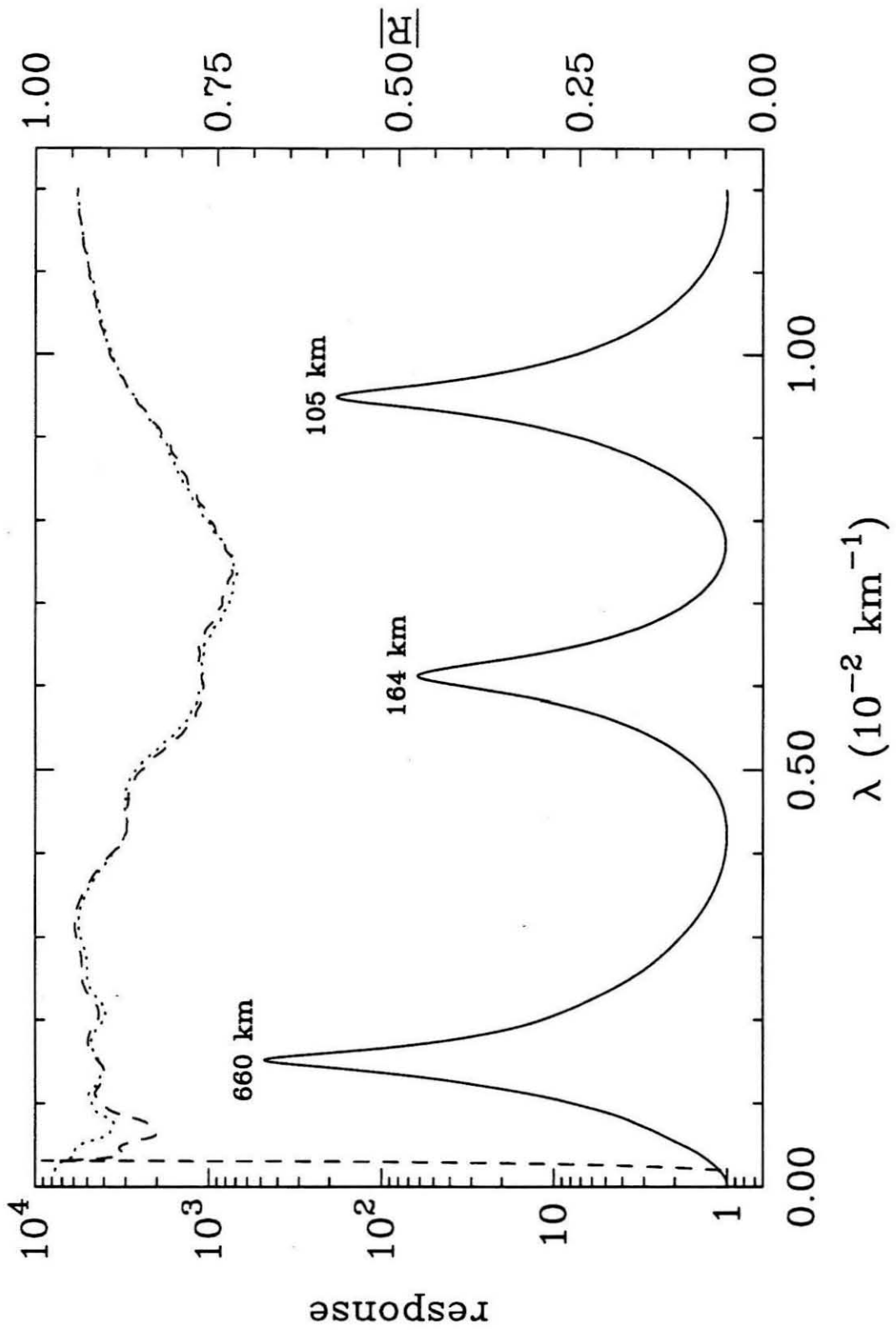
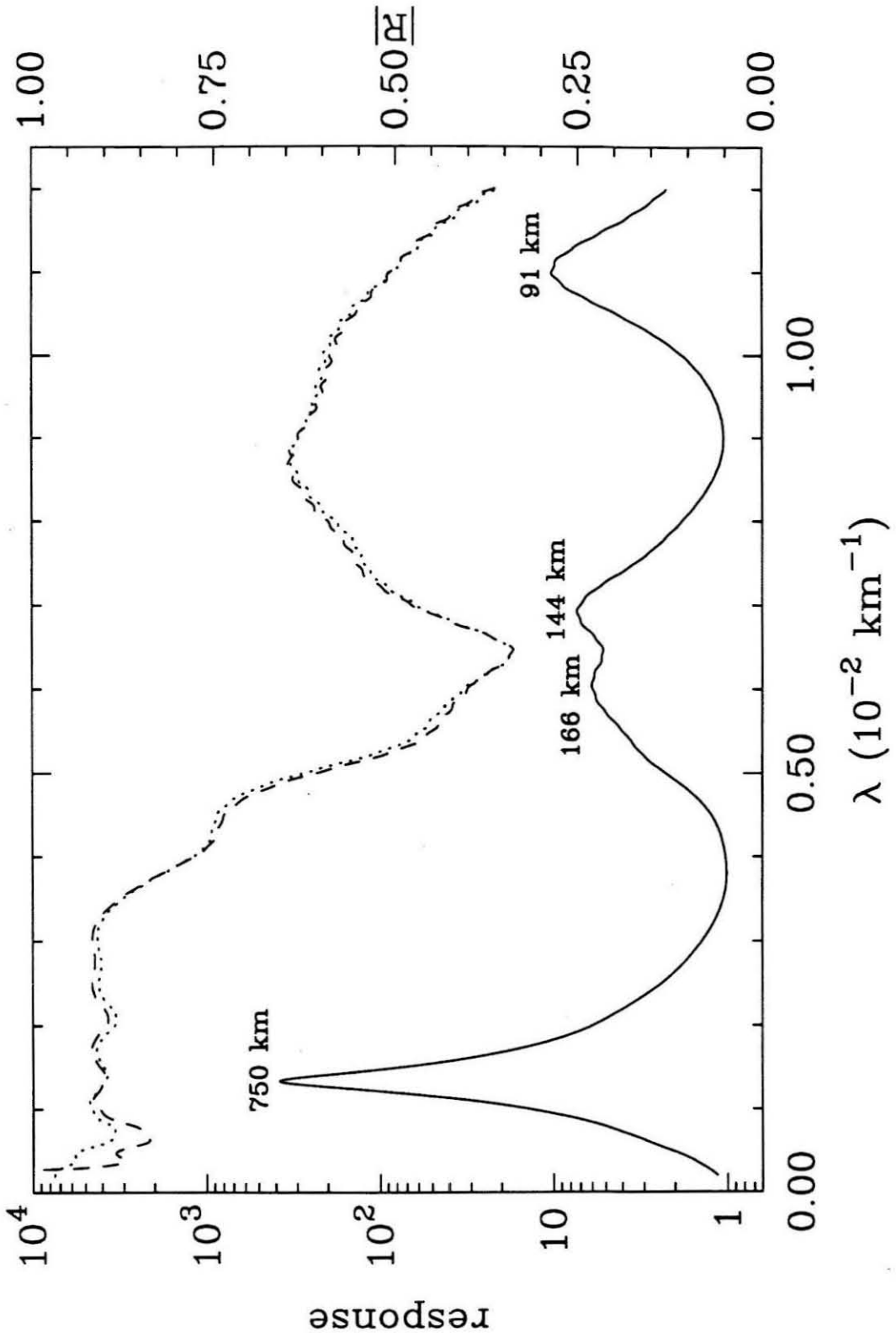


Figure 1.6. Reflection coefficients and response function for equilibrium hydrogen.

The solid line is the response function. The dashed line is the reflection coefficient with $L_D(z < z_1) = L_D(z_1)$. The dotted line is the reflection coefficient with $L_D(z < z_1) = L_D(z_1) \exp(z_1 - z)$. Numeric labels are the deformation radii (λ^{-1}) corresponding to peaks in the response function.



to look something like the response curve in Fig. 1.3, with most of the energy near discrete values of λ . To the extent that the vertical structure of the forced solutions at these frequencies resembles the eigenfunctions obtained with a lid at 690 mbar, the normal mode approximation is good.

We represent the forced wave as a sum over λ :

$$\psi(x, y, z, t) = \sum_{\lambda} (\hat{\phi}_r \cos \alpha + \hat{\phi}_i \sin \alpha), \quad (1.27)$$

where $\hat{\phi}(\lambda; z)$ are complex solutions of (1.4) subject to the radiation condition (1.25), and $\hat{\phi}_r$ and $\hat{\phi}_i$ are the real and imaginary parts of $\hat{\phi}$ respectively. The $\hat{\phi}$ are normalized so that $|\hat{\phi}| = 1$ at $z = z_1$, corresponding to a forcing amplitude independent of λ . The sum in (1.27) includes numerous values of λ on and off the peaks in the response curve. At each λ the phase α of the forcing is arbitrary; we have

$$\alpha(\lambda; x, y, t) = kx + ly + \omega t + \alpha'(\lambda), \quad (1.28)$$

where $\alpha'(\lambda)$ is a random number between 0 and 2π , independent of the α' at all other values of λ .

Specifying all the α 's constitutes a single realization of the possible vertical profiles of ψ . Within $z_1 < z < z_2$, this vertical profile can be represented as an expansion in the real eigenfunctions $\Phi_n(z)$ obtained with the rigid lid at z_2 . The coefficients b_n of this expansion are obtained by minimizing the integrated variance, defined as

$$\sigma_N^2 = \left\langle \left[\sum_{\lambda} (\hat{\phi}_r \cos \alpha + \hat{\phi}_i \sin \alpha) - \sum_{n=1}^N b_n \Phi_n \right]^2 \right\rangle, \quad (1.29)$$

where

$$\langle X \rangle = \int_{z_1}^{z_2} X e^{-z} dz. \quad (1.30)$$

Differentiating with respect to b_n and using the orthonormal property of the Φ_n , namely $\langle \Phi_m \Phi_n \rangle = \delta_{mn}$, we obtain

$$b_n = \sum_{\lambda} \left(\langle \hat{\phi}_r \Phi_n \rangle \cos \alpha + \langle \hat{\phi}_i \Phi_n \rangle \sin \alpha \right). \quad (1.31)$$

Substituting (1.31) into (1.29) gives

$$\sigma_N^2 = \left\langle \left\{ \sum_{\lambda} \left[\left(\hat{\phi}_r - \sum_{n=1}^N \langle \hat{\phi}_r \Phi_n \rangle \Phi_n \right) \cos \alpha + \left(\hat{\phi}_i - \sum_{n=1}^N \langle \hat{\phi}_i \Phi_n \rangle \Phi_n \right) \sin \alpha \right] \right\}^2 \right\rangle \quad (1.32)$$

We average over all possible phases $\alpha(\lambda)$ of the continuous solution to obtain an average measure of the error $\bar{\sigma}_N^2$ in using the normal-mode solution. Using the fact that the α 's are independent and the Φ_n are orthonormal, we find

$$\bar{\sigma}_N^2 = \frac{1}{2} \sum_{\lambda} \left[\langle \hat{\phi}_r^2 \rangle + \langle \hat{\phi}_i^2 \rangle - \sum_{n=1}^N \left(\langle \hat{\phi}_r \Phi_n \rangle^2 + \langle \hat{\phi}_i \Phi_n \rangle^2 \right) \right]. \quad (1.33)$$

A dimensionless measure of error is obtained by comparing this best fit variance $\bar{\sigma}_N^2$ to the variance $\bar{\sigma}_0^2$ with no fit at all. Calling the ratio of these χ^2 , we define

$$\chi_N^2 = \frac{\bar{\sigma}_N^2}{\bar{\sigma}_0^2}, \quad (1.34)$$

where

$$\bar{\sigma}_0^2 = \frac{1}{2} \sum_{\lambda} \left[\langle \hat{\phi}_r^2 \rangle + \langle \hat{\phi}_i^2 \rangle \right]. \quad (1.35)$$

Calculations were performed using the standard model, with $N = 2$ and $N = 3$, corresponding to 2-mode and 3-mode expansions respectively. Since λ^2 can be either positive or negative according to (1.10), summations over λ were done using both real and imaginary λ . When λ is imaginary, the outgoing wave condition (1.25) is replaced by the requirement that Φ decays exponentially with altitude. The negative- λ^2 solutions are non-resonant (response functions are of order unity), and therefore these solutions do not contribute appreciably to the magnitudes of ψ or χ_N^2 . We summed over $|\lambda| \leq \lambda_{\max}$, using two values of λ_{\max} , namely $9.0 \times 10^{-3} \text{ km}^{-1}$ and $1.4 \times 10^{-2} \text{ km}^{-1}$, with equally spaced intervals in λ of 10^{-5} km^{-1} . The values of λ_{\max} were chosen near the minimum of the response function following the $N = 2$ and $N = 3$ response peaks of the standard case. The resulting normalized errors are $\chi_2^2 = 0.0152$ for $\lambda_{\max} = 9 \times 10^{-3} \text{ km}^{-1}$, and $\chi_2^2 = 0.296$ and $\chi_3^2 = 0.0116$ for

$\lambda_{\max} = 1.4 \times 10^{-2}$ km. These numbers indicate that the normal-mode expansion provides a good approximation to the actual structure of uniformly forced waves, provided all of the modes with $\lambda_n < \lambda_{\max}$ are included. For the equilibrium hydrogen case, for which the reflection coefficients are not close to one (see Fig. 1.6), the values of χ_2^2 , χ_3^2 , and χ_4^2 are 0.211, 0.144, and 0.0472, respectively, when $\lambda_{\max} = 1.4 \times 10^{-2}$.

1.5. Test of Normal Mode Model: Baroclinic Instability

As a final test of the normal-mode model, we consider the problem of pure baroclinic instability. Solutions to this problem for three different models are compared: a continuous model with a radiation condition at 1 mbar, a continuous model with a rigid lid at 690 mbar, and our standard normal-mode model with $N = 2$. This allows us to determine the effects both of a rigid lid and of the normal-mode approximation separately. In all cases, we use the standard model of the thermal structure, with solid body rotation in the interior (i.e., $\psi_0 = 0$). We assume a basic state velocity given by

$$\bar{u}(z) = U_1\Phi_1(z) + U_2\Phi_2(z), \quad (1.36)$$

where Φ_1 and Φ_2 are the first two baroclinic eigenfunctions of the normal-mode expansion and the U_n are given constants. The basic state streamfunction is then

$$\bar{\psi}(y, z) = -U_1y\Phi_1(z) - U_2y\Phi_2(z). \quad (1.37)$$

To determine the baroclinic stability of the basic state, we add an infinitesimal perturbation of the form $\psi'(z)\exp(ikx - ikct)$ to the basic flow and solve for the phase speed c as a function of U_1 , U_2 and k . If c has an imaginary component, the perturbation will grow exponentially with growth rate kc_i ; until non-linear effects become important, and the basic flow is linearly unstable.

To solve this problem using the $N = 2$ normal-mode model, we expand ψ' in

our orthonormal eigenfunctions Φ_n :

$$\psi'(z) = \psi'_1 \Phi_1(z) + \psi'_2 \Phi_2(z). \quad (1.38)$$

Substituting (1.37) and (1.38) into (1.15), we obtain a set of equations for ψ'_n :

$$\begin{aligned} (A_{11} + c)\psi'_1 + A_{12}\psi'_2 &= 0, \\ A_{21}\psi'_1 + (A_{22} + c)\psi'_2 &= 0, \end{aligned} \quad (1.39)$$

where

$$\begin{aligned} A_{11} &= (\beta - k^2(\gamma_{111}U_1 + \gamma_{112}U_2) - \gamma_{112}(\lambda_1^2 - \lambda_2^2)U_2) / (k^2 + \lambda_1^2), \\ A_{12} &= (-k^2(\gamma_{112}U_1 + \gamma_{122}U_2) + \gamma_{112}(\lambda_1^2 - \lambda_2^2)U_1) / (k^2 + \lambda_1^2), \\ A_{21} &= (-k^2(\gamma_{112}U_1 + \gamma_{122}U_2) - \gamma_{122}(\lambda_1^2 - \lambda_2^2)U_2) / (k^2 + \lambda_2^2), \\ A_{22} &= (\beta - k^2(\gamma_{122}U_1 + \gamma_{222}U_2) + \gamma_{122}(\lambda_1^2 - \lambda_2^2)U_1) / (k^2 + \lambda_2^2). \end{aligned} \quad (1.40)$$

This can be treated as a matrix eigenvalue problem, and will have non-trivial solutions only when $\det |\mathbf{A} + c\mathbf{I}| = 0$, which can be solved for the phase speed c to obtain

$$c = -\frac{1}{2}(A_{11} + A_{22}) \pm \left[\frac{1}{4}(A_{11} - A_{22})^2 + A_{12}A_{21} \right]^{1/2}. \quad (1.41)$$

If the quantity in square brackets is negative, the phase speed of the perturbation is complex and the flow is linearly unstable. For known values of β , γ_{lmn} and λ_n^2 , the 2-mode instability problem has three independent parameters: k^2 , which determines the length scale of the perturbation, $s = U_2/U_1$, which determines the shape of the unperturbed basic state velocity profile, and $U = \text{sgn}(U_1)(U_1^2 + U_2^2)^{1/2} = U_1(1 + s^2)^{1/2}$, which determines the amplitude of the basic state. It is then straightforward to calculate $c(s, U, k^2)$ from (1.41) and map out the regions of stable and unstable flow.

Calculations were performed with the standard model with $f_{\text{H}_2\text{O}} = 10^{-3}$. Calculations were done first with $s = 1.769$, which is a jet with $\bar{u} = 0$ at $z = z_1$ and $z = z_2$, and second with $s = -0.214$, which is a shear profile with $d\bar{u}/dz = 0$ at $z = z_1$ and $z = z_2$. These velocity profiles are shown in Fig. 1.7. Contour plots of the growth

Figure 1.7. Velocity profiles used in baroclinic instability calculations for $s = 1.769$ (solid line) and $s = -0.214$ (dashed line) with $U = 1 \text{ m s}^{-1}$. At pressures greater than 690 mbar, these profiles are essentially linear combinations of the curves shown in Fig. 1.4.

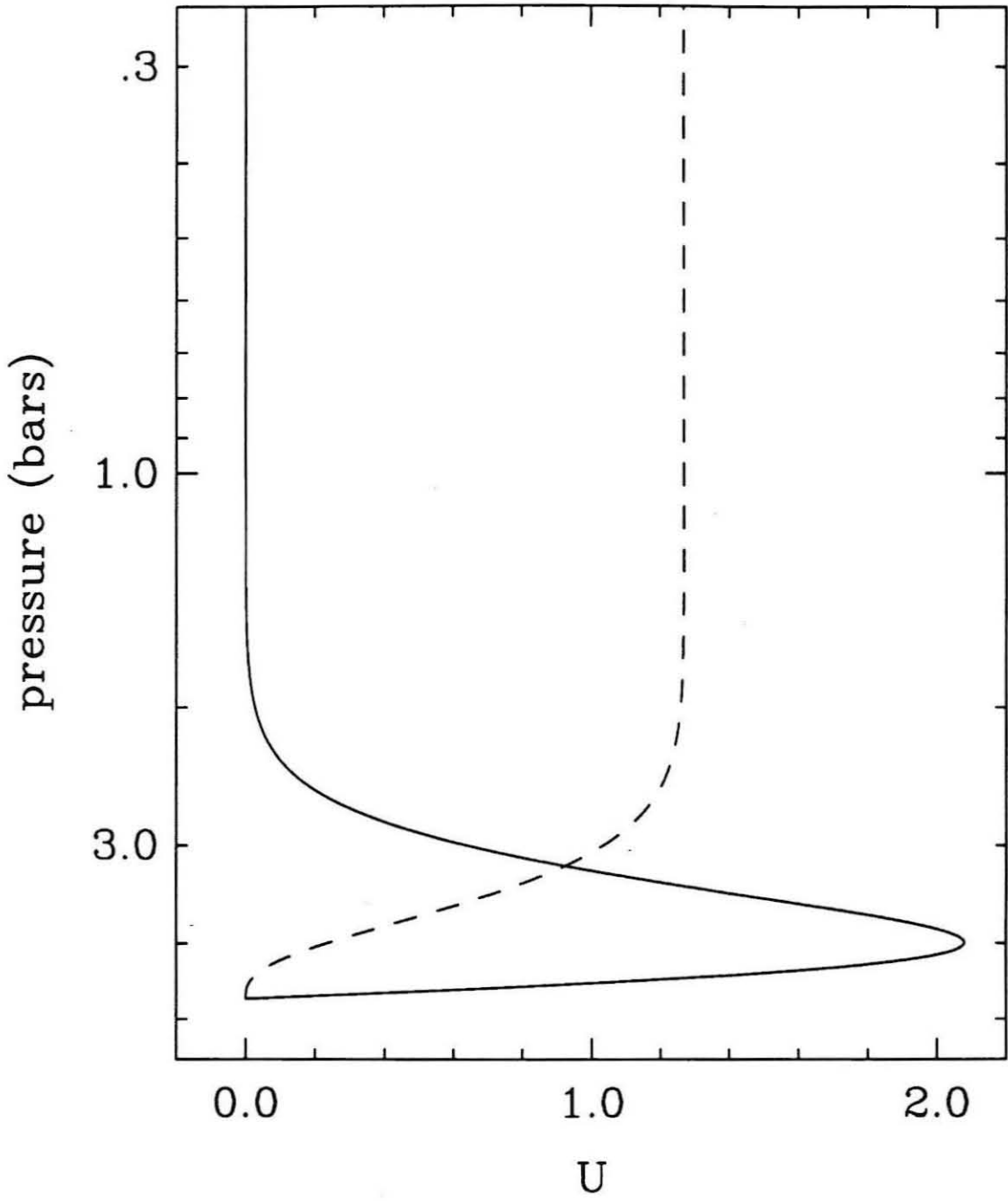


Figure 1.8. Contour plot of growth rates for $s = 1.769$. The contour interval is $2 \times 10^{-7} \text{ s}^{-1}$ and the outer contour is the zero contour.

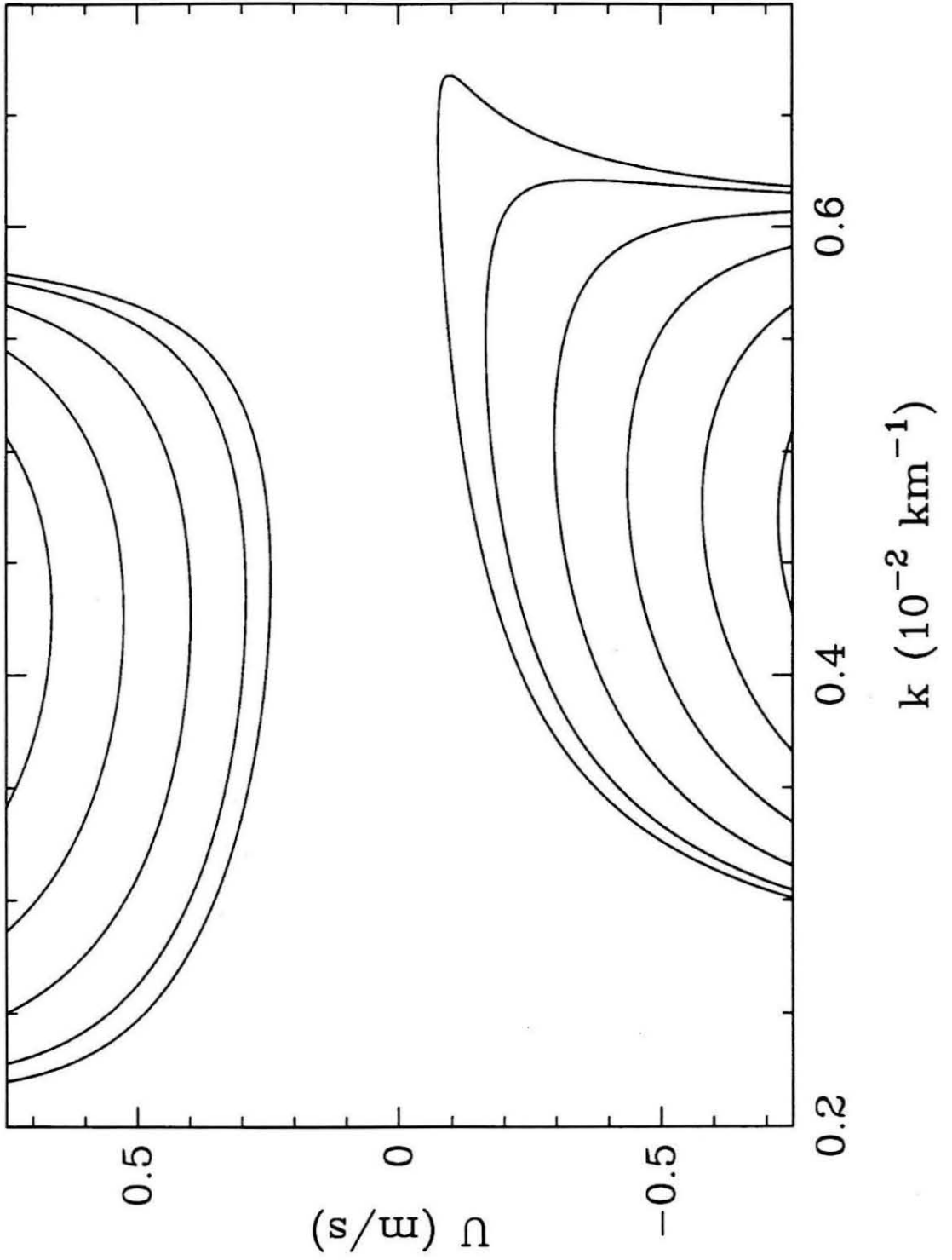


Figure 1.9. Contour plot of growth rates for $s = -0.214$. The contour interval is $2 \times 10^{-7} \text{ s}^{-1}$ and the outer contour is the zero contour.

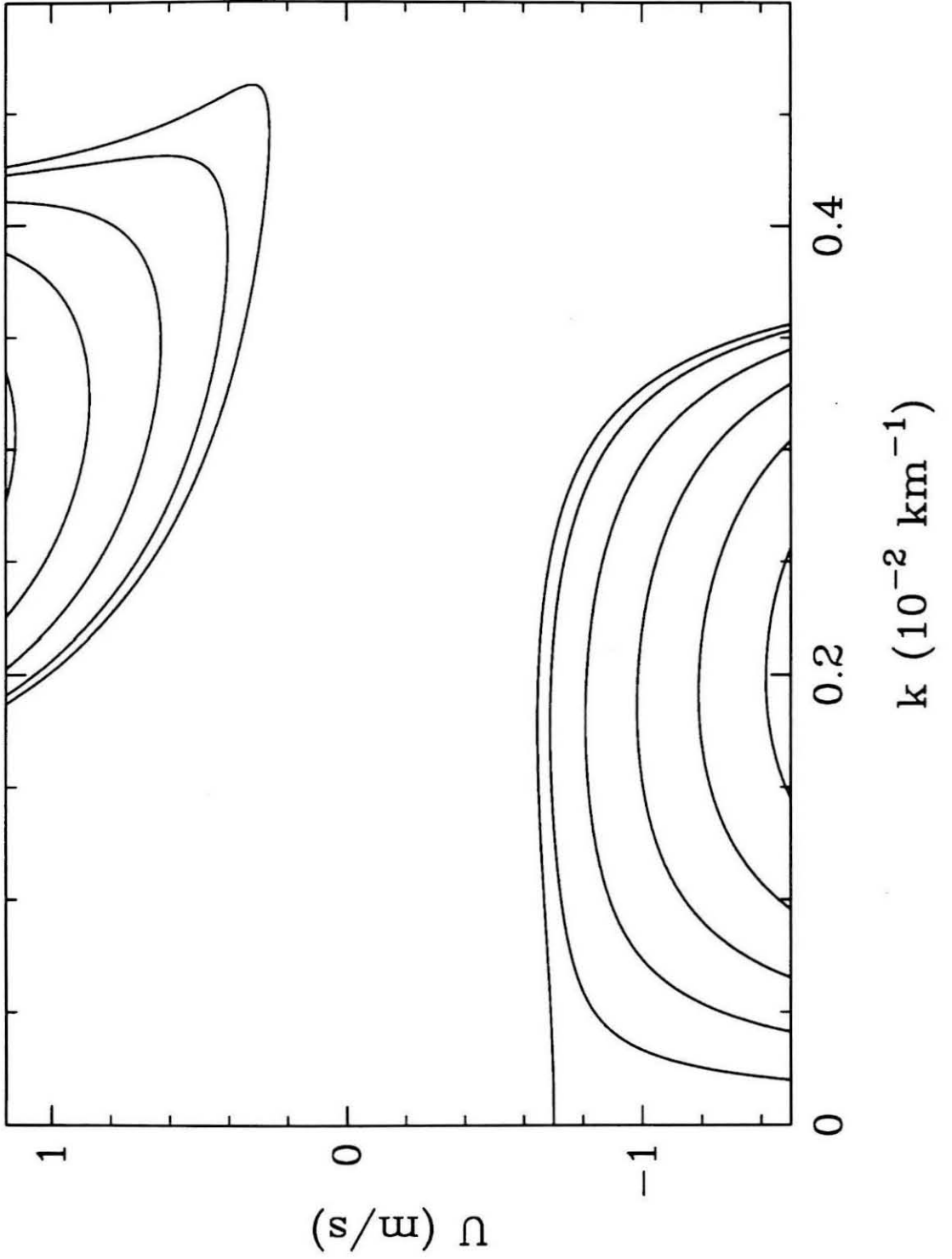


Figure 1.10. Contour plot of growth rates for $U = 79.5 \text{ m s}^{-1}$. The contour interval is $5 \times 10^{-6} \text{ s}^{-1}$ and the outer contour is the zero contour.

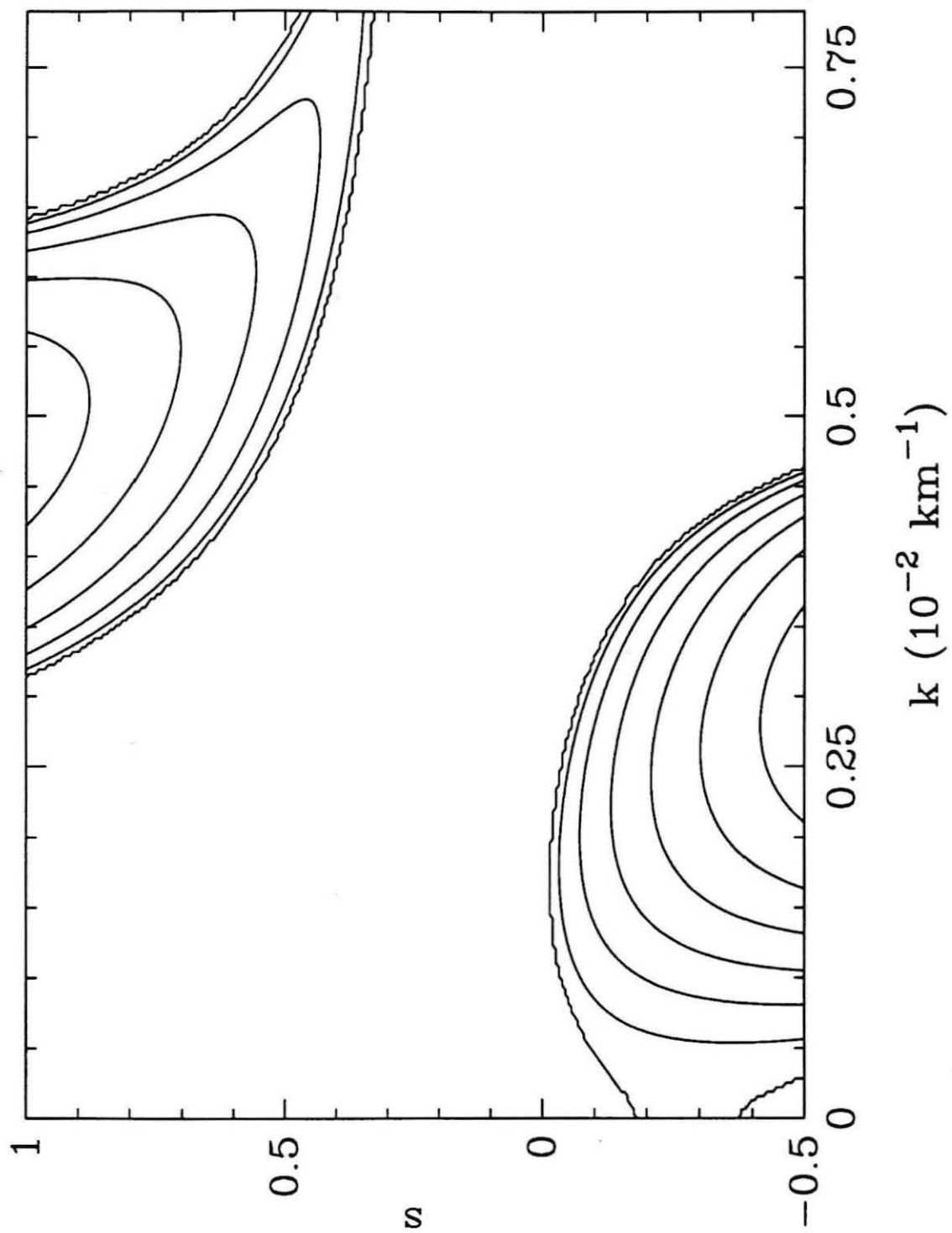
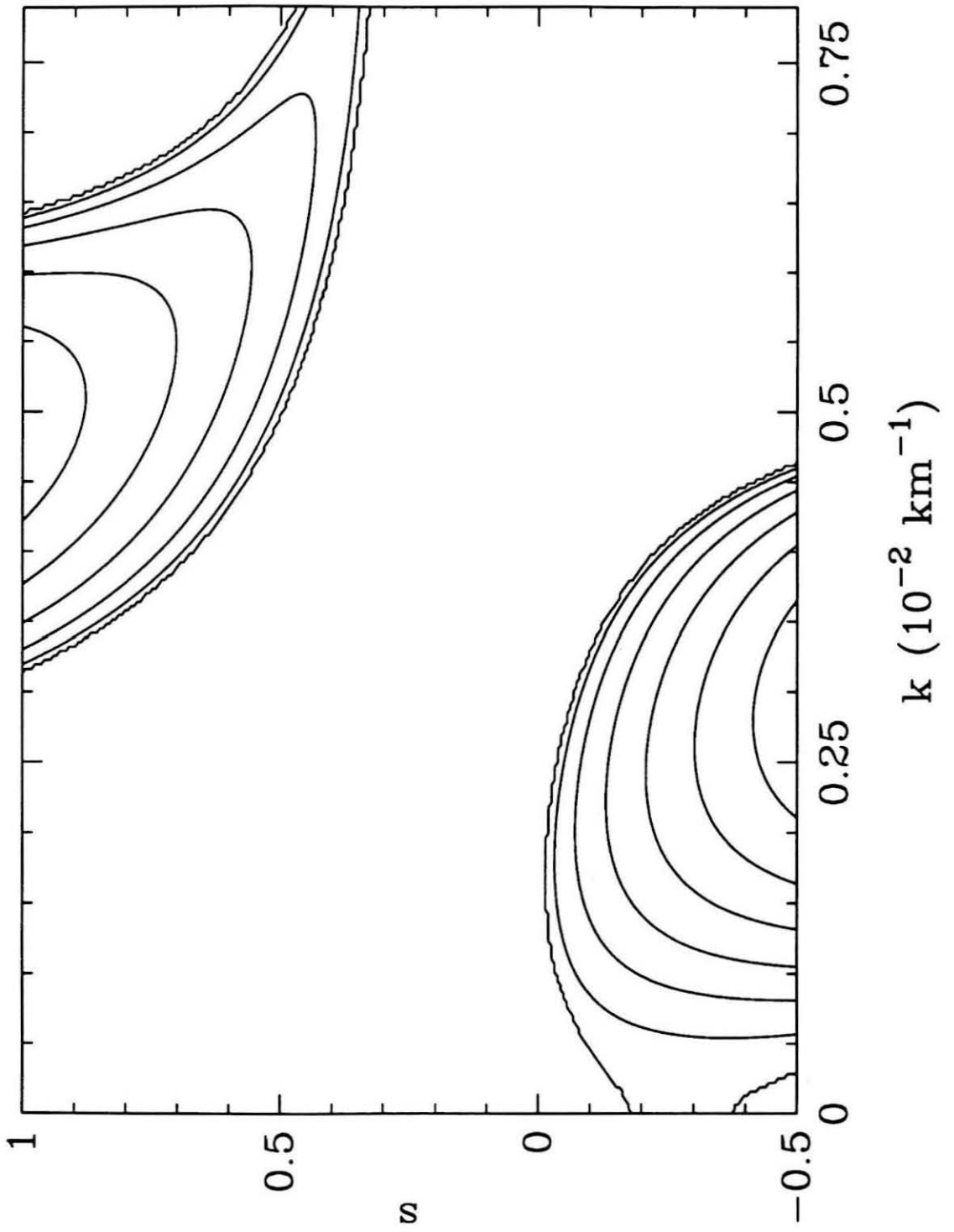


Figure 1.11. Contour plot of growth rates for $U = -79.5 \text{ m s}^{-1}$. The contour interval is $5 \times 10^{-6} \text{ s}^{-1}$ and the outer contour is the zero contour.



rates are shown in Fig. 1.8 for $s = 1.769$ and in Fig. 1.9 for $s = -0.214$. Velocities of order 1 m/s are required for the flow to become unstable. Figures 1.10 and 1.11 show growth rate contours in the k^2 - s plane for velocities more typical for Jupiter ($U = 79.5 \text{ m s}^{-1}$). At these large U , $s < 0$ is more unstable than $s > 0$, and for $s < 0$ only a small amount of the second mode is needed for instability, although $s = 0$ is stable. For large values of U , the β terms in (1.40) are negligible for all growing disturbances. The remaining terms are proportional to U , so the phase speed and growth rate become proportional to U for large U . It can be shown that $s = 0$ (a pure first mode) is always stable in the 2-mode model. This is done by noting that c can have an imaginary part only if $A_{12}A_{21} < 0$. However, with $U_2 = s = 0$, $A_{12}A_{21}$ is proportional to $(k^2 - \lambda_1^2 + \lambda_2^2)$ with a positive constant of proportionality. In this case, $A_{12}A_{21} > 0$, since $\lambda_1^2 < \lambda_2^2$. The shape of the profiles for various positive and negative s have the same general properties as the cases described above.

We now wish to compare these results for the 2-mode model to the models with continuous vertical structure. With a basic state velocity $\bar{u}(z)$ as given in (1.36) and perturbations of the form $\psi'(z) \exp(ikx - ikct)$, the equation for the vertical structure of the disturbance is (Pedlosky 1987)

$$(\bar{u} - c)(\mathcal{L}\psi' - k^2\psi') + (\beta - \mathcal{L}\bar{u})\psi' = 0. \quad (1.42)$$

The lower boundary condition is $\psi'(z_1) = 0$, as derived in Section 1.2. In solving (1.42), we consider two upper boundary conditions: a rigid lid at 690 mbar (the same boundary condition used in the 2-mode model), and a radiation condition imposed at 1 mbar. For the second case, $\bar{u}(z)$ is assumed constant above 690 mbar so that instability will only occur in the region covered by the normal-mode model. More general basic states which do not have $\partial\bar{u}/\partial z = 0$ for $p \leq 690$ mbar are possible, but are not considered in this paper. This problem can again be treated as an eigenvalue problem for the phase speed c .

The problem is solved by integrating (1.42) from the upper to lower boundary by a fourth order Runge-Kutta scheme and defining a complex function $F(c)$ as the value of $\psi'(z_1)$ (i.e., the error in satisfying the lower boundary condition). The eigenvalues then correspond to the zeroes of $F(c)$, which are found by Newton-Raphson iteration, using the results of the 2-mode model as an initial guess. To avoid problems in integrating through critical levels (where $\bar{u} = c$), we only solved the continuous problem in the region of instability, where c has an imaginary component. Also, we used different resolutions to make sure that the step size did not affect the results.

Typical results are presented in Figs. 1.12–1.14, which show vertical and horizontal cuts through the curves of Figs. 1.8 and 1.10. Figure 1.12 shows a comparison of the phase speeds and growth rates for the continuous and 2-mode solutions with $s = 1.769$, $U = 0.531 \text{ m s}^{-1}$ and variable k . This case is somewhat unusual in that the 2-mode model has growth rates slightly lower than both of the continuous models, with and without the lid; the normal-mode model generally tends to overestimate growth rates. The growth rates of the normal-mode model also drop off more sharply at the edge of the unstable region than both continuous models. This effect was observed in all of our calculations. The calculations also show that the effect of the rigid lid approximation decreases with increasing wavenumber. Despite the differences at the edge of the unstable region, the normal-mode solution approximates the continuous solutions fairly well around the most unstable wavelength. Figure 1.13 shows a comparison between the 2-mode and continuous solutions for $s = 1.769$, $k = 4.56 \times 10^{-3} \text{ km}^{-1}$ and U varying. The normal-mode solution approximates the continuous solution quite well, slightly overestimating the growth rates, except at the boundary of the unstable region. Figure 1.14 compares 2-mode and continuous solutions for $k = 1.69 \times 10^{-3} \text{ km}^{-1}$, $U = -79.5 \text{ m s}^{-1}$ and variable s . For this case, the 2-mode model again overestimates the growth rates, and the effect of the upper

Figure 1.12. Phase speed and growth rates for $s = 1.769$, $U = 0.531 \text{ m s}^{-1}$, representing a horizontal cut through the upper lobe of Fig. 1.8. The solid line is the 2-mode solution, the dashed line is the continuous solution with a rigid lid, and the dotted line is the continuous solution with the radiation condition.

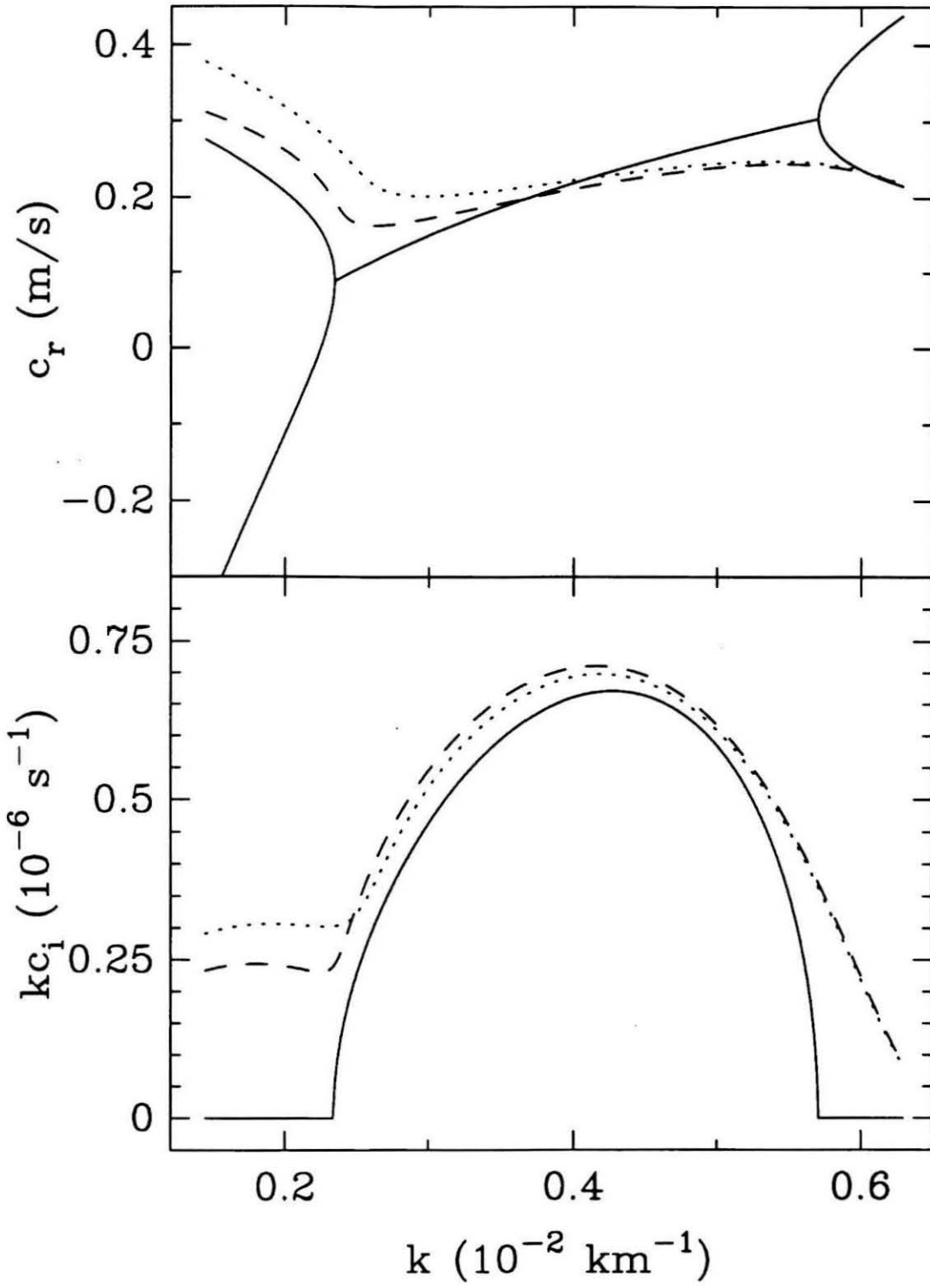


Figure 1.13. Phase speed and growth rates for $s = 1.769$, $k = 4.56 \times 10^{-3} \text{ km}^{-1}$, representing a vertical cut through the lower lobe of Fig. 1.8. The solid line is the 2-mode solution, the dashed line is the continuous solution with a rigid lid, and the dotted line is the continuous solution with the radiation condition.

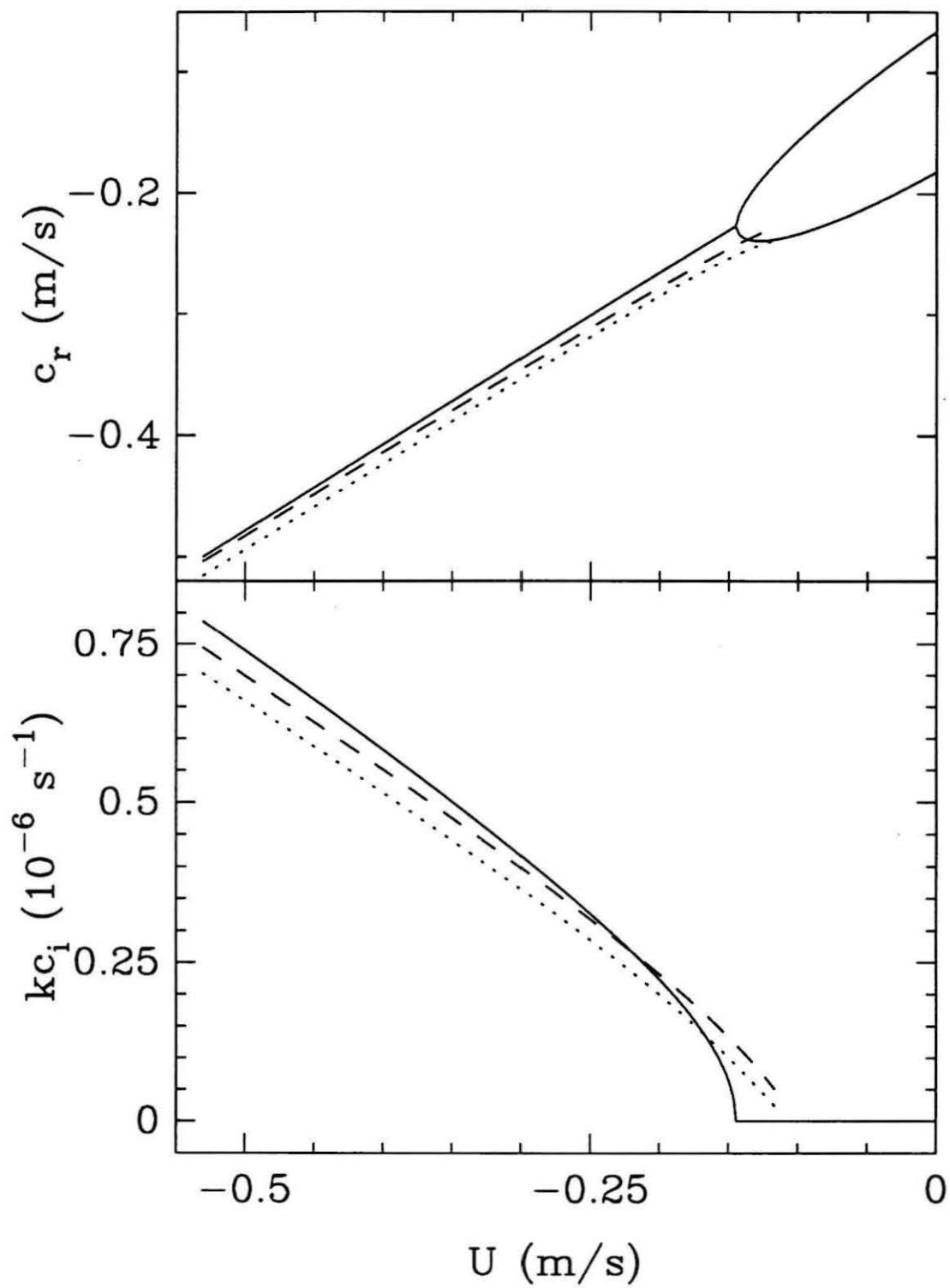
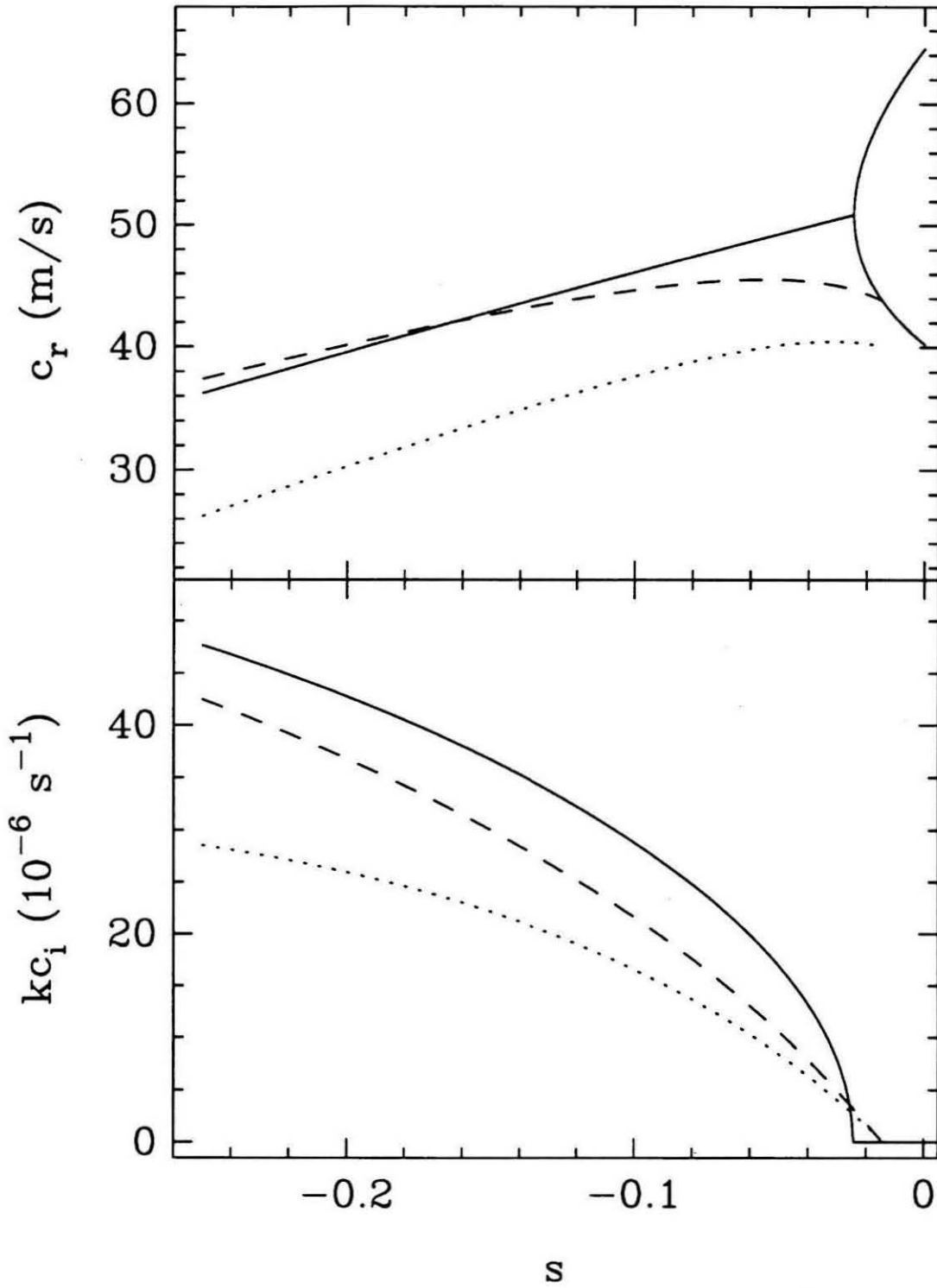


Figure 1.14. Phase speed and growth rates for $k = 1.69 \times 10^{-3} \text{ km}^{-1}$, $U = -79.5 \text{ m s}^{-1}$, representing a vertical cut through the lower lobe of Fig. 1.10. The solid line is the 2-mode solution, the dashed line is the continuous solution with a rigid lid, and the dotted line is the continuous solution with the radiation condition.



boundary condition on the solution is fairly large due to the small wavenumber. In general, although the normal-mode model usually overestimates growth rates and underestimates the size of the unstable regions, it provides a good enough approximation around the most unstable wavelengths to be usable in calculations where a larger number of vertical degrees of freedom is impractical.

1.6. Conclusions

In this paper, we have proposed a normal-mode model for the dynamics of Jupiter's atmosphere, in which the vertical structure is represented by a summation over orthogonal functions which are solutions to the equation for the vertical structure of Rossby waves. In Section 1.2 we developed the relevant equations for a Jovian planet with a deep, adiabatic, fluid interior. One consequence of the adiabatic interior is that the model with one baroclinic mode is dynamically equivalent to the one-layer model commonly used to study Jovian atmospheric dynamics. Thus, calculations like those in Section 1.3 can also be used to calibrate one layer models. For example, using our standard case (frozen equilibrium hydrogen with a volume mixing ratio of water of 10^{-3}), we find that the proper deformation radius is ≈ 735 km for a latitude of ± 30 degrees, and that velocities in the layer model can be approximately compared directly to the observations (see Eq. 1.20).

Calculation of reflection coefficients shows that our standard model has a stratosphere that reflects most (~ 90 percent) of the energy incident upon it. This leads to nearly resonant modes at discrete values of the deformation radius λ^{-1} , making the rigid lid approximation viable and allowing us to calculate a set of orthonormal eigenfunctions for use in the normal-mode expansion. Results in which NH_4SH contributes to N^2 are similar to the standard model, although the reflection coefficients are somewhat lower. Results with equilibrium hydrogen are not as good. The reflection coefficient is only near one when $\lambda \lesssim 3 \times 10^{-3} \text{ km}^{-1}$ so that only one

nearly-resonant mode occurs. In this case the usefulness of the normal-mode model is restricted to a single baroclinic mode. The same calculations can be done for any given model of the thermal structure to determine the applicability of a normal-mode expansion.

We further tested the normal-mode model on the problems of forced Rossby waves and baroclinic instability. In Section 1.4 we demonstrated that the response to broadband forcing is sufficiently concentrated near the resonances for the result to be well approximated by the eigenfunction expansion. We then compared a two-mode model of pure baroclinic instability to the continuous problem. The results show that the two-mode model provides a reasonably good approximation in the wavelengths around the maximum growth rate, so that the normal-mode model provides a simple, qualitatively correct method of including baroclinic effects into models of Jupiter's atmospheric dynamics.

Acknowledgements

This research was supported by the NASA Planetary Atmospheres program under grant NAGW-58.

References

- Allison, M., and P. H. Stone, 1983: Saturn meteorology: A diagnostic assessment of thin-layer configurations for the zonal flow. *Icarus* **54**, 296-308.
- Barcilon, A., and P. Gierasch, 1970: A moist Hadley cell model for Jupiter's cloud bands. *J. Atmos. Sci.* **27**, 550-560.
- Bjoraker, G. L., H. P. Larson and V. G. Kunde, 1986a: The abundance and distribution of water vapor in Jupiter's atmosphere. *Astrophys. J.* **311**, 1058-1072.

- Bjoraker, G. L., H. P. Larson and V. G. Kunde, 1986b: The gas composition of Jupiter derived from 5- μ m airborne spectroscopic observations. *Icarus* **66**, 579-609.
- Busse, F. H., 1976: A simple model of convection in the Jovian atmosphere. *Icarus* **29**, 255-260.
- Conrath, B. J. and P. J. Gierasch, 1984: Global variation of the para hydrogen fraction in Jupiter's atmosphere and implications for dynamics on the outer planets. *Icarus* **57**, 184-204.
- Conrath, B. J. and P. J. Gierasch, 1986: Retrieval of ammonia abundances and cloud opacities on Jupiter from *Voyager* IRIS spectra. *Icarus* **67**, 444-455.
- Conrath, B. J., P. J. Gierasch and N. Nath, 1981: Stability of zonal flows on Jupiter. *Icarus* **48**, 256-282.
- Dowling, T. E. and A. P. Ingersoll, 1988: Potential vorticity and layer thickness variations in the flow around Jupiter's Great Red Spot and White Oval BC. *J. Atmos. Sci.* **45**, 1380-1396.
- Dowling, T. E. and A. P. Ingersoll, 1989: Jupiter's Great Red Spot as a shallow water system. Submitted to *J. Atmos. Sci.*
- Flierl, G. R., 1978: Models of vertical structure and the calibration of two-layer models. *Dyn. Atmos. Oceans* **2**, 341-381.
- Gavrilin, B. L., 1965: On the description of vertical structure of synoptical processes. *Izv. Atmos. Ocean. Phys.* **1**, 8-17.
- Gierasch, P. J. and B. J. Conrath, 1987: Vertical temperature gradients on Uranus: Implications for layered convection. *J. Geophys. Res.* **92**, 15019-15029.
- Gierasch, P. J., B. J. Conrath and J. A. Magalhães, 1986: Zonal mean properties of Jupiter's upper troposphere from *Voyager* infrared observations. *Icarus* **67**, 456-483.

- Gierasch, P. J., A. P. Ingersoll and D. Pollard, 1979: Baroclinic instabilities in Jupiter's zonal flow. *Icarus* **40**, 205–212.
- Gill, A. E., 1982: *Atmosphere–Ocean Dynamics*. Academic Press, New York.
- Halevy, I. and W. R. Peltier, 1985: Barotropic instability and Rossby wave radiation. *J. Atmos. Sci.* **42**, 1825–1837.
- Hatzes, A., D. D. Wenkert, A. P. Ingersoll and G. E. Danielson, 1981: Oscillations and velocity structure of a long-lived cyclonic spot. *J. Geophys. Res.* **86**, 8745–8749.
- Holton, J. R., 1979: *An Introduction to Dynamic Meteorology, second edition*. Academic Press, New York.
- Ingersoll, A. P., R. F. Beebe, B. J. Conrath and G. E. Hunt, 1984: Structure and dynamics of Saturn's atmosphere. In *Saturn* (T. Gehrels and M. S. Matthews, eds.) pp. 195–238. University of Arizona Press, Tucson.
- Ingersoll, A. P., R. F. Beebe, J. L. Mitchell, G. W. Garneau, G. M. Yagi and J.-P. Müller, 1981: Interaction of eddies and mean zonal flow on Jupiter as inferred from *Voyager 1* and *2* images. *J. Geophys. Res.* **86**, 8733–8743.
- Ingersoll, A. P. and P. G. Cuong, 1981: Numerical model of long-lived Jovian vortices. *J. Atmos. Sci.* **38**, 2067–2076.
- Ingersoll, A. P. and R. L. Miller, 1986: Motions in the interiors and atmospheres of Jupiter and Saturn 2. Barotropic instabilities and normal modes of an adiabatic planet. *Icarus* **65**, 370–382.
- Ingersoll, A. P. and D. Pollard, 1982: Motion in the interiors and atmospheres of Jupiter and Saturn: scale analysis, anelastic equations, barotropic stability criterion. *Icarus* **52**, 62–80.
- Lewis, J. S., 1969: The clouds of Jupiter and the $\text{NH}_3\text{-H}_2\text{O}$ and $\text{NH}_3\text{-H}_2\text{S}$ systems. *Icarus* **10**, 365–378.

- Limaye, S. S., 1986: Jupiter: new estimates of the mean zonal flow at the cloud level. *Icarus* **65**, 335–352.
- Limaye, S. S., H. E. Revercomb, L. A. Sromovsky, R. J. Krauss, D. Santek, V. E. Suomi, S. A. Collins and C. C. Avis, 1982: Jovian winds from *Voyager 2*: Part I. Zonal mean circulation. *J. Atmos. Sci.* **39**, 1413–1432.
- Lindal, G. F., G. E. Wood, G. S. Levy, J. D. Anderson, D. N. Sweetnam, H. B. Hotz, B. J. Buckles, D. P. Holmes, P. E. Doms, V. R. Eshleman, G. L. Tyler and T. A. Croft, 1981: The atmosphere of Jupiter: An analysis of the *Voyager* radio occultation measurements. *J. Geophys. Res.* **86**, 8721–8727.
- Lindzen, R. S., E. S. Batten and J. W. Kim, 1967: Oscillations in atmospheres with tops. *Mon. Wea. Rev.* **95**, 441–451.
- Lindzen, R. S. and K.-K. Tung, 1976: Banded convective activity and ducted gravity waves. *Mon. Wea. Rev.* **104**, 1602–1617.
- Lunine, J. I. and D. M. Hunten, 1987: Moist convection and the abundance of water in the troposphere of Jupiter. *Icarus* **69**, 566–570.
- Mac Low, M.-M. and A. P. Ingersoll, 1986: Merging of vortices in the atmosphere of Jupiter: an analysis of *Voyager* images. *Icarus* **65**, 353–369.
- Marcus, P. S., 1988: A numerical simulation of the Great Red Spot of Jupiter. *Nature* **331**, 693–696.
- Massie, S. T. and D. M. Hunten, 1982: Conversion of *para* and *ortho* hydrogen in the Jovian planets. *Icarus* **49**, 213–226.
- Maxworthy, T. and L. G. Redekopp, 1976: A solitary wave theory of the Great Red Spot and other observed features in the Jovian atmosphere. *Icarus* **29**, 261–271.

- Mitchell, J. L., R. F. Beebe, A. P. Ingersoll and G.W. Garneau, 1981: Flow fields within Jupiter's Great Red Spot and White Oval BC. *J. Geophys. Res.* **86**, 8751-8757.
- Palmén, E. and C. W. Newton, 1969: *Atmospheric Circulation Systems*. Academic Press, New York.
- Pedlosky, J., 1987: *Geophysical Fluid Dynamics, Second Edition*. Springer-Verlag, New York.
- Pollack, J. B., M. Podolak, P. Bodenheimer and B. Christofferson, 1986: Planetary dissolution in the envelopes of the forming, giant planets. *Icarus* **67**, 409-443.
- Read, P. L., 1986: Stable, baroclinic eddies on Jupiter and Saturn: A laboratory analog and some observational test. *Icarus* **65**, 304-334.
- Read, P. L. and R. Hide, 1984: An isolated baroclinic eddy as a laboratory analogue of the Great Red Spot on Jupiter. *Nature* **308**, 45-48.
- Riehl, H. and J. S. Malkus, 1958: On the heat balance in the equatorial trough zone. *Geophysica* **6**, 503-537.
- Weidenschilling, S. J. and J. S. Lewis, 1973: Atmospheric and cloud structures of the Jovian planets. *Icarus* **20**, 465-476..
- West, R. A., D. F. Strobel and M. G. Tomasko, 1986: Clouds, aerosols and photochemistry in the Jovian atmosphere. *Icarus* **65**, 161-217.
- Williams, G. P., 1975: Jupiter's atmospheric circulation. *Nature* **257**, 778.
- Williams, G. P., 1979: Planetary Circulations: 2. The Jovian quasi-geostrophic regime. *J. Atmos. Sci.* **36**, 932-968.
- Williams, G. P. and R. J. Wilson, 1988: The stability and genesis of Rossby vortices. *J. Atmos. Sci.* **45**, 207-241.

Williams, G. P. and T. Yamagata, 1984: Geostrophic regimes, intermediate solitary vortices and Jovian eddies. *J. Atmos. Sci.* **41**, 453–478.

Paper 2

Numerical Simulation of Baroclinic Jovian Vortices

Numerical Simulation of Baroclinic Jovian Vortices

Richard K. Achterberg and Andrew P. Ingersoll

Division of Geological and Planetary Sciences
California Institute of Technology
Pasadena, California 91125

To be submitted to *Journal of the Atmospheric Sciences*

Abstract

We examine the evolution of baroclinic vortices in a time dependent, nonlinear numerical model of a Jovian atmosphere. The model uses a normal-mode expansion in the vertical, using the barotropic and first two baroclinic modes (Achterberg and Ingersoll 1989). Our results for the stability of baroclinic vortices on an f -plane in the absence of a mean zonal flow are consistent with previous results in the literature, although the presence of the deep fluid interior on the Jovian planets appears to shift the stability boundaries to smaller length scales. The presence of a mean zonal shear flow acts to stabilize vortices against instability, significantly modifies the finite amplitude form of baroclinic instabilities, and combined with internal barotropic instability (Gent and McWilliams 1986) produces periodic oscillations in the latitude and longitude of the vortex as observed at the level of the cloud tops. This instability may explain some, but not all, observations of longitudinal oscillations of vortices on the outer planets. Oscillations in aspect ratio and orientation of stable elliptical vortices in a zonal shear flow are observed in this baroclinic model, as in simpler two-dimensional models (Kida 1981). The meridional propagation and decay of vortices on a β -plane is inhibited by the presence of a mean zonal flow. The direction of propagation of a vortex relative to the mean zonal flow depends upon the sign of the meridional potential vorticity gradient; combined with observations of vortex drift rates, this may provide a constraint on model assumption for the flow in the deep interior of Jupiter.

2.1. Introduction

One of the characteristic features of the atmosphere of Jupiter is the large number of long-lived spots, ranging in size from the Great Red Spot (GRS), about 25,000 km in length, down to the limits of resolution of the *Voyager* spacecraft (Smith *et al.* 1979a,b). Spots also exist on Saturn (Ingersoll *et al.* 1984) and Neptune (Smith *et al.* 1989), but are not as common on these planets as on Jupiter. Groundbased and spacecraft observations have determined many properties that should be explained by theoretical models of the spots:

a) Most spots are long-lived; the GRS has existed for over 300 years, and the White Ovals have survived for the last 50 years (Peek 1958), while the smaller spots observed by *Voyager* usually lasted for the duration of the observations (60 days) unless they interacted with each other or with other structures (Mac Low and Ingersoll 1986).

b) Spots exist in zonal shears, with the vorticity of the zonal flow being of the same sign as the vorticity of the spot. The vorticity of the GRS and White Oval BC (Mitchell *et al.* 1981) and of the brown barges (Hatzes *et al.* 1981) is greater than the vorticity of the mean zonal winds.

c) Ninety percent of spots are anticyclonic.

d) Interactions between spots usually lead to merging of the spots (Mac Low and Ingersoll 1986).

e) The smallest spots are nearly circular, while larger spots are more elliptical. The largest spots are roughly twice as large in longitude as in latitude (Mac Low and Ingersoll 1986)

f) Some spots display periodic variations in their aspect ratio and orientation of the major axis. The total area of the spot is conserved during the oscillations. These oscillations have been observed in detail for a brown barge on Jupiter (Hatzes

et al. 1981) and for the Great Dark Spot on Neptune (Smith *et al.* 1989; Polvani *et al.* 1990).

g) A few spots have been observed to oscillate in longitude when the mean motion of the spot is removed. The best known example is the Great Red Spot, which oscillates in longitude about its mean motion with a period of just under 90 days and an amplitude of about 1 degree (e.g., Reese 1972). This oscillation persists even when the long term mean motion of the GRS changes drastically. Other examples of longitudinal oscillations will be discussed later in this paper.

Numerous models have been proposed to explain these spots, usually concentrating on the GRS, but none of them can explain all of the observations. Early models postulated that the GRS was the upper end of a Taylor column forced by a topographic feature on the surface (Hide 1961; Ingersoll 1969). Because current models of Jupiter indicate that there is no solid surface (e.g., Stevenson 1982), the Taylor column models of the GRS are not viable. Most of the more recent models consider spots as free-mode, inviscid solutions, usually in the quasi-geostrophic approximation, with various different assumptions about both the variations of Jupiter's mean zonal flow with altitude and the mechanism which maintains the vortices against dissipation and Rossby wave dispersion.

Maxworthy and Redekopp (1976) modeled the GRS as a weakly nonlinear soliton (their calculations are carried to first order in the amplitude of the vortex for long wavelengths, resulting in a modified Korteweg-deVries equation for the amplitude of the vortex as a function of longitude) in a zonal shear flow using the quasi-geostrophic approximation with rigid upper and lower boundaries. The vortex is maintained against dissipation by absorbing energy directly from the zonal flow, which is barotropically unstable. The interaction of two solitons results in their passing through each other unchanged except for a shift in position. This contradicts the

observation that vortex interactions usually lead to merging of the vortices (Mac Low and Ingersoll 1986).

The “modon” model of Ingersoll and Cuong (1981) used a quasi-geostrophic $1\frac{1}{2}$ layer model in which the zonal flow in the observed atmosphere continues into the deep interior unmodified. If the length scales of both the flow and the vortex are larger than the radius of deformation, then the zonal flow is stable and it is possible to find exact, strongly nonlinear, steady and stable solutions in which the potential vorticity is a multivalued function of the streamfunction. In this model, as in the soliton model, the nonlinearity is necessary in order to balance the effects of Rossby wave dispersion. Ingersoll and Cuong showed that the interaction of two modon solutions results in a merger of the two vortices, and postulated that large vortices on Jupiter are maintained against dissipation by the absorption of smaller vortices.

Williams and Yamagata (1984) argue that the GRS and other large vortices are too large to be modeled by quasi-geostrophic dynamics, but instead belong in the “intermediate geostrophic” regime, which they derive for the shallow water equations with a flat lower boundary. They argue that vortices are the fundamental solutions to the intermediate geostrophic equations. They also show that anticyclonic vortices are more stable than cyclonic vortices in the intermediate geostrophic approximation, and that the interaction between two intermediate geostrophic vortices results in the vortices merging together. The difference between cyclonic and anticyclonic vortices, as well as the merging of vortices, has also been observed in laboratory experiments of vortices larger than the Rossby deformation radius (Nezlin *et al.* 1990). Williams and Yamagata propose that the GRS was formed by, and is maintained against dissipation by, a weak barotropic instability of the mean zonal flow. Formation of a GRS-like vortex by barotropic instability has also been demonstrated by Williams and Wilson (1988) and Dowling and Ingersoll (1989), the latter using the observed zonal flow with

bottom topography derived from a vorticity analysis of the GRS and White Oval BC.

Read and Hide (1983 1984; and discussed in more detail in Read 1986) propose that Jovian vortices result from baroclinic instability of the mean flow, based upon an analogy to laboratory experiments on sloping convection in an internally heated fluid in a rotating annulus. Furthermore, Read (1986) demonstrates that the vortices seen in numerical simulations of the annulus experiments are very nearly free mode solutions to the inviscid equations of motion (i.e., modons), with the deviations from the free mode solution caused by the baroclinic forcing.

Marcus (1988, 1990) uses an equivalent barotropic quasi-geostrophic model with a mean zonal flow with approximately constant background potential vorticity when averaged over large scales. He finds, using a numerical model, that patches of anomalous potential vorticity of the same sign as the vorticity of the background flow eventually merge together to form a single large vortex embedded in a turbulent zonal flow. Similar behaviour has been observed in laboratory experiments of vortices in a rotating annulus (Sommeria *et al.* 1988; Meyers *et al.* 1989).

The majority of these models use a $1\frac{1}{2}$ layer model, with a single thin layer of constant density over an infinitely deep layer of slightly higher density; motions in the deep layer are assumed to be a function only of latitude. Such a model is dynamically equivalent to a reduced gravity single layer model with bottom topography. Such models do not allow for processes which require vertical variations of the velocity field, most notably baroclinic instability. Those models of Jovian atmospheric dynamics which are baroclinic use a solid lower boundary instead of a fluid interior.

In this paper, we will be concerned primarily with the nonlinear stability and long-term survival of vortices in a quasi-geostrophic baroclinic model with two degrees of freedom in the vertical and a fluid lower boundary. Of particular interest are the stability of equivalent barotropic vortices in a model with a more complicated

vertical structure, and the conditions under which long-lived vortices can exist. We also wish to investigate using vortices as a probe of the vertical structure of Jupiter's atmosphere. If we find that a distinctive behavior occurs only for vortices within a certain size range relative to the radius of deformation, then an observation of a vortex on Jupiter which exhibits that behavior can be used to constrain Jupiter's radius of deformation. Similarly, vortices might also provide limits on the mean zonal velocity below the observed clouds.

We find that stable or apparently stable vortices exist over the range of sizes considered in our model, but that equivalent barotropic vortices can be unstable in a baroclinic model if the diameter of the vortex is smaller than the deformation radius. Furthermore, this instability may explain some of the observations of vortices which oscillate in longitude, and thus provide limits on Jupiter's radius of deformation. We also find that the decay of vortices by the radiation of Rossby waves can be inhibited by the presence of the mean zonal flow. In addition, the direction that vortices propagate relative to the zonal flow depends upon the sign of the meridional potential vorticity gradient. Observations of vortex drift rates may thus be useful for testing assumptions about the zonal flow below the observed cloud layer.

This paper is organized as follows. In Section 2.2 we briefly describe our numerical model, which uses a normal-mode expansion in the vertical. A more detailed derivation of the normal-mode expansion for Jovian atmospheres is given in Achterberg and Ingersoll (1989). Section 2.3 discusses the stability of baroclinic vortices on an f -plane (ignoring the meridional variation of the Coriolis parameter) in the absence of a mean zonal flow. The effects of adding a mean zonal upon the stability of vortices is examined in Section 2.4. Section 2.5 looks at the effects of a meridional potential vorticity gradient (the β effect). Comparison of the model with observations of the outer planets is done in Section 2.6.

2.2. Model Description

Our model is based on the quasi-geostrophic equation for the conservation of potential vorticity on the β -plane. This is given in log-pressure coordinates as: (e.g., Pedlosky 1987)

$$\frac{D}{Dt} (\nabla^2 \psi + \beta y + \mathcal{L}\psi) = 0, \quad (2.1)$$

where

$$\begin{aligned} \mathcal{L}a &= e^z \frac{\partial}{\partial z} \left(\frac{e^{-z}}{L_D^2} \frac{\partial a}{\partial z} \right), \\ \frac{Da}{Dt} &= \frac{\partial a}{\partial t} + J(\psi, a), \\ J(a, b) &= \frac{\partial a}{\partial x} \frac{\partial b}{\partial y} - \frac{\partial a}{\partial y} \frac{\partial b}{\partial x}. \end{aligned} \quad (2.2)$$

Here ψ is the geostrophic streamfunction, D/Dt is the advective derivative, $z \equiv -\ln(p/p_1)$ with p_1 a reference pressure level, $L_D(z) = NH/f_0$ is the local internal deformation radius, N is the Brunt-Väisälä frequency, $H = RT/g$ is the pressure scale height, T is the temperature, R is the gas constant, g is the gravitational acceleration, and $f = f_0 + \beta y$ is the Coriolis parameter.

We use a normal-mode expansion in the vertical coordinate, in which the streamfunction is written as

$$\psi(x, y, z, t) = \sum_{n=0}^N \psi_n(x, y, t) \Phi_n(z), \quad (2.3)$$

where the functions $\Phi_n(z)$ are the eigenfunctions of the vertical operator in the equations of motion:

$$\mathcal{L}\Phi_n + \lambda_n^2 \Phi_n = 0. \quad (2.4)$$

This equation can be derived by a separation of variables on the linearized form of (2.2), and describes the vertical structure of Rossby waves in an atmosphere at rest. λ_n^{-1} is called the radius of deformation of the n^{th} mode, or the n^{th} internal deformation radius.

For a Jovian atmosphere, with a thin, stably-stratified weather layer ($z_1 < z < z_2$) lying hydrostatically above a very deep, neutrally-stratified, fluid interior ($z_0 < z < z_1$) with $z_1 - z_0 \gg z_2 - z_1$, the baroclinic ($n \geq 1$) modes are confined to the weather layer with $\Phi_n = 0$ for $z \leq z_1$, while the barotropic ($n = 0$) mode has constant amplitude in both the weather layer and interior, with $\Phi_0 = 1$ for $z_0 < z < z_2$ (Achterberg and Ingersoll 1989). The equation for the time evolution of mode n is obtained by inserting (2.4) into (2.1), multiplying by Φ_n , and integrating from z_0 to z_2 . This gives

$$\frac{\partial}{\partial t} (\nabla^2 \psi_0) + \beta \frac{\partial \psi_0}{\partial x} + J(\psi_0, \nabla^2 \psi_0) = 0, \quad (2.5)$$

for the barotropic mode, and

$$\begin{aligned} \frac{\partial}{\partial t} (\nabla^2 \psi_n - \lambda_n^2 \psi_n) + \beta \frac{\partial \psi_n}{\partial x} + J(\psi_0, \nabla^2 \psi_n - \lambda_n^2 \psi_n) \\ + J(\psi_n, \nabla^2 \psi_0) + \sum_{l,m=1}^N \gamma_{lmn} J(\psi_l, \nabla^2 \psi_m - \lambda_m^2 \psi_m) = 0 \end{aligned} \quad (2.6)$$

for the baroclinic modes, where the interaction coefficients γ_{lmn} are given by

$$\gamma_{lmn} = \int_{z_1}^{z_2} e^{-(z-z_1)} \Phi_l \Phi_m \Phi_n dz.$$

The quantity $q_n \equiv \nabla^2 \psi_n - \lambda_n^2 \psi_n$ is the potential vorticity of the n^{th} mode. The potential vorticity at a given altitude $q(z)$ is calculated by summing over the potential vorticity of each mode and adding in the term due to β :

$$q(z) = \beta y + \sum_{n=0}^N (\nabla^2 \psi_n - \lambda_n^2 \psi_n) \Phi_n(z),$$

noting that $\lambda_0^2 = 0$.

The barotropic mode is unaffected by the baroclinic modes (i.e., the motions in the interior are not affected by motion in the visible atmosphere), although the baroclinic modes are affected by the barotropic mode. Because in this paper we are interested only in the motions in the weather layer, we do not solve (2.5), but assume

Table 2.1. Parameters for Normal-Mode Model of Jupiter.

λ_2/λ_1	=	4.50
γ_{111}	=	1.176
γ_{112}	=	-0.1506
γ_{122}	=	0.8125
γ_{222}	=	1.365

that motions in the interior are zonally symmetric such that $\psi_0 = \psi_0(y)$, which is a solution to (2.5). The barotropic mode then represents the effect of motions in the fluid interior upon motions in the weather layer.

A model with $N = 1$, using only the barotropic mode and a single baroclinic mode, is dynamically equivalent to the reduced-gravity, quasi-geostrophic shallow water model (Achterberg and Ingersoll 1989) which has often been used to study Jovian vortices. In this paper we use the barotropic mode and the lowest two baroclinic modes ($N = 2$), which allows for the possibility of baroclinic instability and for motions in the weather layer that are variable with altitude. The structures of the modes $\Phi_n(z)$, interaction coefficients γ_{lmn} , and ratio of second internal deformation radius to first internal deformation radius $\lambda_2^{-1}/\lambda_1^{-1}$ are taken from the model of Achterberg and Ingersoll (1989) with a molar mixing ratio for water of 10^{-3} and frozen equilibrium for the *ortho-parahydrogen* conversion. The structure of the modes is shown in Fig. 2.1, and the interaction coefficients are given in Table 2.1.

The equations as used in this paper have been non-dimensionalized by a length scale L and velocity scale U , chosen such that model vortices have unit radius and amplitude. The non-dimensional variables can be related to dimensional variables through the relations $x_d = Lx$, $t_d = (L/U)t$, $\psi_d = LU\psi$, $\beta_d = (U/L^2)\beta$ and $\lambda_d = \lambda/L$, where the dimensional variables are denoted by the d subscript.

We solve (2.6) numerically using second-order centered finite-differences, with the energy- and enstrophy-conserving Jacobian of Arakawa (1966). The time integration uses leapfrog time steps, followed every 20 steps by a pair of leapfrog trapezoidal

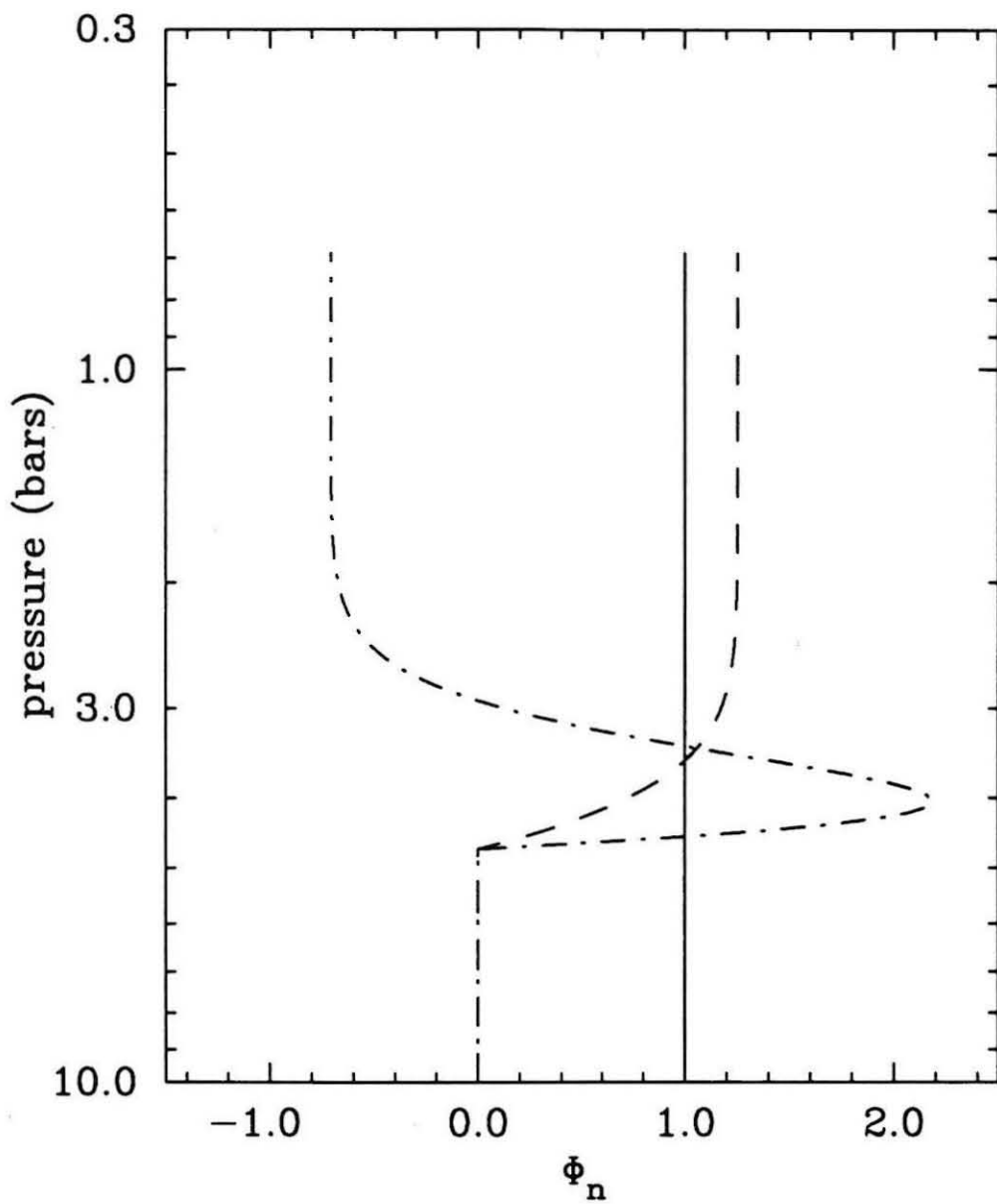
time steps, which provide damping of the computational mode (Haltiner and Williams 1980). For long integrations (more than 8000 timesteps), an eddy viscosity term of the form $\nu \nabla^4 \psi_n$ is added to the right hand side of (2.6), with $\nu = 10^{-5}$. Repeating calculations with different values of ν showed no change in the qualitative behavior of the solutions. The domain is a channel with $0 \leq y \leq 3\pi$; the width of the channel in x is usually $0 \leq x \leq 3\pi$, although $0 \leq x \leq 6\pi$ is sometimes used. Most simulations were done on an 128 by 128 grid, which gives a resolution of $\delta x = 0.074$. Some simulations were done on a 64 by 64 grid, and a few simulations were done on a 256 by 256 grid. Boundary conditions are periodic in x and free-slip in y . Boundary conditions at $y = 0, 3\pi$ are $d\psi_n/dx = 0$ and $\partial^2 \bar{\psi}_n / \partial t \partial y = 0$, where the overbar indicates a zonal average; the first condition is equivalent to no normal flow at the boundary, the second condition prevents any energy flux across the boundary.

Equation (2.6) does not conserve the energy of the weather layer unless $\psi_0 = 0$, as the deep interior can act as a source or sink of energy. Thus, "conservation" of energy by the numerical model is checked by comparing the rate of change of the total energy of the model with the expected value of dE/dt calculated from the streamfunction; these usually agree to within a factor of a few times 10^{-4} of the expected value.

2.3. Vortices on an *f*-plane With No Zonal Flow

We begin by considering the non-linear evolution of isolated vortices on an *f*-plane in the absence of a mean zonal flow. The stability of vortices on an *f*-plane with no zonal flow has received considerable attention, primarily in the context of the stability of oceanic eddies. The most comprehensive study of the linear stability of baroclinic vortices is by Flierl (1988), using a two-mode contour dynamics model, with piecewise constant potential vorticity at all levels and solid upper and lower boundaries. He finds that vortices sufficiently larger than the first internal deformation radius and

Figure 2.1. Structure of the barotropic and first two baroclinic modes $\Phi_n(z)$ for $n = 0$ (solid line), $n = 1$ (dashed line) and $n = 2$ (dot-dashed line).



with a significant baroclinic component are baroclinically unstable, and that vortices smaller than the deformation radius and with the same sign of vorticity at all altitudes are subject to a form of barotropic instability which results in the tilting and twisting of the vertical axis of the vortex. Nonlinear numerical calculations by Helfrich and Send (1988) with a two layer contour dynamics model show that the barotropic instability results in the breakup of the vortex into multiple dipolar structures. Calculations of the linear stability and nonlinear evolution of f -plane vortices with continuous vorticity distributions, but over narrow ranges of parameter space, have been done by Ikeda (1981) in a two layer model of vortices larger than the deformation radius and with the vortex strongest in the upper layer, and by Gent and McWilliams (1986) for equivalent barotropic vortices, although they allowed the unstable modes to have a baroclinic structure. Ikeda (1981) found that sufficiently large vortices are subject to baroclinic instability, and that if the linear growth rate was large enough the instability resulted in the breakup of the vortex. For smaller growth rates, he found that after initially becoming elliptical, the vortex returned to a circular shape while smaller vortices of opposite sign formed on either side of the original vortex. Gent and McWilliams (1986) found that small enough barotropic vortices are subject to a form of barotropic instability, which they called internal barotropic instability, that results in the vortex breaking up into two separate vortices at different altitudes. The primary difference between these models and ours, is our lower boundary condition: we have a fluid lower boundary instead of a solid lower boundary. Also, we cover a larger range of parameter space than either Ikeda or Gent and McWilliams.

To examine the non-linear stability of isolated f -plane vortices in our Jovian model, we follow the time evolution of a nearly circular vortex, using the numerical methods described in section 2. The initial condition is a Gaussian streamfunction of

unit radius with an elliptical perturbation and no mean zonal flow, given by

$$\psi_n = A_n * \exp \left(- \left(\frac{x}{1.05} \right)^2 - \left(\frac{y}{0.95} \right)^2 \right) \quad \text{for } n = 1, 2 \quad (2.7)$$

and $\psi_0 = 0$. The slight elliptical perturbation has been included to excite any instability. With this initial condition we have two independent parameters: λ_1 , the size of the initial vortex divided by the first internal deformation radius, and the vertical structure of the initial vortex, given by the ratio of the amplitude of the second baroclinic mode of the initial vortex to the amplitude of the first baroclinic mode of the initial vortex, which we call $s \equiv A_2/A_1$. $s = 0$ represents an equivalent barotropic vortex and increasing the magnitude of s increases the baroclinicity of the vortex. Vortices with $-0.214 \leq s \leq 1.769$ have the same sign of vorticity at all altitudes. Vortices with $s \approx -0.214$ are confined in the vertical to altitudes above the 3 bar pressure level, while vortices with $s \approx -1.769$ are confined to between the base of the water cloud and about 3 bars, with very little amplitude at the level of the observed clouds. Vortices with $-1.25 \lesssim s \lesssim 0.1$ are strongest at the level of the observed clouds, and vortices outside this range are strongest at a pressure level around 4 bars in the region of the water cloud. The actual mode amplitudes of the initial vortex are determined by requiring that $A_1^2 + A_2^2 = 1$ and that $A_1 > 0$. Numerical simulations were performed for $0.01 \leq \lambda_1^2 \leq 3$, and $-2 \leq s \leq 2$. This covers vortices with diameters ranging from one-fifth of the first internal deformation radius up to about four times the first internal deformation radius. The deformation radius on Jupiter is unknown, but has been estimated to be in the range of 500 to 5000 kilometers, with the most likely value on the order of 1000 km (Achterberg and Ingersoll 1989). Thus our simulations cover vortices ranging in size from the smallest observed vortices up to a few thousand kilometers. Our simulations do not reach the size of the very largest vortices (the GRS and White Ovals); using values of $\lambda_1^2 \gtrsim 3$ in our models is impractical, as it requires a prohibitively small grid spacing to adequately resolve the

deformation radius of the second baroclinic mode.

We find four different types of behavior, depending upon the parameters s and λ_1^2 : horizontal fragmentation of the initial vortex, usually into two dipoles; elongation of the vortex, followed by a decrease in eccentricity and generation of a tripolar structure, very similar to the rapidly/slowly deformed ring found by Ikeda (1981); vertical breakup of the vortex into separate vortices at different altitudes, an example of the internal barotropic instability discovered by Gent and McWilliams (1986); and long-term stability in which the initial vortex persists for tens of rotations with little change. Each of these is discussed in more detail below.

2.3.1 *Horizontal Fragmentation*

Figure 2.2 shows the time evolution of the streamfunction and potential vorticity respectively for the case $s = -2$ and $\lambda_1^2 = 1$, in which the sign of the vorticity changes with altitude. The streamfunction and potential vorticity have been evaluated at two pressure levels: 690 mbar, the top of the model, which corresponds to the altitude of the visible clouds on Jupiter, and 3962 mbar, corresponding to the maximum of the second mode eigenfunction and located in the water clouds. We will refer to the streamfunction (potential vorticity) evaluated at 690 mbar as the “upper layer streamfunction (potential vorticity)” and the streamfunction (potential vorticity) evaluated at 3962 mbar as the “lower layer streamfunction (potential vorticity).” The streamfunction and potential vorticity at these altitudes display qualitatively similar behaviour to the streamfunction and potential vorticity in the upper and lower layers of a two layer model.

The vortex in Fig. 2.2 rapidly elongates, with the upper part of the vortex rotated with respect to the lower part, and pinches off in the center. This results in two dipolar structures, each with a vortex in the upper layer paired with a vortex of opposite-signed vorticity in the lower layer. The dipolar structures then move away

from each other. The two vortices in each layer remain connected by filaments of potential vorticity which stretch out and become thinner as the vortices separate. This breakup into dipoles occurs rapidly, requiring approximately one rotation time of the initial vortex. The breakup of the vortex is accompanied by a decrease in the potential energy of the second baroclinic mode (and in the total potential energy), with a roughly corresponding increase in the kinetic energy of the first baroclinic mode, while the potential energy of the first baroclinic mode and kinetic energy of the second baroclinic mode show slight increases (Fig. 2.3; the derivation of the energy terms for a normal-mode model is outlined in Appendix A). This indicates that the energy source for the instability is baroclinic; the instability is begin driven by the vertical shear of the initial condition. Splitting of the initial vortex into multiple dipoles is observed only when the sign of the vorticity of the original vortex varies with altitude and when $\lambda_1^2 \gtrsim 0.3$ (or equivalently, when the diameter of the vortex is roughly greater than the first internal deformation radius), although not for all vortices which meet these conditions.

2.3.2 Tripole Formation

Figure 2.4 shows the evolution of the streamfunction and potential vorticity for the case $s = -0.5$ and $\lambda_1^2 = 1$, which also has oppositely signed vorticity in the upper and lower layers, but relatively more energy in the first baroclinic mode than the previous case shown in Fig. 2.2. Initially, the upper layer part of the vortex becomes elongated, while the lower layer part of the vortex, which has oppositely signed vorticity from the upper vortex, splits into two smaller vortices. The upper layer vortex then becomes more circular while another vortex with the same sign of vorticity as the upper layer vortex forms between the two lower layer vortices and below the upper layer vortex. This forms a tripolar structure, with a central vortex flanked on either side by two vortices which have the opposite sign of vorticity than the central vortex. This tripolar

Figure 2.2a. Example of horizontal fragmentation. Time evolution of the streamfunction of an f -plane vortex with $s = -2.0$, $\lambda_1^2 = 1.0$ and $U_0 = 0.0$ at times 2.23, 4.45, 6.68 and 8.91. The left column shows the streamfunction evaluated at 690 mbar, and the right column shows the streamfunction evaluated at 3962 mbar. The contour interval is 0.25 and negative contours are dashed.

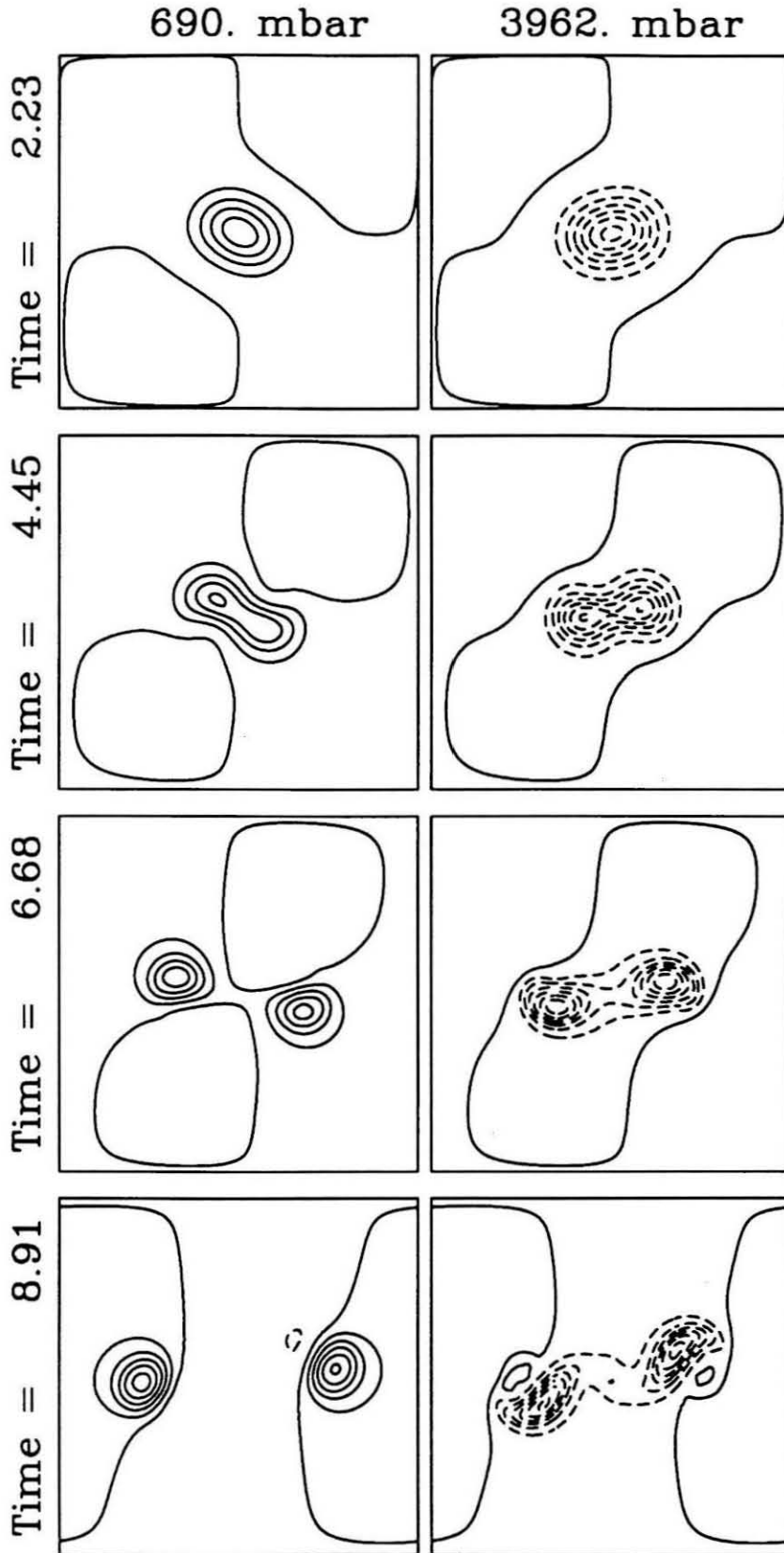


Figure 2.2b. Example of horizontal fragmentation. Time evolution of the potential vorticity of an f -plane vortex with $s = -2.0$, $\lambda_1^2 = 1.0$ and $U_0 = 0.0$ at times 2.23, 4.45, 6.68 and 8.91. The left column shows the potential vorticity evaluated at 690 mbar, with a contour interval of 2.5. The right column shows the potential vorticity evaluated at 3962 mbar, with a contour interval of 5.0. Negative contours are dashed, and the contours straddle 0.

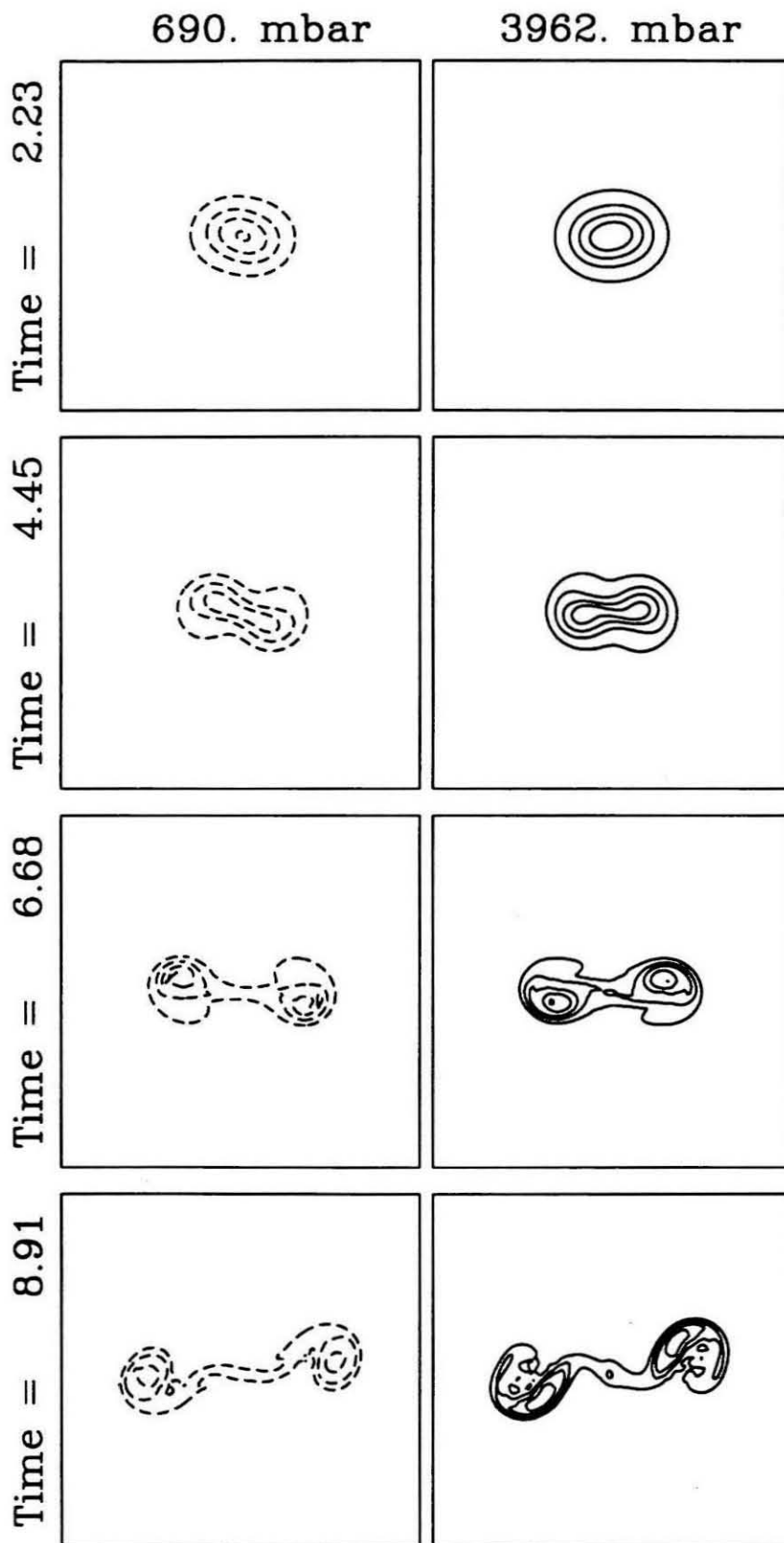


Figure 2.3. Kinetic and potential energy as a function of time for the run shown in Fig. 2.2. The upper panel shows the kinetic energy and the lower panel shows the potential energy. The dashed line is the energy in the first baroclinic mode, the dot-dashed line is the energy in the second baroclinic mode, and the solid line is the sum of the energy in both modes.

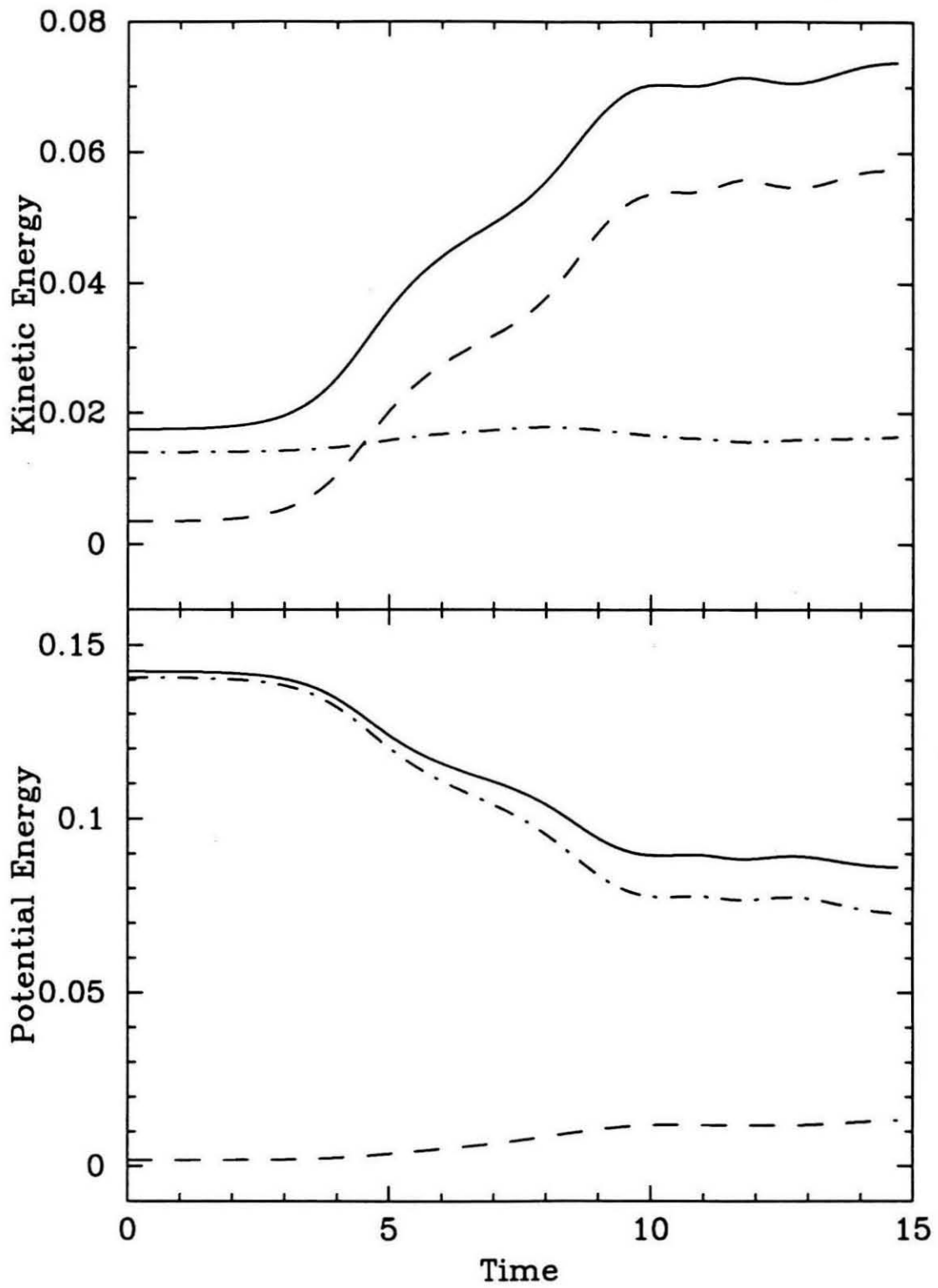


Figure 2.4a. Example of tripole formation. Time evolution of the streamfunction of an f -plane vortex with $s = -0.5$, $\lambda_1^2 = 1.0$ and $U_0 = 0.0$ at times 0.0, 13.36, 26.72 and 40.07. The left column shows the streamfunction evaluated at 690 mbar, and the right column shows the streamfunction evaluated at 3962 mbar. The contour interval is 0.25 and negative contours are dashed.

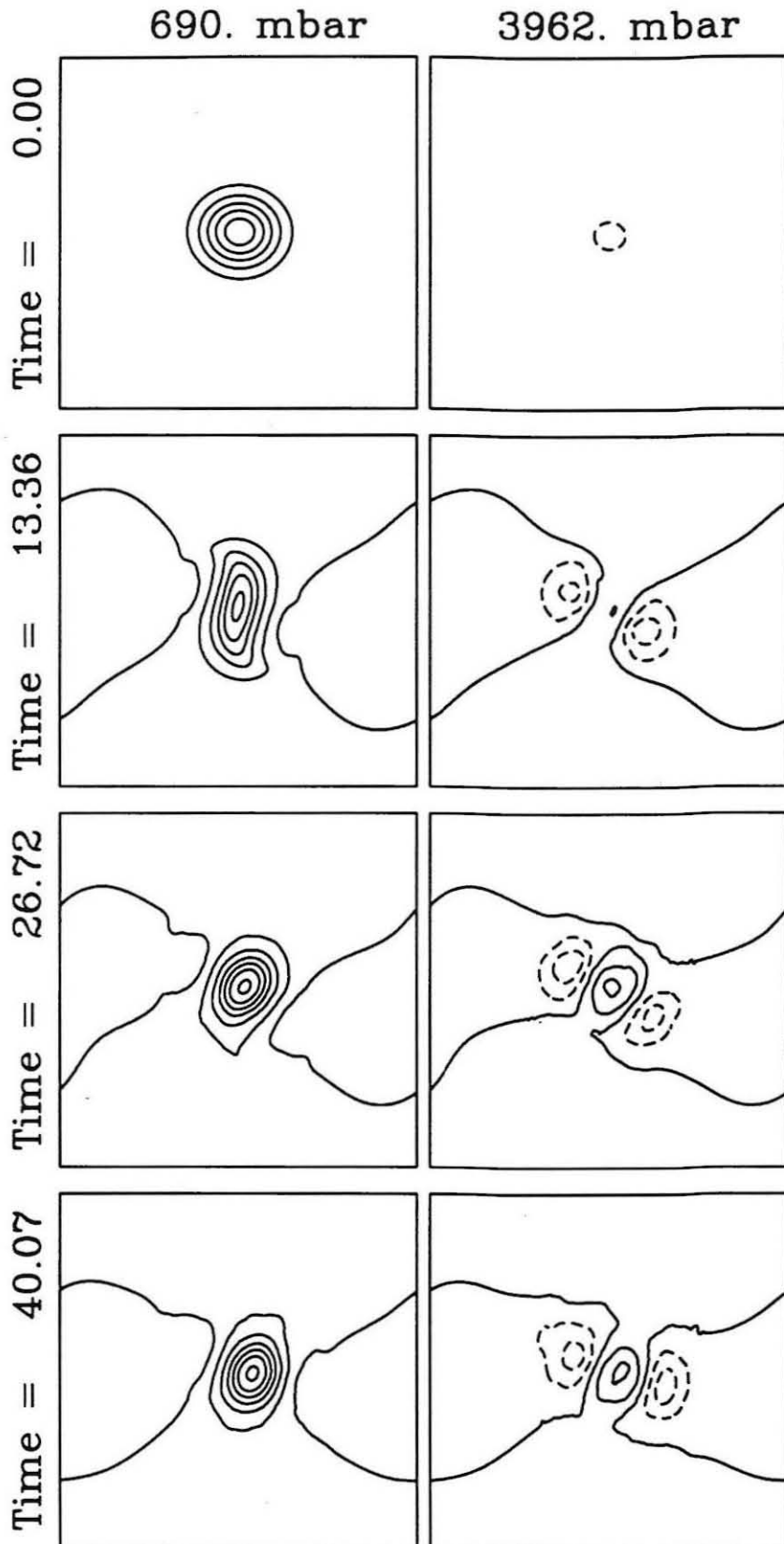


Figure 2.4b. Example of tripole formation. Time evolution of the potential vorticity of an f -plane vortex with $s = -0.5$, $\lambda_1^2 = 1.0$ and $U_0 = 0.0$ at times 0.0, 13.36, 26.72 and 40.07. The left column shows the potential vorticity evaluated at 690 mbar, and the right column shows the potential vorticity evaluated at 3962 mbar. The contour interval is 5.0, negative contours are dashed, and the contours straddle 0.

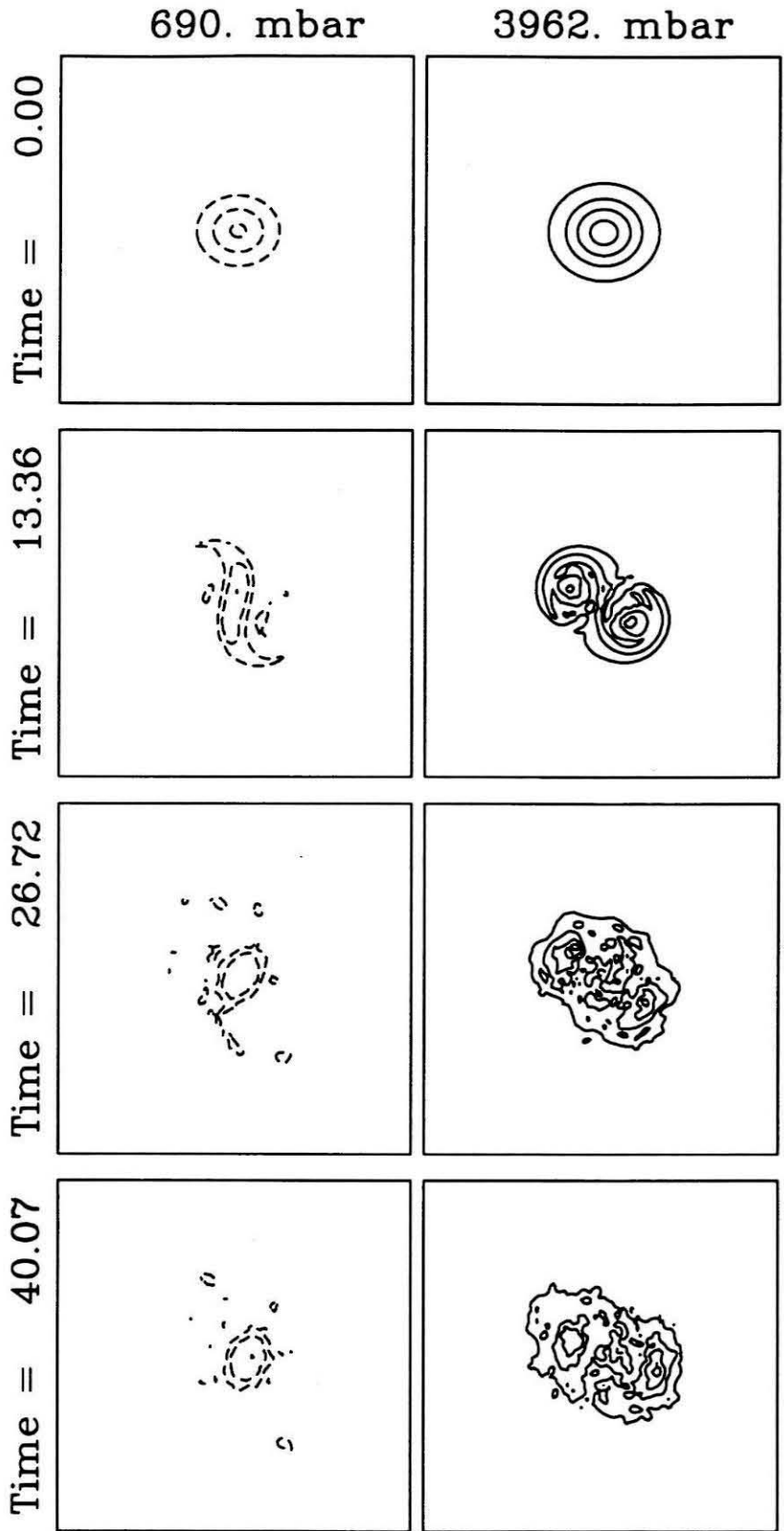
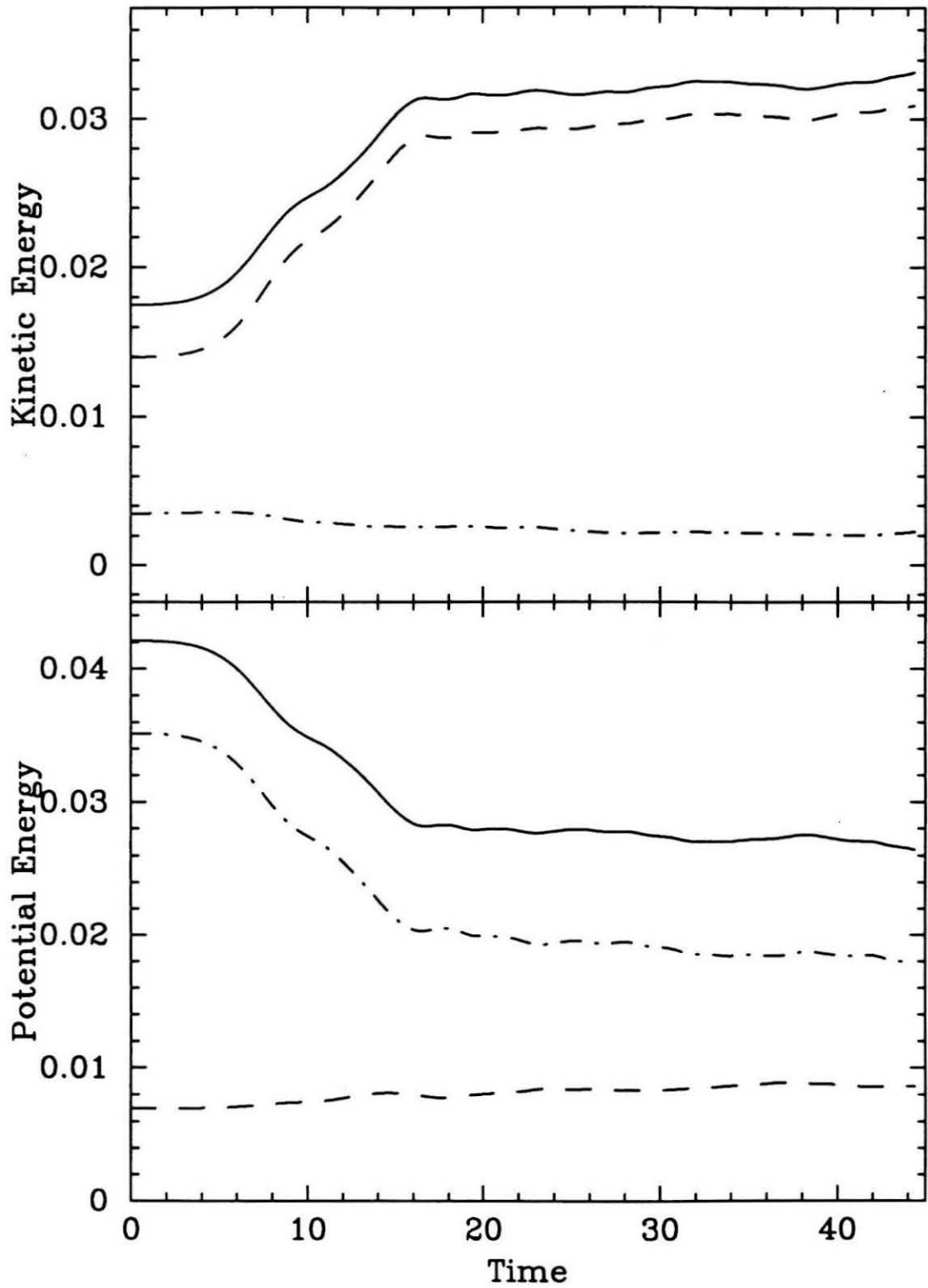


Figure 2.5. Kinetic and potential energy as a function of time for the run shown in Fig. 2.4. The upper panel shows the kinetic energy and the lower panel shows the potential energy. The dashed line is the energy in the first baroclinic mode, the dot-dashed line is the energy in the second baroclinic mode, and the solid line is the sum of the energy in both modes.



structure then rotates as a single unit with little change in structure. The initial stages of this tripole formation are very similar to the initial stages of breakup and dipole formations, except that in tripole formation the lower layer elongates faster than the upper layer and splits while the upper layer is only weakly distorted. Once the lower layer vortex splits, the evolution of the tripole formation is obviously quite different from the evolution of dipole formation. As with horizontal fragmentation, the formation of the tripole is accompanied by a decrease in the potential energy of the second baroclinic mode and increase in the kinetic energy of the first baroclinic mode (Fig. 2.5), suggesting that tripole formation is a form of baroclinic instability.

A similar behavior is seen for some vortices with the same sign of vorticity at all altitudes, but still with a change in sign with altitude of the potential vorticity, as shown in Fig. 2.6 for $s = 1.5$ and $\lambda_1^2 = 1$. In this case, the upper layer vortex becomes stronger, more elongated, and develops a pair of vortices, with vorticity of the opposite sign of the original vortex, on either side of it. As the side vortices develop, the lower layer vortex elongates, and then returns to a more circular shape. The end result is again a tripolar structure.

The relative sizes and vertical structures of the central and flanking vortices depend upon the vertical structure of the initial vortex, and upon the size of the vortex relative to the deformation radius. Decreasing the size of the initial vortex, or decreasing the amplitude of the second mode relative to the first mode, generates smaller flanking vortices (relative to the central vortex) and central vortices with vertical structures closer to the vertical structure of the initial vortex. As with horizontal fragmentations, formation of tripoles occurs only when $\lambda_1^2 \gtrsim 0.3$, and only when the sign of the potential vorticity varies with altitude.

2.3.3 Vertical Fragmentation

Figure 2.7 shows the evolution of the streamfunction for the case $s = 0.5$ and

$\lambda_1^2 = 0.03$. The vertical axis of the vortex becomes tilted, and eventually the upper and lower layer parts of the vortex separate and slowly move away from each other in opposite directions, leaving two separate vortices of limited vertical extent. Splitting of the vortex is accompanied by a decrease in the kinetic energy of the first baroclinic mode and an increase in both the kinetic and potential energies of the second baroclinic mode (Fig. 2.8), indicating that the energy source for the instability is barotropic, and the instability is being driven by the horizontal shear of the initial condition. This behavior is only observed when $\lambda_1^2 \lesssim 0.1$ (diameter of the vortex smaller than about two-thirds of the first internal radius of deformation) and the vortex has the same sign of vorticity in both layers. Under these conditions, vertical fragmentation can occur for equivalent barotropic vortices ($s = 0$). These vortices are representable in the $N = 1$ model, and hence in the common equivalent barotropic models, and are stable in such a model. The timescale for vertical fragmentation is much longer than for horizontal fragmentation, requiring $O(10)$ vortex rotation times.

2.3.4 Discussion

The nonlinear behavior of nearly circular 2-mode Gaussian vortices on an f -plane can be broken down into four classifications: horizontal fragmentation, tripole formations, vertical fragmentation, and stability. Figure 2.9 shows the regions of λ_1^2 - s parameter space over which each of these types of behaviour occurs; a list of runs used to construct this diagram is given in Table 2.2. Horizontal fragmentation and tripole formation occur only for vortices with diameters roughly equal to or larger than the first internal radius of deformation and with a second mode strong enough that the sign of the potential vorticity varies with altitude. Vertical fragmentation occurs only for vortices with diameters smaller than the first internal radius of deformation and with the same sign of vorticity at all altitudes. Stability occurs for vortices with diameters larger than the radius of deformation which are barotropic or

Figure 2.6. Example of tripole formation for a vortex with the same sign of vorticity at all altitudes. Time evolution of the streamfunction of an f -plane vortex with $s = 1.5$, $\lambda_1^2 = 1.0$ and $U_0 = 0.0$ at times 0.0, 12.87, 23.75 and 35.62. The left column shows the streamfunction evaluated at 690 mbar, and the right column shows the streamfunction evaluated at 3962 mbar. The contour interval is 0.25 and negative contours are dashed.

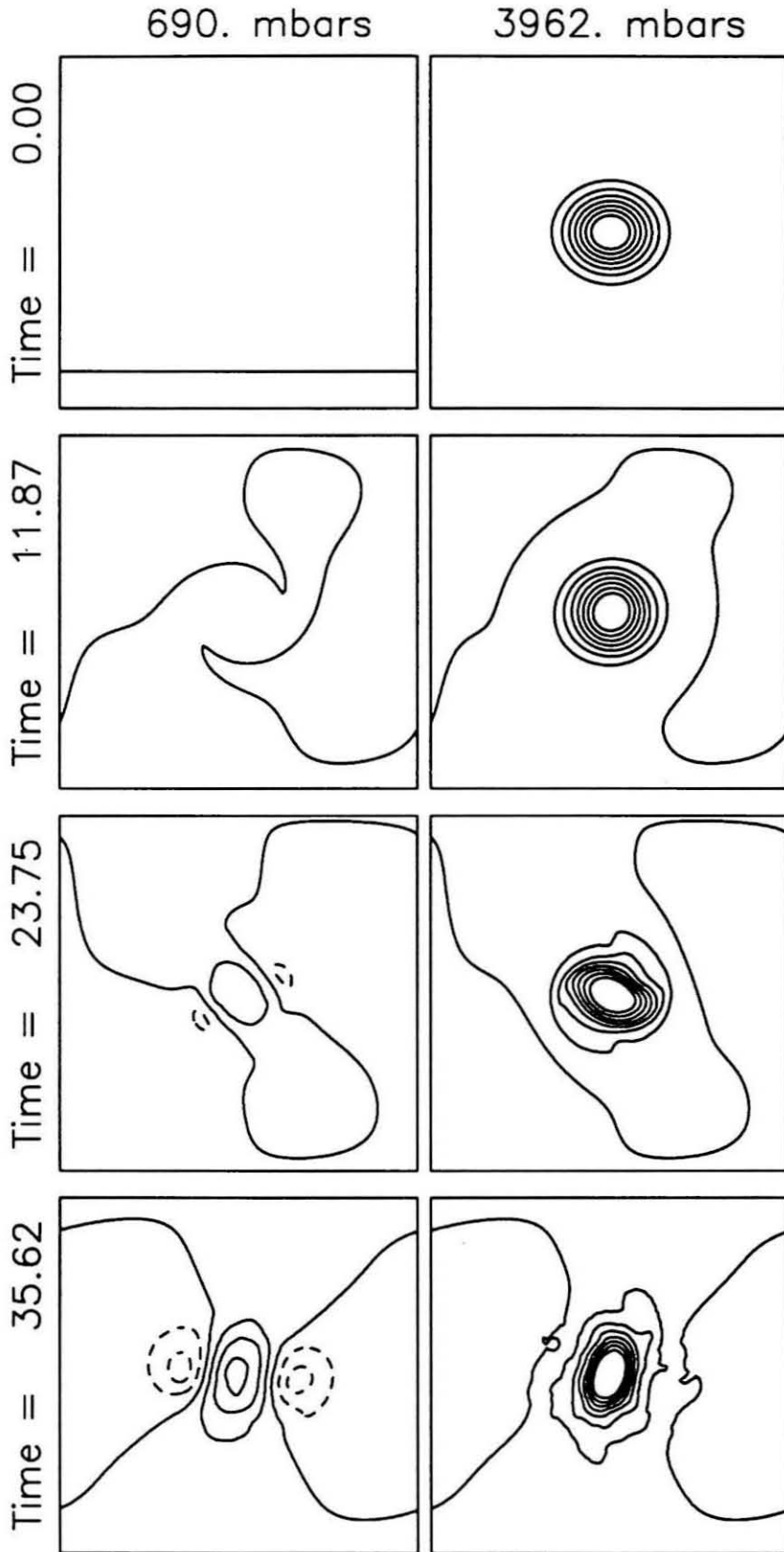


Figure 2.7. Example of vertical fragmentation. Time evolution of the streamfunction of an f -plane vortex with $s = 0.5$, $\lambda_1^2 = 0.03$ and $U_0 = 0.0$ at times 0.0, 35.90, 71.81 and 107.71. The left column shows the streamfunction evaluated at 690 mbar, and the right column shows the streamfunction evaluated at 3962 mbar. The contour interval is 0.25 and negative contours are dashed.

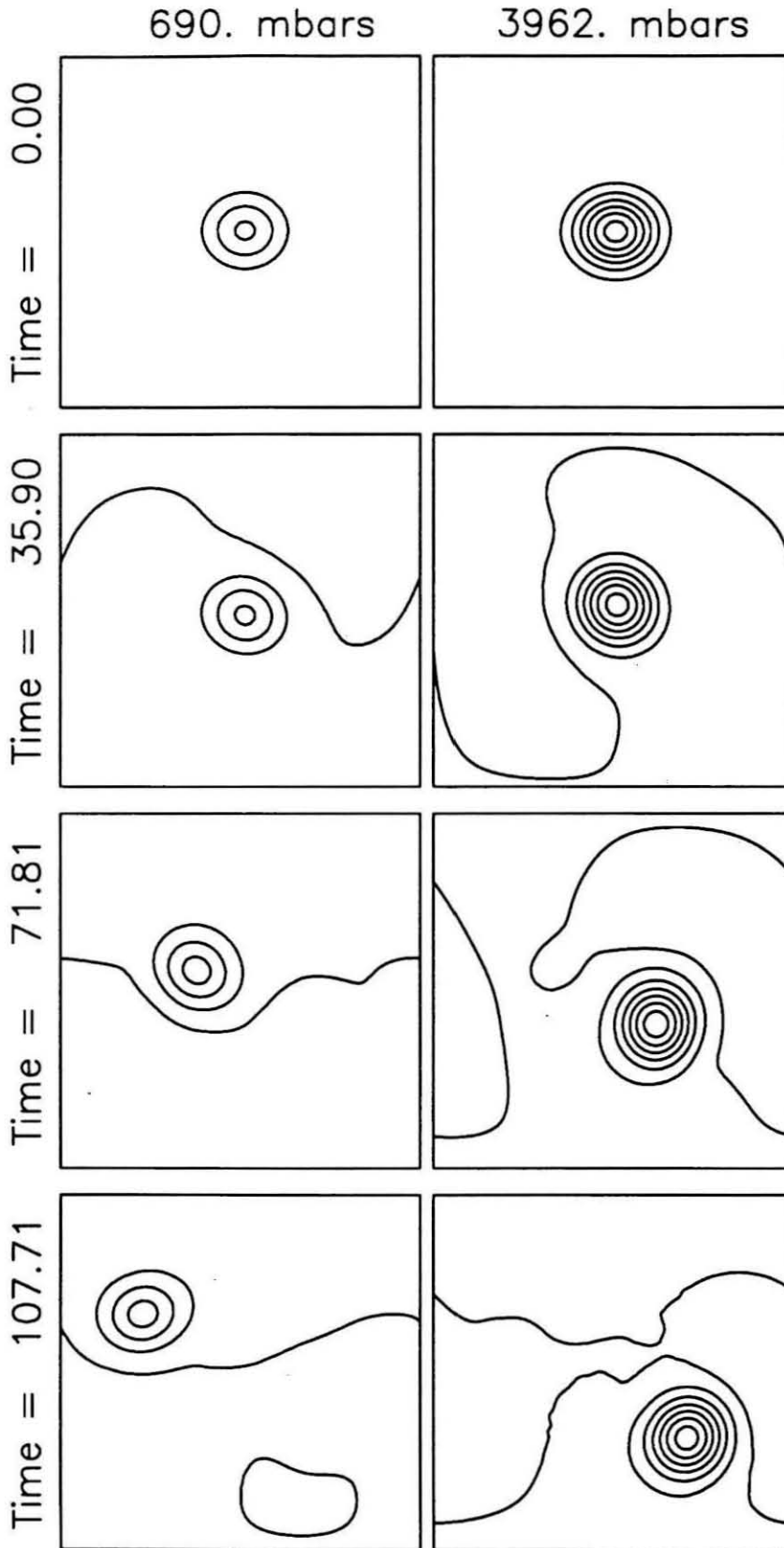


Figure 2.8. Kinetic and potential energy as a function of time for the run shown in Fig. 2.7. The upper panel shows the kinetic energy and the lower panel shows the potential energy. The dashed line is the energy in the first baroclinic mode, the dot-dashed line is the energy in the second baroclinic mode, and the solid line is the sum of the energy in both modes.

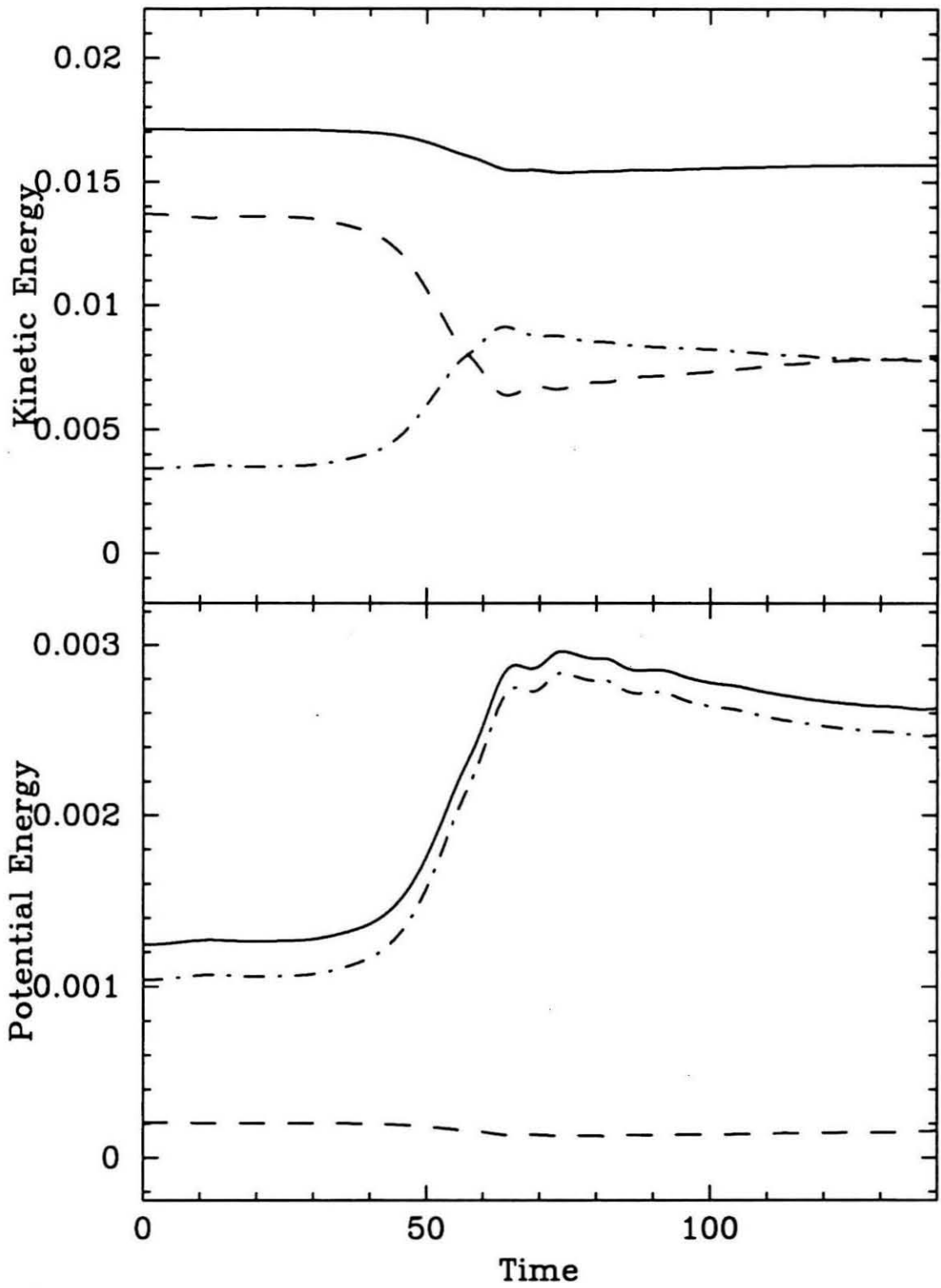
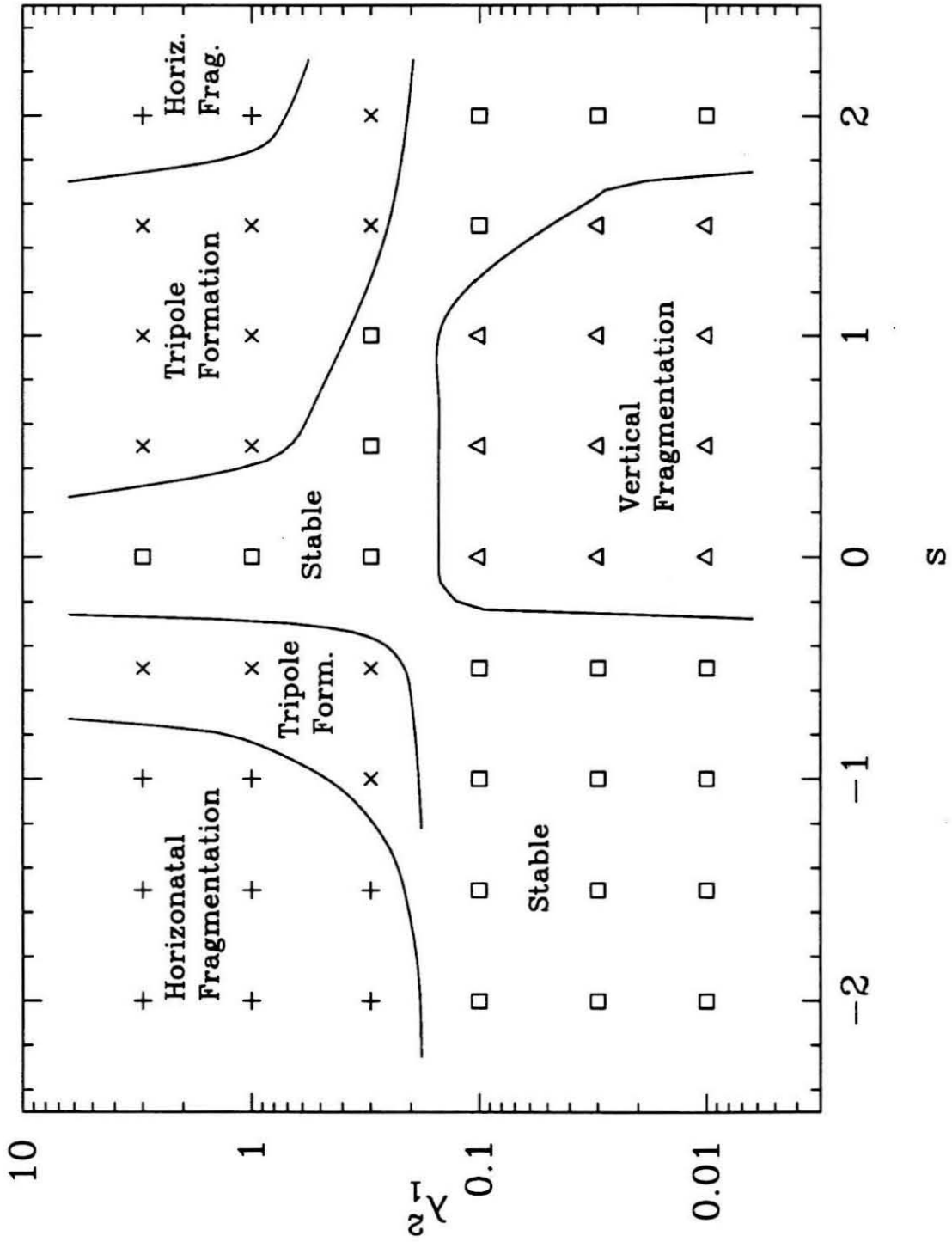


Figure 2.9. Regime diagram for the behavior of vortices on the f -plane with no mean zonal flow. The horizontal axis is the s , the ratio of second baroclinic mode to first baroclinic mode in the initial vortex. The vertical axis is the radius of the vortex relative to the first internal radius of deformation. The open squares (\square) represent stable vortices, which survive to time 400, the plus signs (+) represent horizontal fragmentation (baroclinic instability), the crosses (\times) represent tripole formation, and the open triangles (\triangle) represent vertical fragmentation (internal barotropic instability).



nearly barotropic, and for vortices smaller than the radius of deformation which have vorticity that changes sign with altitude.

These results are qualitatively consistent with the calculations by Flierl (1988) of the linear instability of vortices in a two mode (the barotropic and first baroclinic mode) contour dynamics model with a solid lower boundary. He found that vortices with a strong enough baroclinic component (equivalent to about $|s| \gtrsim 0.5$, with the minimum value of $|s|$ for which instability occurs decreasing as λ_1^2 is increased) are baroclinically unstable if they have a radius larger than about twice the radius of deformation. The exact stability boundaries are dependent upon the assumed vertical stratification. Flierl also found that vortices which have the same sign of vorticity at all altitudes and a radius smaller than about one and one-half times the radius of deformation are subject to an instability which causes a twisting and tilting of the vertical axis of the vortex. This matches our observations that instability occurs for large enough vortices with a strong enough baroclinic component and for small enough vortices with the same sign of vorticity at all altitudes, while large, barotropic vortices are stable. The only major difference is that our stability boundaries occur for a value of λ_1 that is about a factor of four to five times smaller than was found by Flierl. The difference in the location of the stability boundaries could be caused either by differences in the vertical stratification, by our use of a fluid lower boundary while Flierl has a solid lower boundary, or by the differences in the horizontal structure of the vortices (ours have a Gaussian profile for the streamfunction while Flierl uses patches of constant potential vorticity).

Our results may also be compared to those of Ikeda (1981) and Gent and Williams (1986). Ikeda (1981) considered the stability of Gaussian vortices in a two-layer, quasi-geostrophic model with solid lower boundary, considering only vortices that were strongest in the upper (thinner) layer (equivalent to $1.0 \lesssim s \lesssim 1.7$ in our

Table 2.2. *f*-plane Simulations With No Zonal Flow

λ_1^2	s	N_x	N_y	$\Delta t/\Delta x$	length of run
3.0	-2.0	128	128	0.2	59.37
3.0	-1.5	128	128	0.2	59.37
3.0	-1.0	128	128	0.2	59.37
3.0	-0.5	128	128	0.2	59.37
3.0	0.0	128	128	0.4	478.72
3.0	0.5	128	128	0.2	59.37
3.0	1.0	128	128	0.2	59.37
3.0	1.5	128	128	0.2	59.37
3.0	2.0	128	128	0.2	59.37
1.0	-2.0	128	128	0.2	59.37
1.0	-1.5	128	128	0.2	59.37
1.0	-1.0	128	128	0.2	59.37
1.0	-0.5	128	128	0.2	59.37
1.0	0.0	128	128	0.4	478.72
1.0	0.5	128	128	0.2	59.37
1.0	1.0	128	128	0.2	59.37
1.0	1.5	128	128	0.2	59.37
1.0	2.0	128	128	0.2	59.37
0.3	-2.0	128	128	0.4	59.37
0.3	-1.5	128	128	0.4	59.37
0.3	-1.0	128	128	0.4	59.37
0.3	-0.5	128	128	0.4	59.37
0.3	0.0	128	128	0.4	59.37
0.3	0.5	128	128	0.4	478.72
0.3	1.0	128	128	0.4	478.72
0.3	1.5	128	128	0.4	478.72
0.3	2.0	128	128	0.4	118.74
0.1	-2.0	128	128	0.4	59.37
0.1	-2.0	64	64	0.2	478.72
0.1	-1.5	128	128	0.4	59.37
0.1	-1.5	64	64	0.2	478.72
0.1	-1.0	128	128	0.4	59.37
0.1	-1.0	64	64	0.2	478.72
0.1	-0.5	128	128	0.4	59.37
0.1	-0.5	64	64	0.2	478.72
0.1	0.0	128	128	0.4	59.37
0.1	0.0	64	64	0.2	478.72
0.1	0.5	128	128	0.4	59.37
0.1	0.5	64	64	0.2	237.48
0.1	1.0	128	128	0.4	59.37
0.1	1.0	64	64	0.2	478.72
0.1	1.5	128	128	0.4	59.37
0.1	1.5	64	64	0.2	478.72

Table 2.2. (continued)

λ_1^2	s	N_x	N_y	$\Delta t/\Delta x$	length of run
0.1	2.0	128	128	0.4	59.37
0.1	2.0	64	64	0.2	478.72
0.03	-2.0	128	128	0.4	59.37
0.03	-2.0	64	64	0.2	478.72
0.03	-1.5	128	128	0.4	59.37
0.03	-1.5	64	64	0.2	478.72
0.03	-1.0	128	128	0.4	59.37
0.03	-1.0	64	64	0.2	478.72
0.03	-0.5	128	128	0.4	59.37
0.03	-0.5	64	64	0.2	478.72
0.03	0.0	128	128	0.4	59.37
0.03	0.0	64	64	0.2	237.48
0.03	0.5	128	128	0.4	59.37
0.03	0.5	64	64	0.2	237.48
0.03	1.0	128	128	0.4	59.37
0.03	1.0	64	64	0.2	237.48
0.03	1.5	128	128	0.4	59.37
0.03	1.5	64	64	0.2	237.48
0.03	2.0	128	128	0.4	59.37
0.03	2.0	64	64	0.2	478.72
0.01	-2.0	128	128	0.4	59.37
0.01	-2.0	64	64	0.2	478.72
0.01	-1.5	128	128	0.4	59.37
0.01	-1.5	64	64	0.2	478.72
0.01	-1.0	128	128	0.4	59.37
0.01	-1.0	64	64	0.2	478.72
0.01	-0.5	128	128	0.4	59.37
0.01	-0.5	64	64	0.2	478.72
0.01	0.0	128	128	0.4	118.74
0.01	0.0	64	64	0.2	237.48
0.01	0.5	128	128	0.4	59.37
0.01	0.5	64	64	0.2	237.48
0.01	1.0	128	128	0.4	59.37
0.01	1.0	64	64	0.2	237.48
0.01	1.5	128	128	0.4	59.37
0.01	1.5	64	64	0.2	237.48
0.01	2.0	128	128	0.4	59.37
0.01	2.0	64	64	0.2	478.72

model). He classified his nonlinear, initial value results into four groups — the splitting ring, the rapidly deformed ring, the slowly deformed ring, and the calm ring — which he related to the linear growth rates for baroclinic instability. The largest growth rates (most unstable vortices) correspond to the splitting rings, and occur for the largest, most baroclinic vortices. Lower growth rates correspond to the deformed rings, while stable vortices correspond to the calm ring. The evolution of Ikeda's splitting rings results in the formation of two dipolar structures, which is the same behaviour we observe for sufficiently large, sufficiently baroclinic vortices. His deformed rings appear to show the same behaviour as our tripole formation. The initial vortex becomes more elliptical, then returns to a more circular form while two vortices of opposite rotation form on either side (Ikeda's Figs. 11 and 12). As in our models, the tripole formation occurs in the region of parameter space between the stable vortices and complete fragmentation. For a vortex confined to the thinner of his two layers (roughly equivalent to $s \approx 1.7$ in our model) found that baroclinic instability occurs for vortices with radii larger than about twice the radius of deformation. His nonlinear calculations show tripole formation occurring for vortices larger than twice the radius of deformation, changing to horizontal fragmentation for vortices larger than about three and one-half times the radius of deformation.

Gent and McWilliams (1986) considered the stability of barotropic vortices (equal to $s = 0$ in our model), although they allowed the perturbations to be baroclinic. They found that for Gaussian vortices the most unstable mode was baroclinic, and showed in nonlinear numerical simulations using a two-layer model that this instability, which they termed internal barotropic instability, resulted in the vertical fragmentation of the vortex, as also seen in our model. Their linear calculations show that for a Gaussian vortex, the instability occurs for $\lambda_1^2 < 1.6$.

In all the cases discussed above, we find the stability boundaries at values of

λ_1 that are about a factor of five lower than found by the other authors, including those who also used a Gaussian for the radial shape of the initial streamfunction. The most likely explanation is that the other models have a solid lower boundary, while our model has an infinitely deep, neutrally stratified fluid below the levels of interest. In other words, the other models use the barotropic and first baroclinic modes, while we use the first two baroclinic modes. Thus it appears that the effect of a deep, neutrally-stratified, fluid interior on the stability of vortices is to shift the stability boundaries to smaller length scales.

2.4. Effects of a Barotropic Mean Zonal Shear

We now consider the effects of a barotropic shear flow on the solutions obtained in the previous section. To do this, a barotropic mean zonal flow with constant shear is added to the barotropic mode: $\psi_0 = \frac{1}{2}U_0y^2$. This zonal flow has no meridional potential vorticity gradient, and thus will not support Rossby waves. Although such a zonal flow is not realistic for Jupiter, it allows us to examine the effects of a mean zonal flow upon the stability of vortices without having to separate the effects of the shear from the effects of interactions with waves; the effects of a mean zonal potential vorticity gradient (the β effect) will be discussed in the next section. Superimposed upon the zonal flow is a Gaussian vortex as described in the previous section. We now have three independent parameters: λ_1 , s , and U_0 , representing, respectively, the size of the vortex relative to the deformation radius, the vertical structure of the vortex, and the nondimensionalized vorticity of the shear flow. Numerical simulations were performed using the same values of λ_1^2 and s as in section 2, but with $U_0 = 0.5$ and $U_0 = 1.0$. A few simulations were also done with $U_0 = 1.0$ and the amplitude of the first mode $A_1 < 0$, which gives vortices that rotate counter to the flow at the altitude of the observed cloud tops. The effects of the shear on the results of the previous section are discussed below.

2.4.1 Effect of shear on stable f -plane vortices

The behavior of a vortex which is stable on the f -plane when shear is added depends upon the sign of the vorticity. When the vorticity of the vortex has the opposite sign from the vorticity of the background shear flow, the vortex becomes sheared out by the mean flow and is destroyed (Fig. 2.10). This is the same as the behavior in a non-rotating, single layer system of an elliptical patch of constant vorticity embedded in a background flow of constant shear with the opposite sign of vorticity (Kida 1981; Meacham *et al.* 1990). If the initial vortex has a different sign of vorticity at different altitudes, the portion of the vortex rotating counter to the flow is stretched out and destroyed, leaving behind a vortex of limited vertical extent (Fig. 2.11).

A vortex with the same sign of vorticity as the mean flow at all altitudes, and which is stable in the absence of the mean flow, is also stable in the presence of the mean flow. However, the vortex is not, in general, steady; both the aspect ratio and the orientation oscillate quasi-periodically in time with slight variations in amplitude and period. Figure 2.12 shows the time variations of the aspect ratio and orientation of the $q(z = 690 \text{ mbar}) = -1.3$ contour of the potential vorticity evaluated at 690 mbar for the case $s = 0$, $\lambda_1^2 = 1.0$ and $U_0 = 0.5$. This contour of the potential vorticity has a radius of 0.93 in the initial condition. The aspect ratio is defined as the ratio of the major and minor axes of an ellipse with the same second order moments as the selected contour, while the orientation is defined as the angle between the major axis of the moment ellipse and the x axis with a positive value indicating a clockwise rotation (in the direction of the rotation of the vortex). The oscillations in aspect ratio and orientation differ in phase by approximately 90 degrees, such that the aspect ratio is increasing while the orientation is negative and the decreasing while the orientation is positive.

These oscillations in shape and orientation are accompanied by conversions of

Figure 2.10a. Example of a vortex rotating counter to the mean zonal flow. Time evolution of the streamfunction at 690 mbar of an f -plane vortex with $s = 0.0$, $\lambda_1^2 = 1.0$ and $U_0 = 1.0$ at times 0.0, 2.97, 5.94 and 8.91. The contour interval is 0.25 and negative contours are dashed. Contours for $\psi < -2.0$ are not shown.

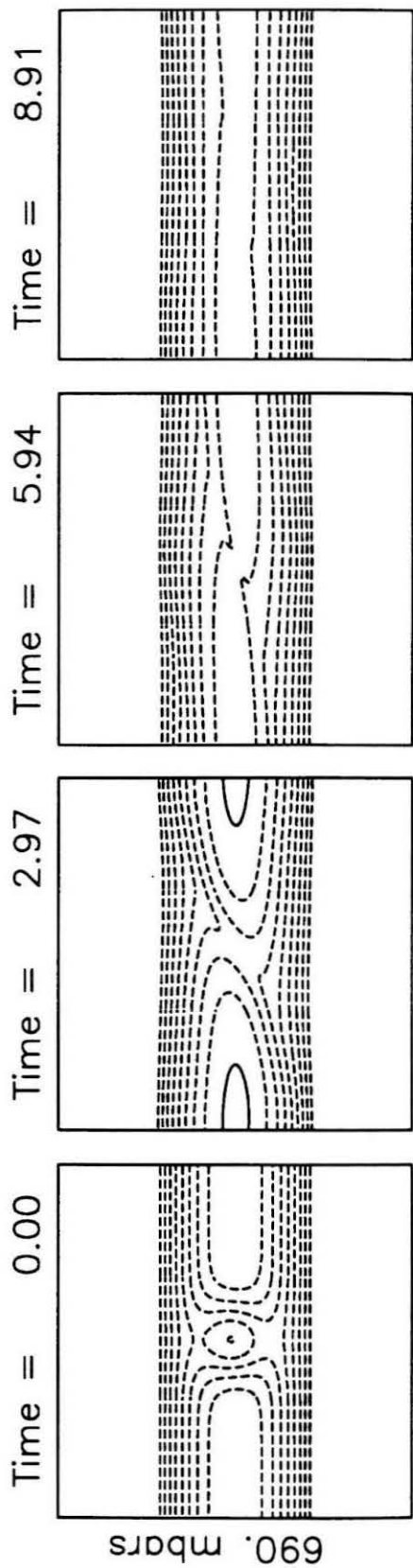


Figure 2.10b. Example of a vortex rotating counter to the mean zonal flow. Time evolution of the potential vorticity at 690 mbar of an f -plane vortex with $s = 0.0$, $\lambda_1^2 = 1.0$ and $U_0 = 1.0$ at times 0.0, 2.97, 5.94 and 8.91. The contour interval is 1.0 and negative contours are dashed.

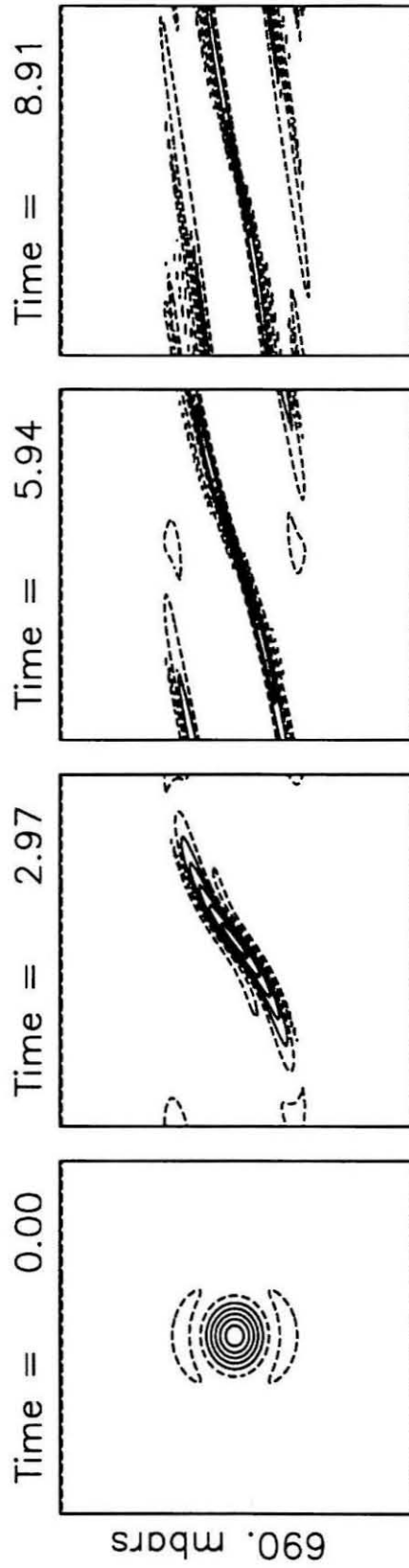


Figure 2.11a. Example of a vortex rotating counter to the mean zonal flow at some altitudes. Time evolution of the streamfunction of an f -plane vortex with $s = -2.0$, $\lambda_1^2 = 0.03$ and $U_0 = 0.5$ at times 0.0, 4.45, 8.91 and 13.36. The left column shows the streamfunction evaluated at 690 mbar, and the right column shows the streamfunction evaluated at 3962 mbar. The contour interval is 0.25 and negative contours are dashed. Contours for $\psi < -2.0$ are not shown.

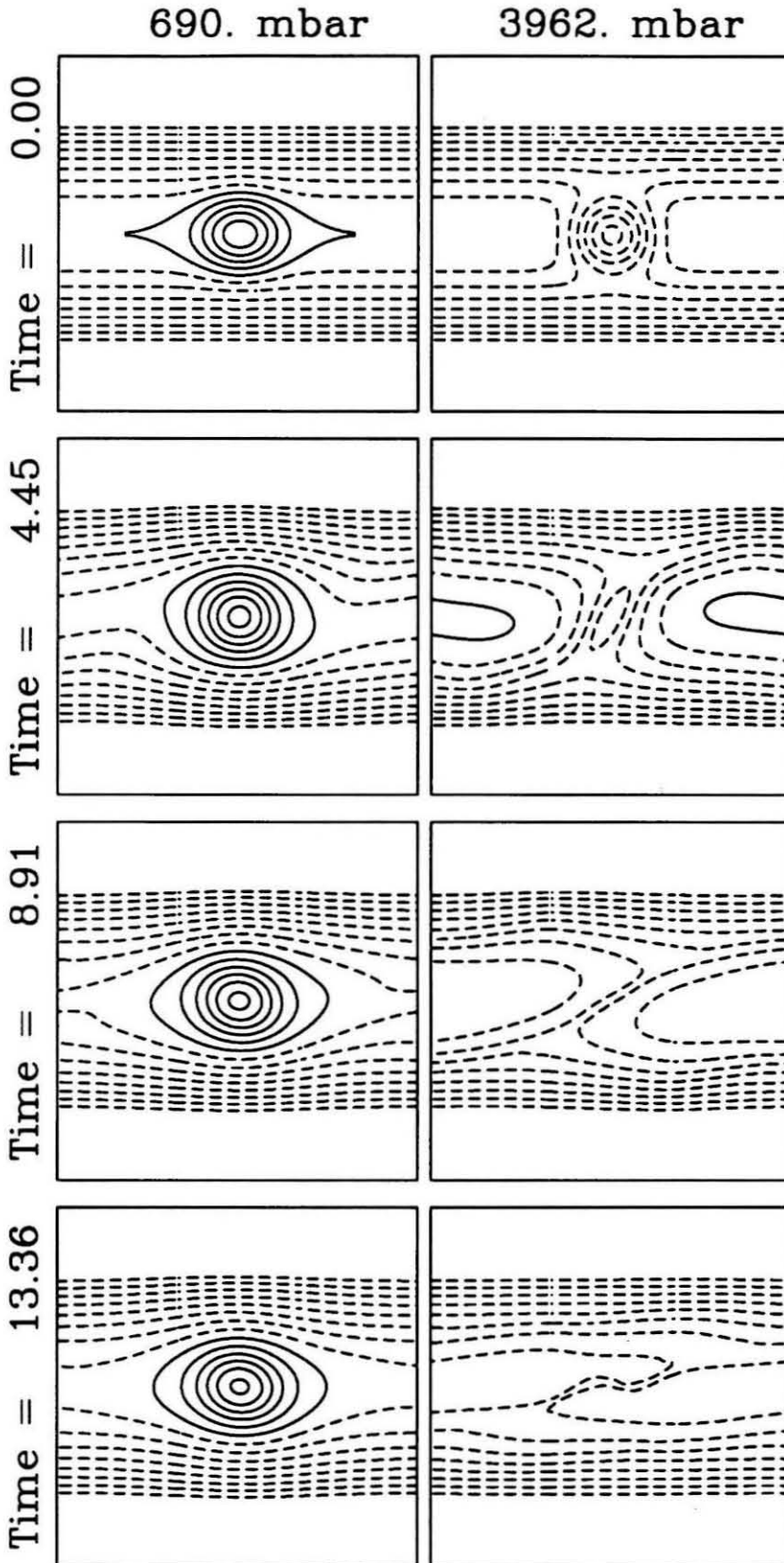


Figure 2.11b. Example of a vortex rotating counter to the mean zonal flow at some altitudes. Time evolution of the potential vorticity of an f -plane vortex with $s = -2.0$, $\lambda_1^2 = 0.03$ and $U_0 = 0.5$ at times 0.0, 4.45, 8.91 and 13.36. The left column shows the potential vorticity evaluated at 690 mbar, and the right column shows the potential vorticity evaluated at 3962 mbar. The contour interval is 2.0, negative contours are dashed, and the contours straddle 0.

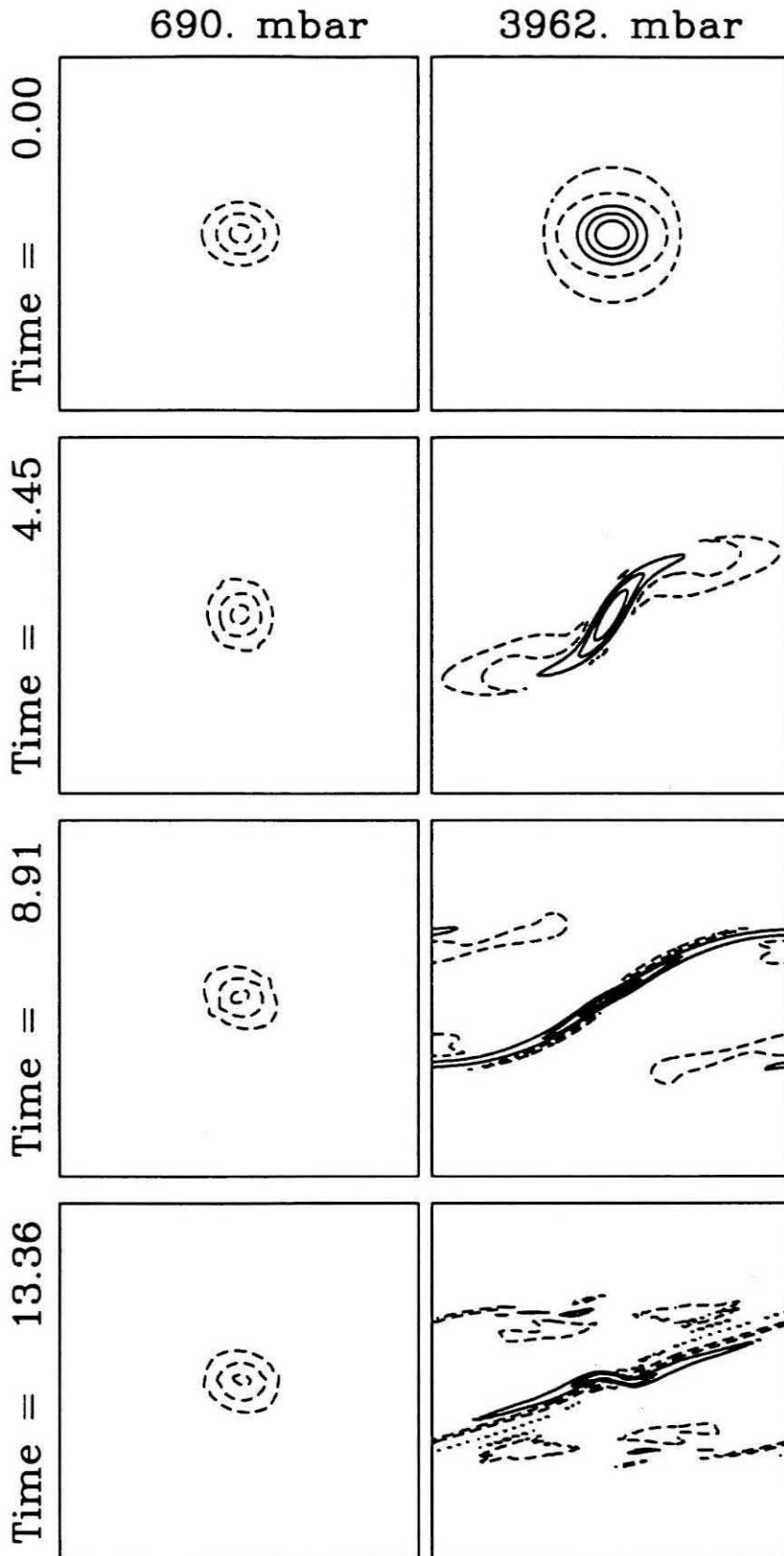


Figure 2.12. Shape and orientation oscillations of a stable vortex in a mean zonal shear. Aspect ratio and orientation of the $q = -1.3$ potential vorticity contour at 690 mbar for $s = 0$, $\lambda_1^2 = 1.0$ and $U_0 = 0.5$. The upper panel shows the aspect ratio as a function of time and the lower panel shows the orientation as a function of time.

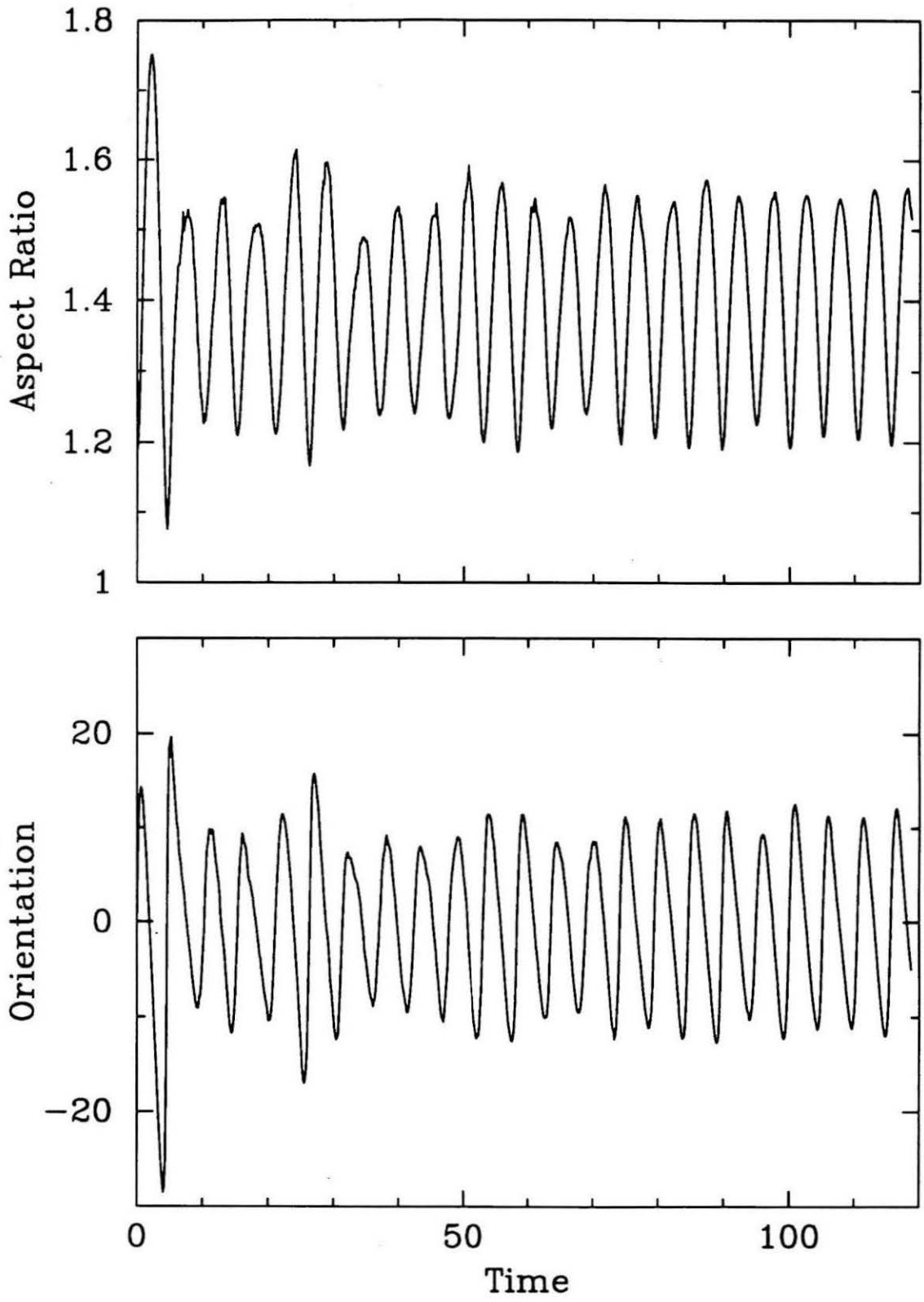
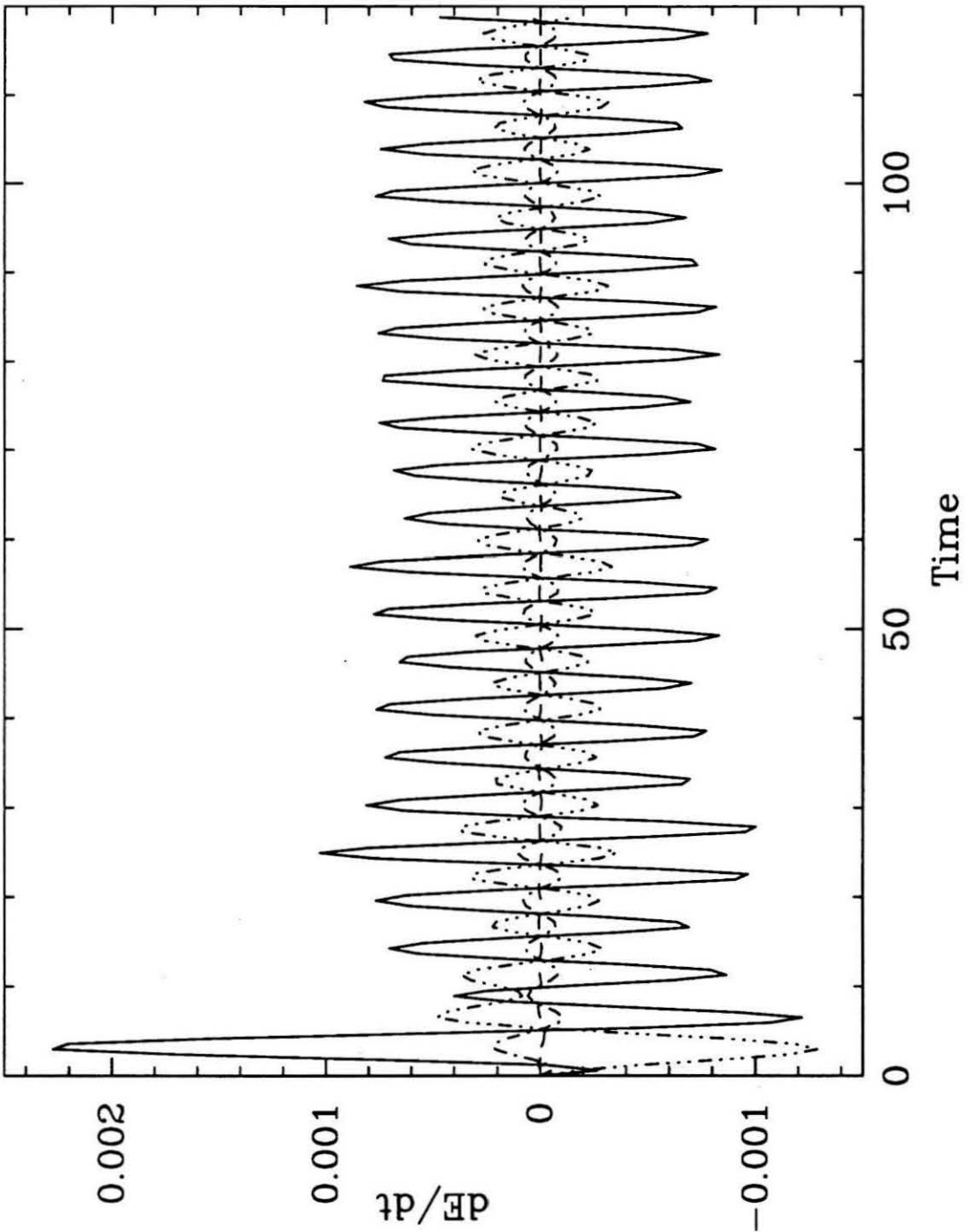


Figure 2.13. Time variation of the energy conversion terms for a stable vortex in a mean zonal shear with $s = 0$, $\lambda_1^2 = 1.0$ and $U_0 = 0.5$. The solid line is $\{\bar{K} \cdot K'\}$, the conversion of mean kinetic energy to eddy kinetic energy. The dashed line is $\{\bar{P} \cdot P'\}$, the conversion of mean potential energy to eddy potential energy. The dot-dashed line is $\{\bar{P} \cdot \bar{K}\}$, the conversion of mean potential energy to mean kinetic energy, and the dot-dot-dot-dashed line is $\{P' \cdot K'\}$, the conversion of eddy potential energy to eddy kinetic energy.



energy between the vortex and the mean zonal flow which also show quasi-periodic oscillations. The energy conversion terms are shown in Fig. 2.13. A derivation for the energy conversion terms in a normal-mode model is outlined in Appendix A. The main energy conversion term is $\{\bar{K} \cdot K'\}$, the conversion of mean kinetic energy to eddy kinetic energy. These oscillations of $\{\bar{K} \cdot K'\}$ are approximately 90 degrees out of phase with the oscillations of aspect ratio, and roughly in phase with the oscillations of orientation, such that $\{\bar{K} \cdot K'\}$ is positive (the mean flow is adding energy to the vortex) while the aspect ratio of the vortex is decreasing and the vortex is tilted clockwise from alignment of the major axis with the flow. There is also a weaker contribution from $\{P' \cdot K'\}$, the conversion of eddy potential energy to eddy kinetic energy, which oscillates 180 degrees out of phase from $\{\bar{K} \cdot K'\}$. The oscillations persist throughout the computation, with no sign of decaying.

2.4.2 Effect of shear on horizontal fragmentation

The effect of horizontal shear on horizontal fragmentation by baroclinic instability is shown in Fig. 2.14 for the case $s = -2.0$, $\lambda_1^2 = 1.0$ and $U_0 = 0.5$. This is the same case as shown in Fig. 2.2, except for the addition of the mean zonal flow. The initial behavior of the vortex is similar to the behavior in the absence of the zonal flow: the vortices become elongated with the upper and lower vortices tilted with respect to each other. In contrast to the case without the zonal flow, however, the upper layer vortex (which has the same sign of vorticity as the zonal flow) does not split into two vortices, but instead sheds two large filaments of potential vorticity, with weak vortices at the ends, which become drawn out by the mean zonal flow. The lower layer vortex again splits into two vortices. The end result is that the original vortex is strongly modified, becoming smaller and having a stable vertical structure, but is not completely destroyed. The energy conversions for this case are shown in Fig. 2.15. The dominant term is the conversion of eddy potential energy

into eddy kinetic energy, which indicates that the instability is baroclinic. There are also significant contributions from the interactions with the mean flow during the time when the main vortex is adjusting to its final state. The timescale for this adjustment and shedding of vortices is on the order of the turnaround time for the vortex, but slightly faster than the timescale for splitting of the vortex in the absence of the zonal flow.

2.4.3 Effect of shear on tripole formation

The effect of horizontal shear on tripole formation is shown in Fig. 2.16 for the case $s = -0.5$, $\lambda_1^2 = 1.0$ and $U_0 = 0.5$, which is the same as shown in Fig. 2.4 except for the addition of the mean zonal flow. In the upper layer the streamfunction contours become slightly elongated and then return to a more circular form, while in the lower layer a vortex spins up beneath the upper layer vortex. The behavior is similar to the behavior without the vertical shear, except that the formation of the flanking vortices is inhibited by the zonal flow. The lower layer potential vorticity patches, which would become the flanking vortices in the absence of the mean zonal flow, are instead sheared out by the zonal flow. The original vortex maintains its identity, but the vertical structure adjusts to give a stable vortex. The energy conversion terms are shown in Fig. 2.17, and are dominated by quasi-periodic oscillations of $\{\bar{K} \cdot K'\}$. The $\{P' \cdot K'\}$ term is also significant, oscillating out of phase with $\{\bar{K} \cdot K'\}$ as in the case of a steady vortex, but with a bias towards converting potential energy into kinetic energy while the vortex is adjusting to its final state. The timescale for this adjustment is similar to the timescale for tripole formation in the absence of the mean zonal flow.

2.4.4 Effect of shear on vertical fragmentation

In the case of vertical fragmentation by internal barotropic instability, the presence of a mean zonal flow greatly decreases the rate at which the upper and lower vor-

Figure 2.14a. Effect of mean zonal shear on horizontal fragmentation Time evolution of the streamfunction of an f -plane vortex with $s = -2.0$, $\lambda_1^2 = 1.0$ and $U_0 = 0.5$ at times 0.0, 2.23, 4.45 and 6.68. The left column shows the streamfunction evaluated at 690 mbar, and the right column shows the streamfunction evaluated at 3962 mbar. The contour interval is 0.25 and negative contours are dashed. Contours for $\psi < -2.0$ are not shown.

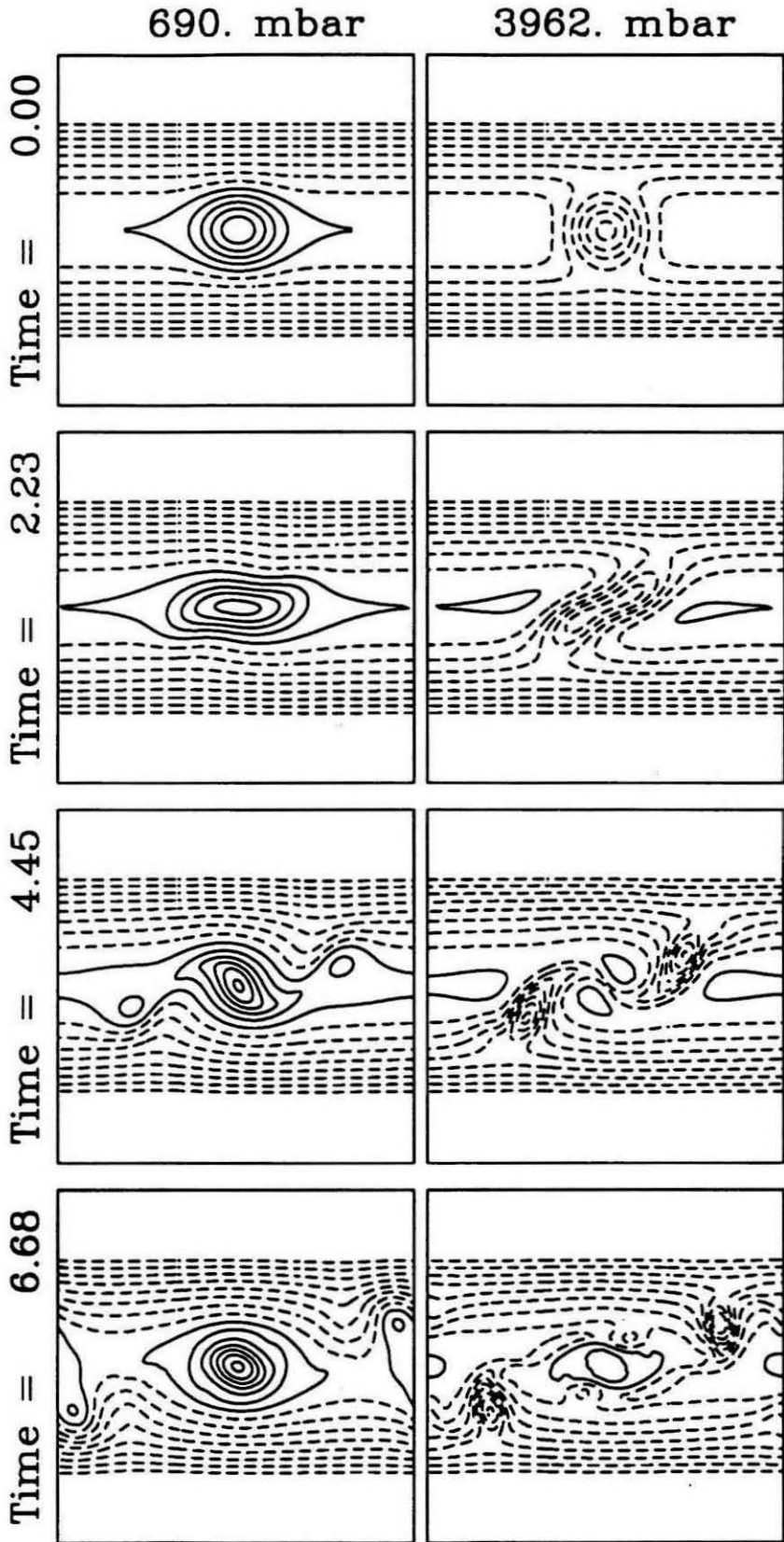


Figure 2.14b. Effect of mean zonal shear on horizontal fragmentation. Time evolution of the potential vorticity of an f -plane vortex with $s = -2.0$, $\lambda_1^2 = 1.0$ and $U_0 = 0.5$ at times 0.0, 2.23, 4.45 and 6.68. The left column shows the potential vorticity evaluated at 690 mbar, with a contour interval of 5.0. The right column shows the potential vorticity evaluated at 3962 mbar, with a contour interval of 10.0. Negative contours are dashed, and the contours straddle 0.

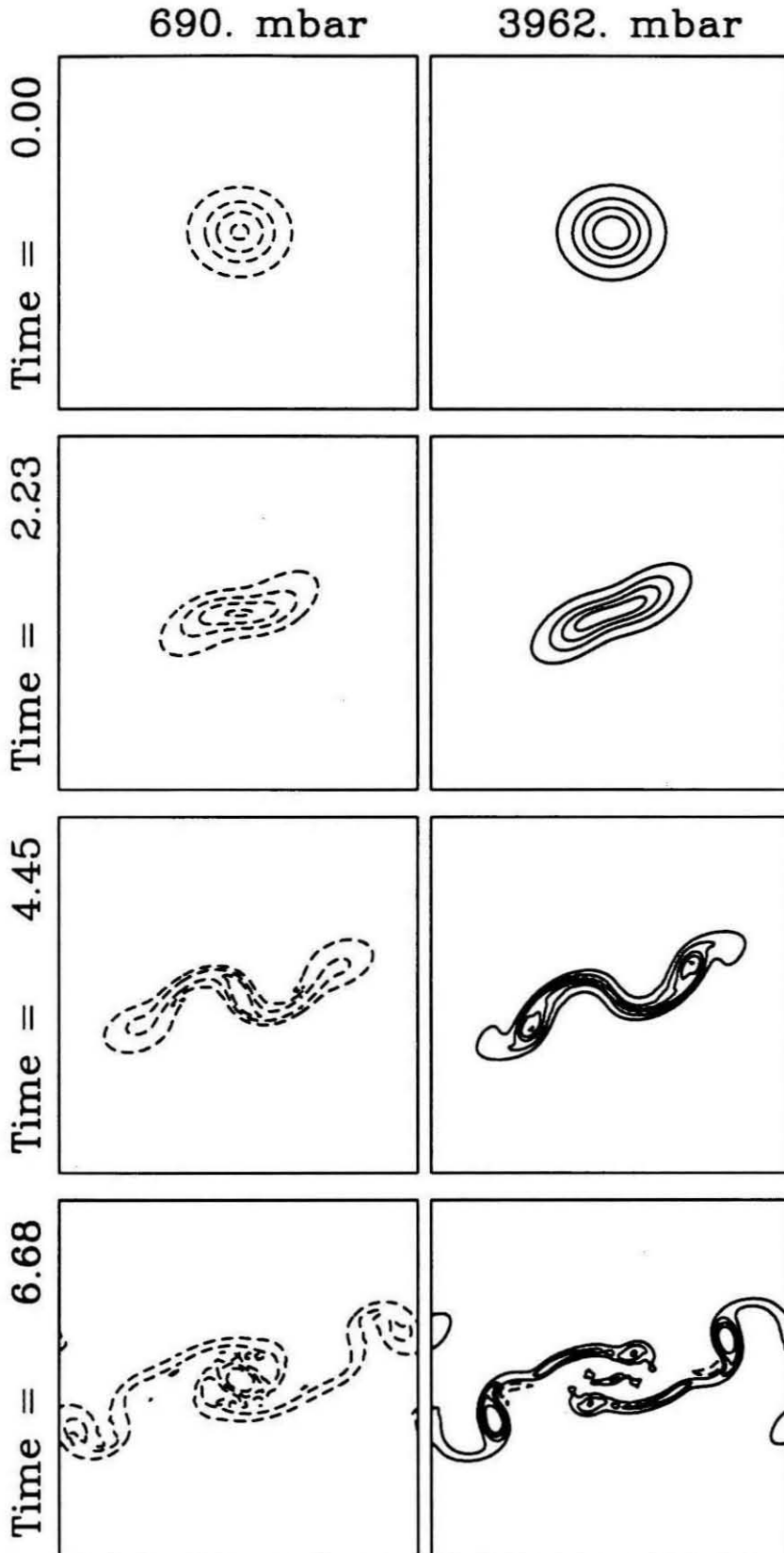


Figure 2.15. Time variation of the energy conversion terms for the case shown in Fig. 2.14. The solid line is $\{\bar{K} \cdot K'\}$, the conversion of mean kinetic energy to eddy kinetic energy. The dashed line is $\{\bar{P} \cdot P'\}$, the conversion of mean potential energy to eddy potential energy. The dot-dashed line is $\{\bar{P} \cdot \bar{K}\}$, the conversion of mean potential energy to mean kinetic energy, and the dot-dot-dashed line is $\{P' \cdot K'\}$, the conversion of eddy potential energy to eddy kinetic energy.

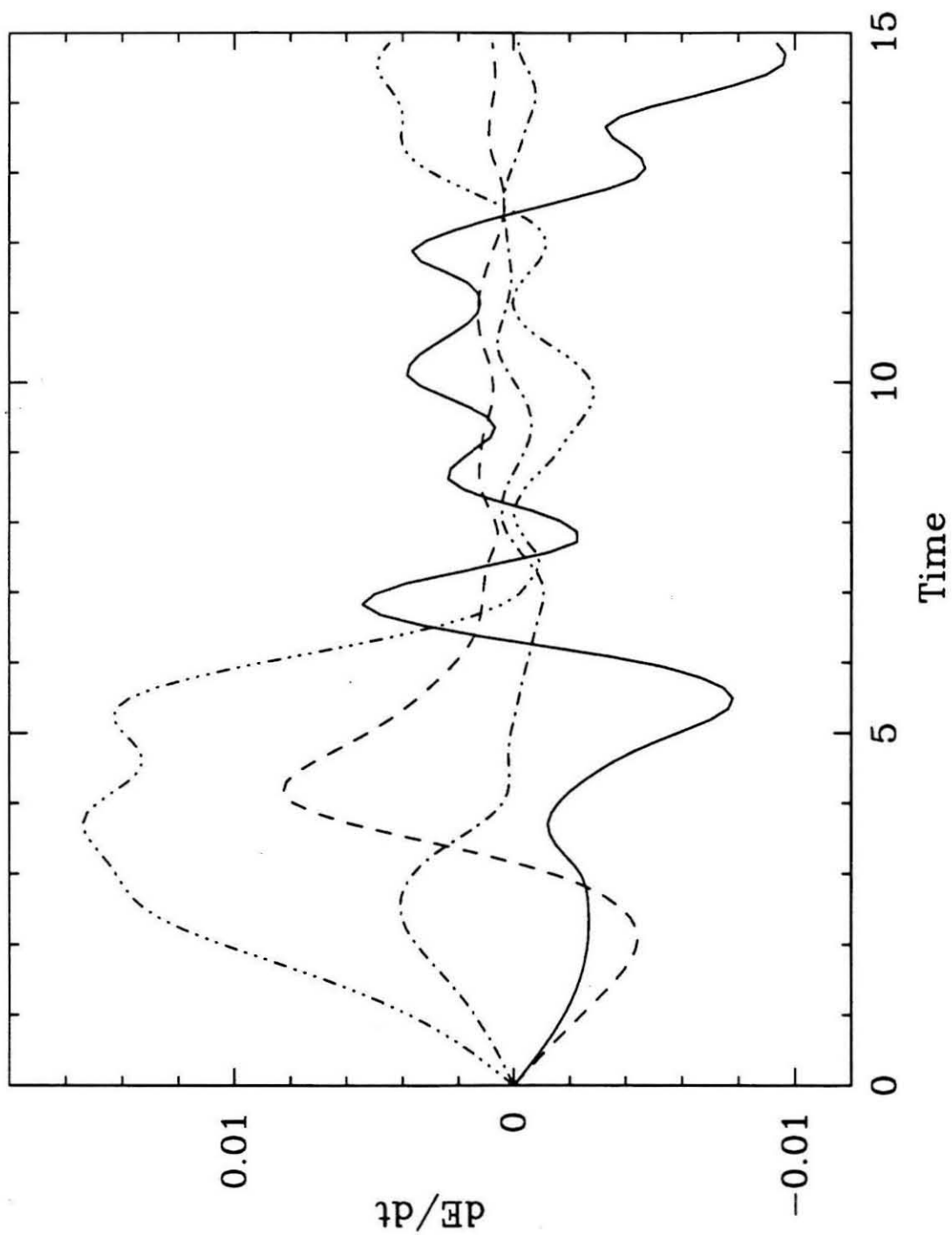


Figure 2.16a. Effect of mean zonal shear on tripole formation. Time evolution of the streamfunction of an f -plane vortex with $s = -0.5$, $\lambda_1^2 = 1.0$ and $U_0 = 0.5$ at times 0.0, 4.16, 8.31 and 12.47. The left column shows the streamfunction evaluated at 690 mbar, and the right column shows the streamfunction evaluated at 3962 mbar. The contour interval is 0.25 and negative contours are dashed. Contours for $\psi < -2.0$ are not shown.

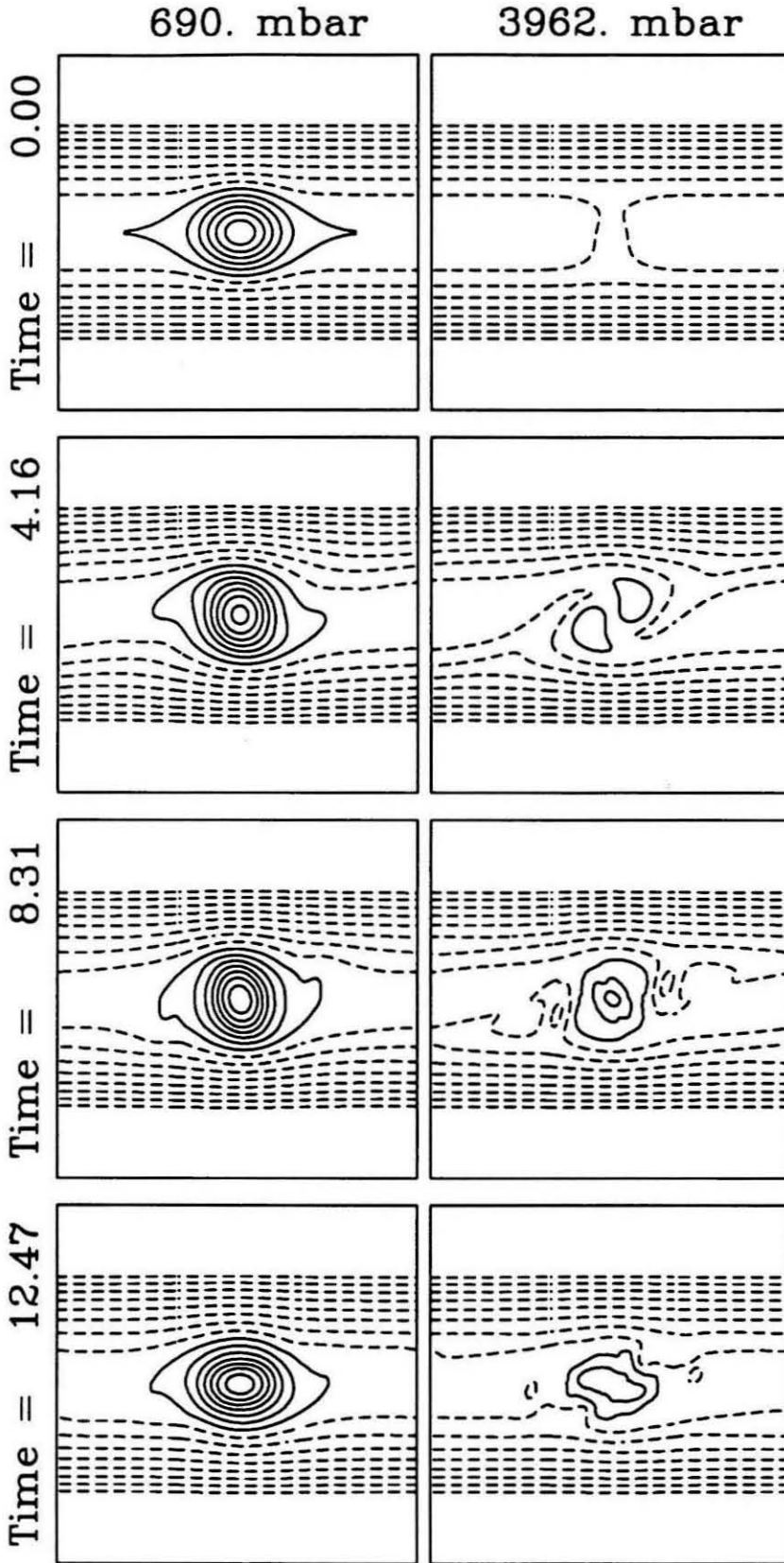


Figure 2.16b. Effect of mean zonal shear on tripole formation. Time evolution of the potential vorticity of an f -plane vortex with $s = -0.5$, $\lambda_1^2 = 1.0$ and $U_0 = 0.5$ at times 0.0, 4.16, 8.31 and 12.47. The left column shows the potential vorticity evaluated at 690 mbar, and the right column shows the potential vorticity evaluated at 3962 mbar. The contour interval is 5.0, and negative contours are dashed. and the contours straddle 0.

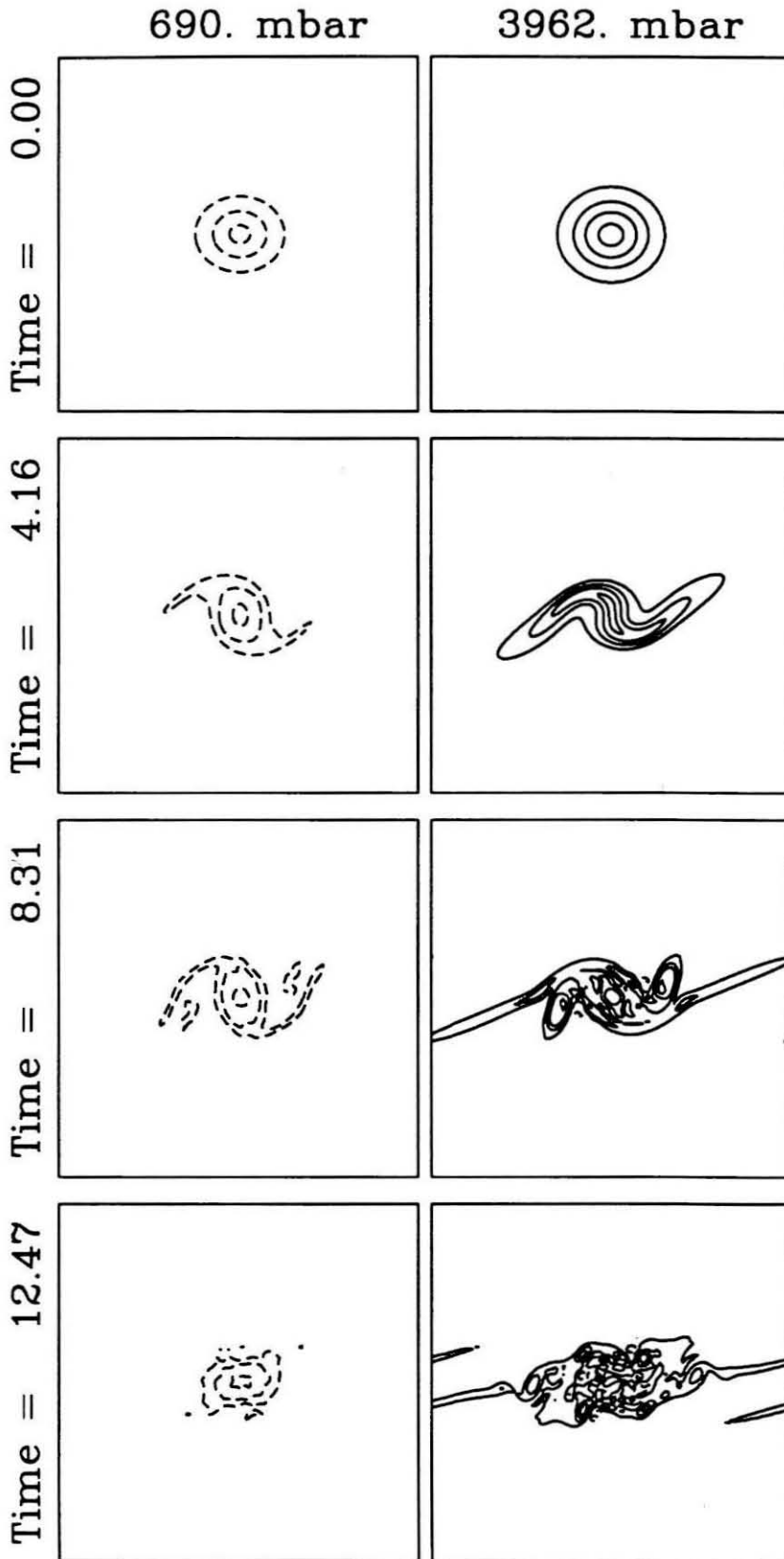
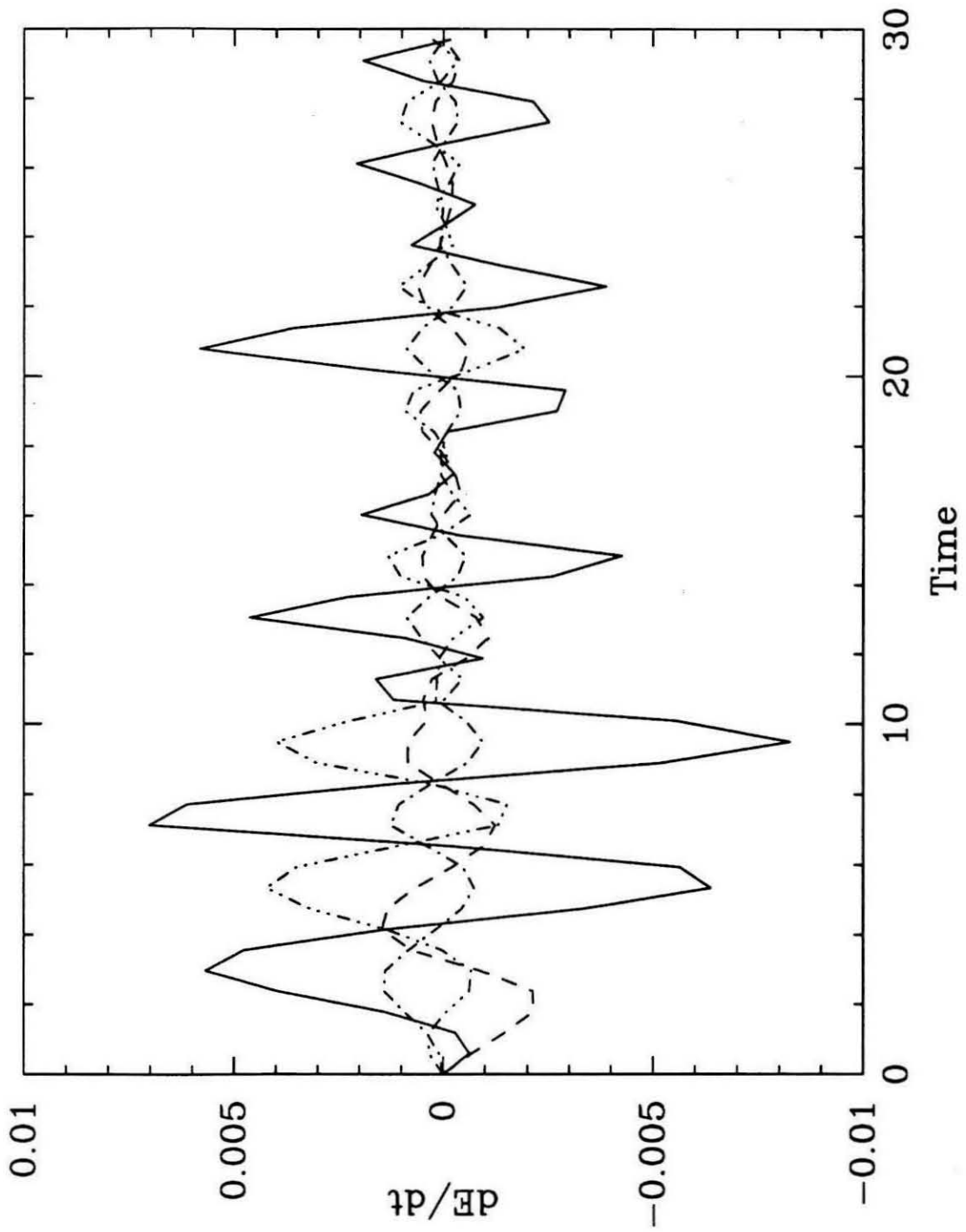


Figure 2.17. Time variation of the energy conversion terms for the case shown in Fig. 2.16. The solid line is $\{\bar{K} \cdot K'\}$, the conversion of mean kinetic energy to eddy kinetic energy. The dashed line is $\{\bar{P} \cdot P'\}$, the conversion of mean potential energy to eddy potential energy. The dot-dashed line is $\{\bar{P} \cdot \bar{K}\}$, the conversion of mean potential energy to mean kinetic energy, and the dot-dot-dot-dashed line is $\{P' \cdot K'\}$, the conversion of eddy potential energy to eddy kinetic energy.



tices separate from each other. As a result, the upper and lower vortices follow an ellipsoidal spiral trajectory which slowly expands until the separation between the vortices becomes sufficiently large. Figure 2.18 shows the trajectories of the maxima of the upper and lower layer streamfunctions for the case $s = 0.5$, $\lambda_1^2 = 0.03$ and $U_0 = 0.5$. The spiral trajectory is associated with an oscillation of the latitude and longitude of the vortex, with a 90 degree difference in phase between the latitudinal and longitudinal oscillations. The longitude oscillations have a larger amplitude than the latitude oscillation, and the weaker of the upper and lower layer sections of the vortex shows a larger oscillation amplitude than the stronger section. Both the amplitude and period of the oscillations increase with time, and when the peak-to-peak amplitude of the latitude oscillations reaches approximately the radius of the vortex, the upper and lower sections of the vortex separate completely and are advected away from each other by the mean flow (although variations of latitude and longitude still occur when the periodic boundary conditions result in the upper and lower vortices encountering each other). Increasing the value of λ_1^2 (decreasing the radius of deformation or increasing the size of the vortex), decreases the rate at which the amplitude and period of the oscillations grow, Increasing U_0 has a similar effect. This can be seen in Fig. 2.19, which shows the latitude and longitude of the vortex streamfunction maxima for the cases ($\lambda_1^2 = 0.1$, $U_0 = 0.5$) and ($\lambda_1^2 = 0.3$, $U_0 = 0.75$), both with $s = 0.5$.

2.4.5 Discussion

The nonlinear behavior of nearly circular, two-mode, Gaussian vortices on an f -plane in a barotropic mean zonal shear can be broken down into five classifications: adjustment to a more barotropic structure with shedding of smaller vortices, adjustment to a more barotropic structure without shedding of smaller vortices, vertical fragmentation of the vortex preceded by oscillations in the position of the vortex, shearing

of the vortex by the zonal flow, and stability. Figure 2.20 shows the regions of λ_1^2 - s parameter space over which each of these types of behavior occurs for $U_0 = 0.5$ and $U_0 = 1.0$. A list of the runs used to generate these figures is shown in Table 2.3.

Adjustment to a more barotropic structure with shedding of smaller vortices occurs in roughly the same region of λ_1^2 - s parameter space as horizontal fragmentation does in the absence of the mean zonal shear, while adjustment to a more barotropic structure without shedding of smaller vortices occurs in roughly the same region of λ_1^2 - s parameter space as tripole formation does in the absence of the mean zonal shear. All of these behaviors occur only for vortices with diameters roughly larger than the first internal radius of deformation and with potential vorticity of opposite sign in the upper and lower layers. In all the cases examined, the initial vortex is not completely destroyed, although its vertical structure is modified.

Oscillations in the latitude and longitude of the vortex, usually followed by a breakup into separate upper and lower layer vortices, occur only for vortices with diameters smaller than the first internal radius of deformation and with the same sign of vorticity at all altitudes. This is an example of internal barotropic instability, modified by the presence of the mean zonal flow, which reduces the rate at which the upper and lower layer vortices separate, allowing the upper and lower layer vortices to remain close enough together for their mutual advection to produce the oscillations in position. The amplitude and period of the oscillations grow as the upper and lower layer vortices move farther apart. When the separation becomes large enough, approximately greater than the radius of the vortex in latitude, the oscillations cease and the zonal flow advects the vortices away from each other. We have also found one example (Fig 2.19a) in which the amplitude of the oscillations stops growing before the upper and lower vortices separate. It is interesting to note that these positional oscillations occur for vortices with $s = 0$, which can be represented by an equivalent

Figure 2.18a. Effect of mean zonal shear on vertical fragmentation. Trajectories of the upper and lower layer components of the vortex for $s = 0.5$, $\lambda_1^2 = 0.03$ and $U_0 = 0.5$. The position of the vortex is defined as the location of the maxima in the perturbation streamfunction $\psi - \psi_0$, evaluated at pressures of 690 mbar (solid line) and 4000 mbar (dotted line).

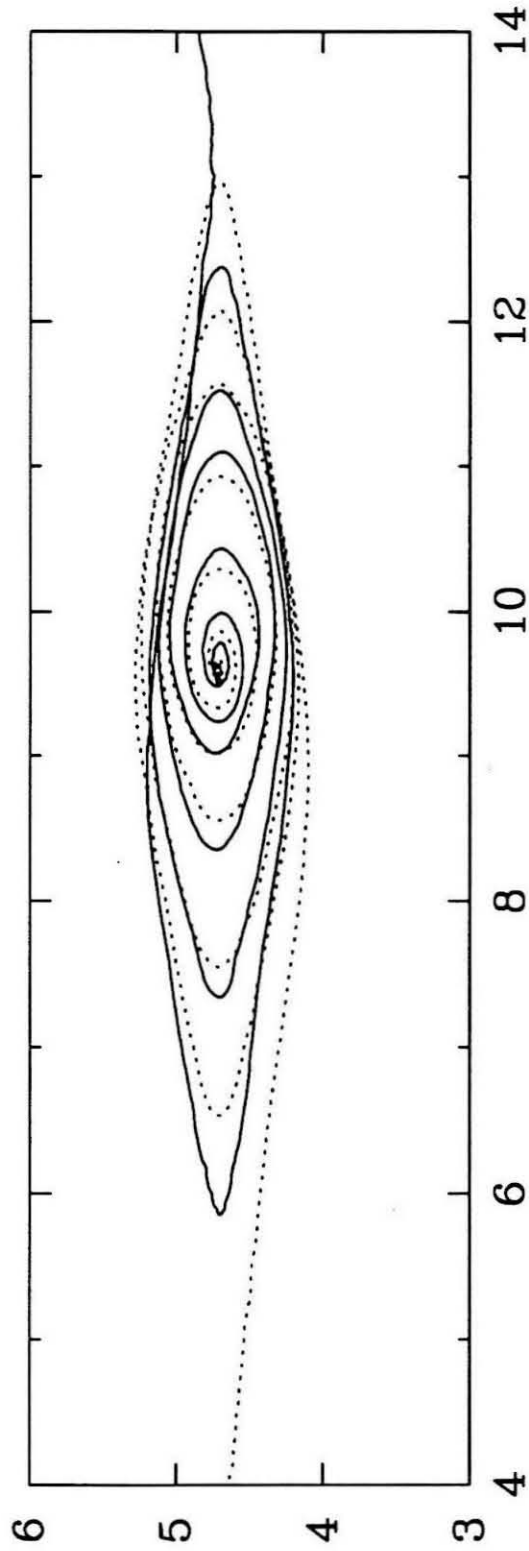


Figure 2.18b. Effect of mean zonal flow on vertical fragmentation. Latitude and longitude of the vortex for $s = 0.5$, $\lambda_1^2 = 0.03$ and $U_0 = 0.5$, evaluated at 690 mbar (solid line) and 3962 mbar (dotted line). The upper panel shows the longitude as a function of time, and the lower panel shows the latitude as a function of time.

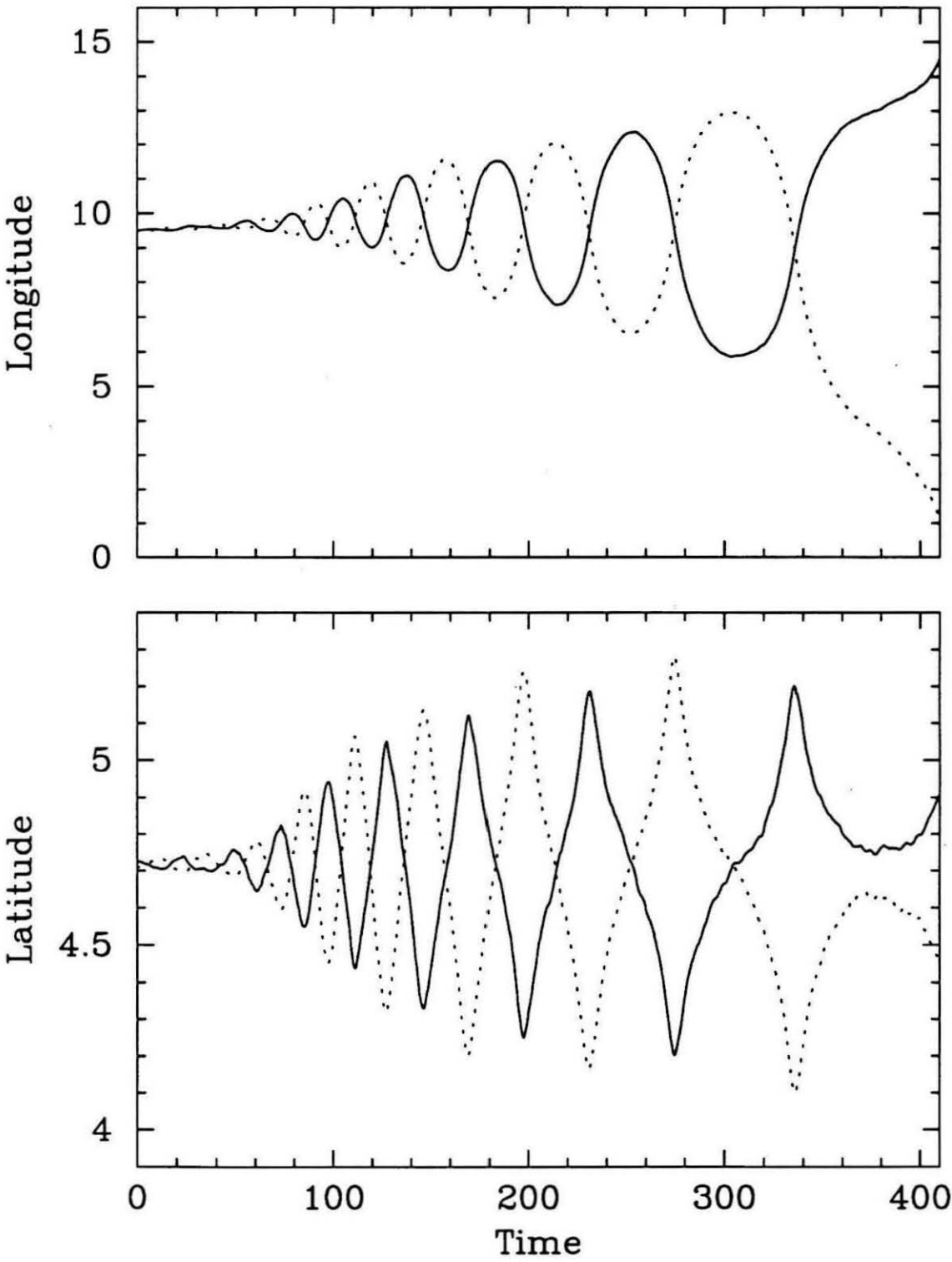


Figure 2.19a. Example of positional oscillations of a vortex. As Fig. 2.18b, but for $s = 0.5$, $\lambda_1^2 = 0.1$ and $U_0 = 0.5$.

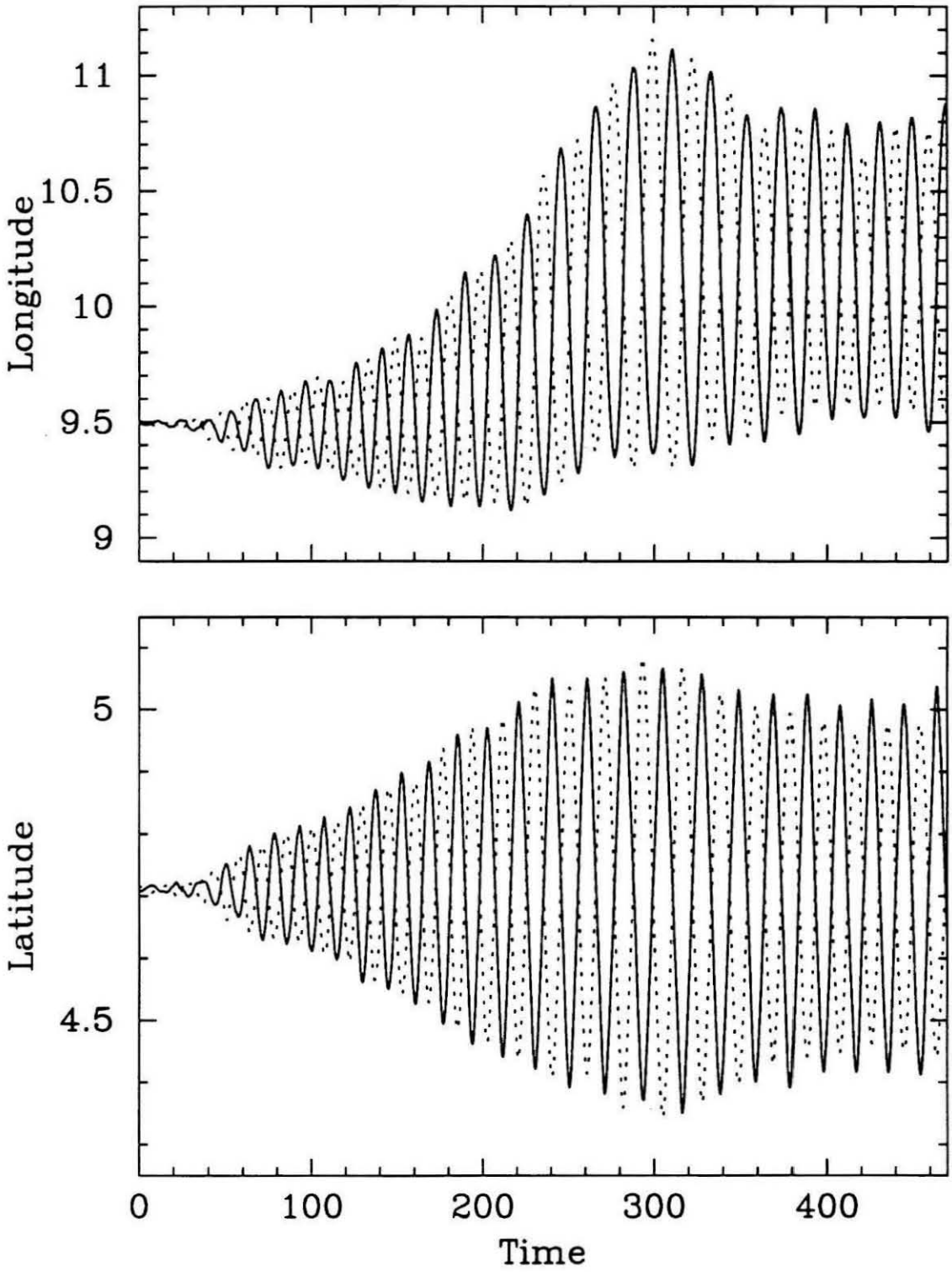


Figure 2.19b. Example of positional oscillations of a vortex. As Fig. 2.18b, but for $s = 0.5$, $\lambda_1^2 = 0.03$ and $U_0 = 0.75$.

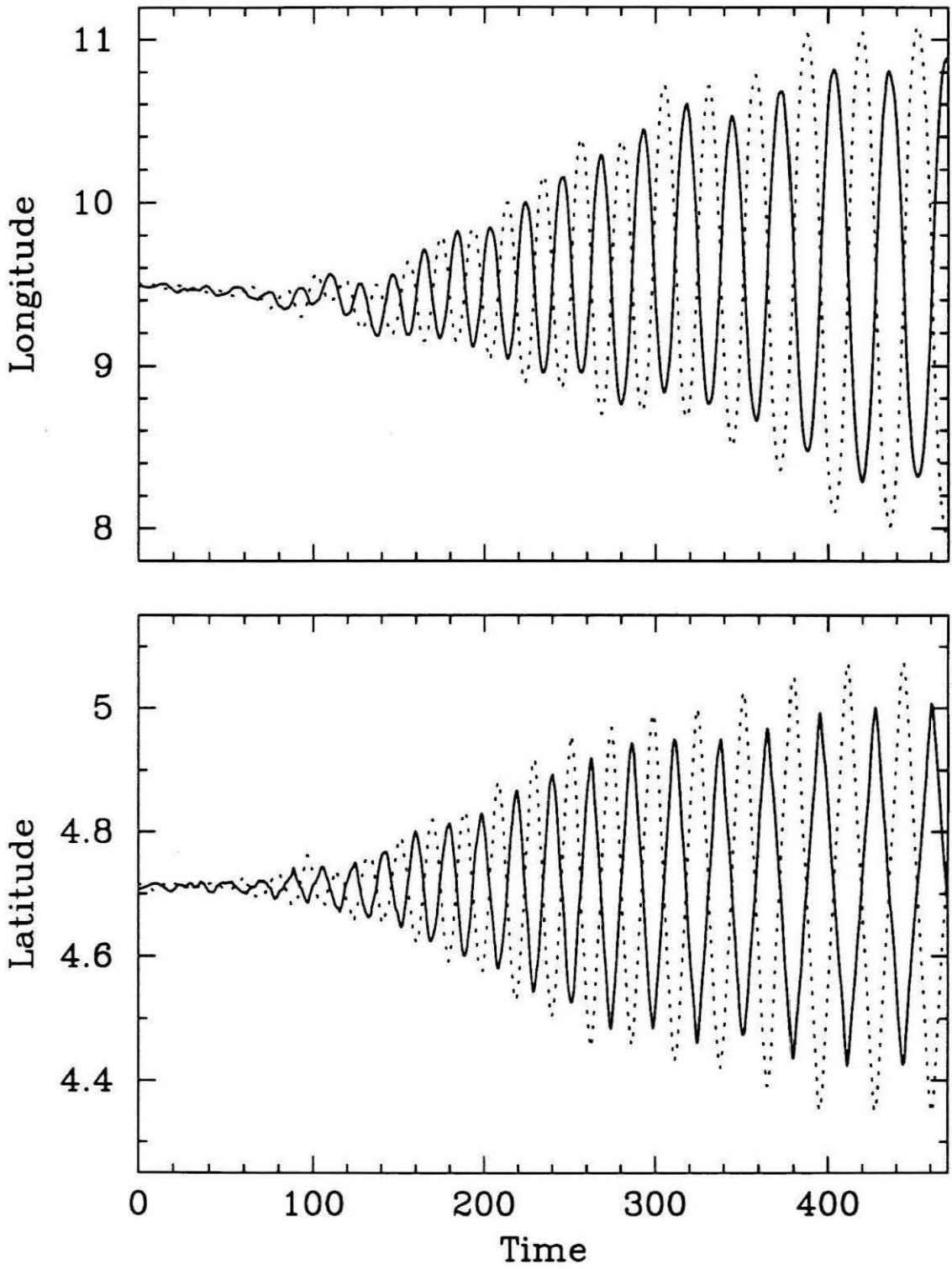


Figure 2.20a. Regime diagram for the behavior of vortices on an f -plane with mean zonal flow $U_0 = 0.5$. The horizontal axis is s , the ratio of the second baroclinic mode to the first baroclinic mode in the initial vortex. The vertical axis is the radius of the vortex relative to the first internal radius of deformation. The open squares (\square) are stable vortices, the plus signs (+) are vortices which adjust to stability while ejecting smaller vortices, the crosses (\times) are vortices which adjust to a stable state with a different vertical structure from the initial condition without ejecting smaller vortices, the asterisks (*) are vortices which are sheared out at the altitudes at which they rotate counter to the mean flow, and the open triangles (\triangle) are vortices which develop oscillations in longitude and latitude.

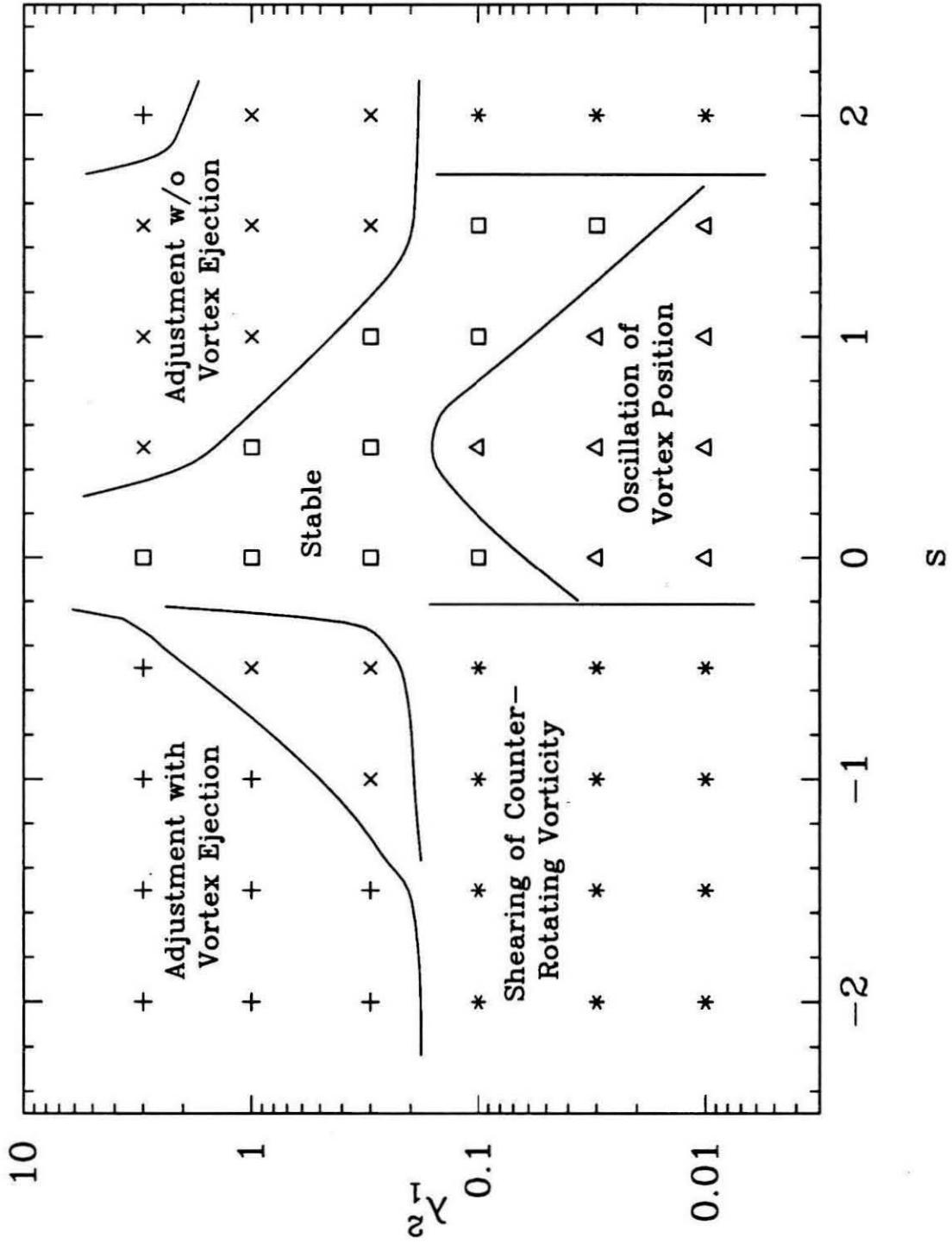


Figure 2.20b. As Fig. 2.20a, but with $U_0 = 1.0$.

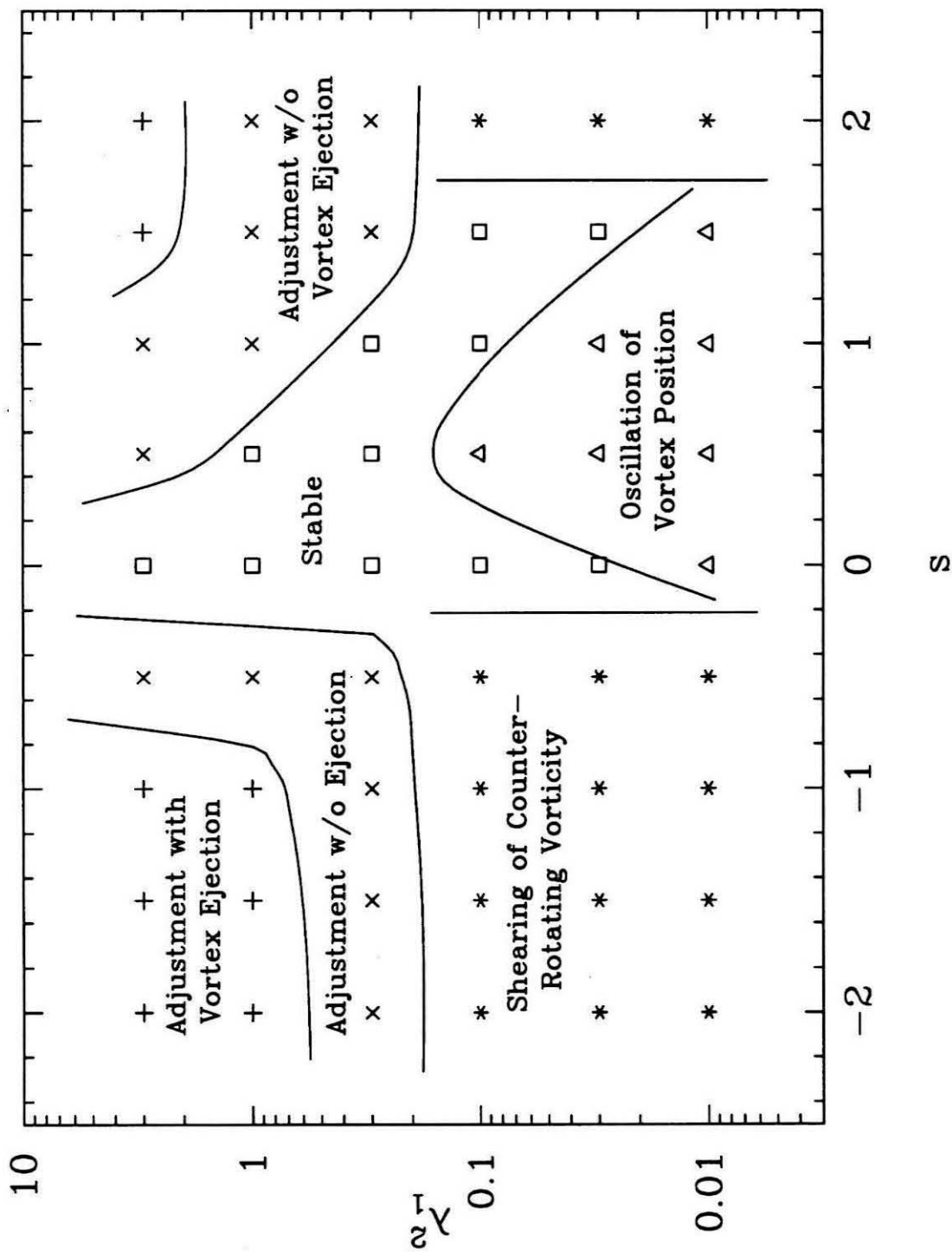


Table 2.3. Simulations of f -plane Vortices with Mean Zonal Flow

λ_1^2	s	U_0	N_x	N_y	$\Delta t/\Delta x$	length of run
3.0	-2.0	0.5	128	128	0.2	59.37
3.0	-2.0	1.0	128	128	0.2	59.37
3.0	-1.5	0.5	128	128	0.2	59.37
3.0	-1.5	1.0	128	128	0.2	59.37
3.0	-1.0	0.5	128	128	0.2	59.37
3.0	-1.0	1.0	128	128	0.2	59.37
3.0	-0.5	0.5	128	128	0.2	59.37
3.0	-0.5	1.0	128	128	0.2	59.37
3.0	0.0	0.5	128	128	0.2	478.72
3.0	0.0	0.5	256	128	0.2	478.72
3.0	0.0	1.0	128	128	0.2	59.37
3.0	0.5	0.5	128	128	0.2	59.37
3.0	0.5	1.0	128	128	0.2	59.37
3.0	1.0	0.5	128	128	0.2	59.37
3.0	1.0	1.0	128	128	0.2	59.37
3.0	1.5	0.5	128	128	0.2	59.37
3.0	1.5	1.0	128	128	0.2	59.37
3.0	2.0	0.5	128	128	0.2	59.37
3.0	2.0	1.0	128	128	0.2	59.37
1.0	-2.0	0.5	128	128	0.2	59.37
1.0	-2.0	1.0	128	128	0.2	59.37
1.0	-1.5	0.5	128	128	0.2	59.37
1.0	-1.5	1.0	128	128	0.2	59.37
1.0	-1.0	0.5	128	128	0.2	59.37
1.0	-1.0	1.0	128	128	0.2	59.37
1.0	-0.5	0.5	128	128	0.2	59.37
1.0	-0.5	1.0	128	128	0.2	59.37
1.0	0.0	0.5	128	128	0.2	478.72
1.0	0.0	0.5	256	128	0.2	478.72
1.0	0.0	1.0	128	128	0.2	478.72
1.0	0.5	0.5	128	128	0.2	59.37
1.0	0.5	1.0	128	128	0.2	59.37
1.0	1.0	0.5	128	128	0.2	59.37
1.0	1.0	1.0	128	128	0.2	59.37
1.0	1.5	0.5	128	128	0.2	59.37
1.0	1.5	1.0	128	128	0.2	59.37
1.0	2.0	0.5	128	128	0.2	59.37
1.0	2.0	1.0	128	128	0.2	59.37
0.3	-2.0	0.5	128	128	0.2	59.37
0.3	-2.0	1.0	128	128	0.2	59.37
0.3	-1.5	0.5	128	128	0.2	59.37
0.3	-1.5	1.0	128	128	0.2	59.37
0.3	-1.0	0.5	128	128	0.2	59.37
0.3	-1.0	1.0	128	128	0.2	59.37
0.3	-0.5	0.5	128	128	0.2	59.37

Table 2.3. (continued)

λ_1^2	s	U_0	N_x	N_y	$\Delta t/\Delta x$	length of run
0.3	-0.5	1.0	128	128	0.2	59.37
0.3	0.0	0.5	128	128	0.2	478.72
0.3	0.0	0.5	256	128	0.2	478.72
0.3	0.0	1.0	128	128	0.2	59.37
0.3	0.5	0.5	128	128	0.2	478.72
0.3	0.5	1.0	128	128	0.2	478.72
0.3	1.0	0.5	128	128	0.2	478.72
0.3	1.0	1.0	128	128	0.2	478.72
0.3	1.5	0.5	128	128	0.2	478.72
0.3	1.5	1.0	128	128	0.2	478.72
0.3	2.0	0.5	128	128	0.2	59.37
0.3	2.0	1.0	128	128	0.2	59.37
0.1	-2.0	0.5	128	128	0.2	59.37
0.1	-2.0	1.0	64	64	0.2	478.72
0.1	-1.5	0.5	128	128	0.2	59.37
0.1	-1.5	1.0	64	64	0.2	478.72
0.1	-1.0	0.5	128	128	0.2	59.37
0.1	-1.0	1.0	64	64	0.2	478.72
0.1	-0.5	0.5	128	128	0.2	59.37
0.1	-0.5	1.0	64	64	0.2	478.72
0.1	0.0	0.5	128	128	0.2	478.72
0.1	0.0	0.5	256	128	0.2	478.72
0.1	0.0	1.0	64	64	0.2	478.72
0.1	0.0	1.0	128	128	0.2	478.72
0.1	0.5	0.5	128	128	0.2	478.72
0.1	0.5	0.5	256	128	0.2	478.72
0.1	0.5	1.0	64	64	0.2	237.48
0.1	0.5	1.0	128	128	0.2	478.72
0.1	1.0	0.5	128	128	0.2	478.72
0.1	1.0	0.5	256	128	0.2	478.72
0.1	1.0	1.0	64	64	0.2	478.72
0.1	1.0	1.0	128	128	0.2	478.72
0.1	1.5	0.5	128	128	0.2	59.37
0.1	1.5	1.0	64	64	0.2	478.72
0.1	2.0	0.5	128	128	0.2	59.37
0.1	2.0	1.0	64	64	0.2	478.72
0.03	-2.0	0.5	128	128	0.2	59.37
0.03	-2.0	1.0	64	64	0.2	478.72
0.03	-1.5	0.5	128	128	0.2	59.37
0.03	-1.5	1.0	64	64	0.2	478.72
0.03	-1.0	0.5	128	128	0.2	59.37
0.03	-1.0	1.0	64	64	0.2	478.72
0.03	-0.5	0.5	128	128	0.2	59.37
0.03	-0.5	1.0	64	64	0.2	478.72
0.03	0.0	0.5	128	128	0.2	478.72

Table 2.3. (continued)

λ_1^2	s	U_0	N_x	N_y	$\Delta t/\Delta x$	length of run
0.03	0.0	0.5	256	128	0.2	478.72
0.03	0.0	1.0	64	64	0.2	478.72
0.03	0.0	1.0	128	128	0.2	478.72
0.03	0.5	0.25	256	128	0.2	478.72
0.03	0.5	0.5	128	128	0.2	478.72
0.03	0.5	0.5	256	128	0.2	478.72
0.03	0.5	0.5	256	64	0.2	478.72
0.03	0.5	0.75	256	128	0.2	478.72
0.03	0.5	1.0	64	64	0.2	478.72
0.03	0.5	1.0	128	128	0.2	478.72
0.03	1.0	0.5	128	128	0.2	478.72
0.03	1.0	0.5	256	128	0.2	478.72
0.03	1.0	1.0	64	64	0.2	478.72
0.03	1.0	1.0	128	128	0.2	478.72
0.03	1.5	0.5	128	128	0.2	478.72
0.03	1.5	0.5	256	128	0.2	478.72
0.03	1.5	1.0	64	64	0.2	478.72
0.03	1.5	1.0	128	128	0.2	478.72
0.03	2.0	0.5	128	128	0.2	59.37
0.03	2.0	1.0	64	64	0.2	478.72
0.01	-2.0	0.5	128	128	0.2	59.37
0.01	-2.0	1.0	64	64	0.2	59.37
0.01	-1.5	0.5	128	128	0.2	59.37
0.01	-1.5	1.0	64	64	0.2	478.72
0.01	-1.0	0.5	128	128	0.2	59.37
0.01	-1.0	1.0	64	64	0.2	478.72
0.01	-0.5	0.5	128	128	0.2	59.37
0.01	-0.5	1.0	64	64	0.2	478.72
0.01	0.0	0.5	128	128	0.2	478.72
0.01	0.0	0.5	256	128	0.2	478.72
0.01	0.0	1.0	64	64	0.2	478.72
0.01	0.0	1.0	128	128	0.2	478.72
0.01	0.5	0.5	128	128	0.2	478.72
0.01	0.5	0.5	256	128	0.2	478.72
0.01	0.5	1.0	64	64	0.2	478.72
0.01	0.5	1.0	128	128	0.2	478.72
0.01	1.0	0.5	256	128	0.2	478.72
0.01	1.0	1.0	64	64	0.2	478.72
0.01	1.0	1.0	128	128	0.2	478.72
0.01	1.5	0.5	128	128	0.2	478.72
0.01	1.5	0.5	256	128	0.2	478.72
0.01	1.5	1.0	64	64	0.2	478.72
0.01	1.5	1.0	128	128	0.2	478.72
0.01	2.0	0.5	128	128	0.2	59.37
0.01	2.0	1.0	64	64	0.2	478.72

barotropic model. The oscillations, however, cannot occur in the equivalent barotropic model, because they require the velocity field to vary with altitude. Vortices which oscillate in longitude have been observed on Jupiter (Peek 1958; Reese and Smith 1966), Saturn (Reese 1971), and Neptune (Hammel *et al.* 1989); comparison of the observations with our model will be discussed in Section 2.6.

Shearing out of the vortex by the mean zonal flow occurs for vortices which are stable in the absence of the shear, and which have the opposite sign of vorticity as the shear flow. If the initial vortex has a different sign of vorticity at different altitudes, only the part of the vortex rotating counter to the flow is sheared out. We also note that the unstable solutions which shed smaller vortices produce small, intense vortices which have a vorticity of opposite sign to the vorticity of the mean zonal flow, but which are not sheared out by the flow. This indicates that a vortex may exist in a counterrotating shear, provided that the vortex is sufficiently strong. This is consistent with calculations for the behaviour of a patch of constant vorticity in a background flow with constant shear and strain (Moore and Saffman 1971; Kida 1981; Meacham *et al.* 1990), which show that counterrotating vortices are sheared out if the absolute value of their vorticity is less than about six times the vorticity of the mean flow.

Vortices which are stable in the absence of the mean zonal flow are also stable in a mean zonal shear with the same sign of vorticity as the vortex. While these vortices are stable, they are not necessarily steady: the aspect ratio and orientation of the vortex varies quasi-periodically. These oscillations are qualitatively similar to the nutating solutions found by Kida (1981) and Meacham *et al.* (1990), and which were used by Polvani *et al.* (1990) to explain the variations in shape of Neptune's Great Dark Spot. Our results indicate that periodic variations in the shape and orientation of vortices can occur in models with continuous vorticity distributions.

Oscillations of vortex shape in a model with a continuous vorticity distribution have also been seen by Marcus (1990). However, Marcus found that the oscillations in shape damped out in a few vortex turnaround times, provided that the background flow contained numerous small-scale filaments of vorticity (which our simulations do not have), resulting in a steady vortex.

2.5. Effects of β

We now consider the effects of a meridional gradient of the Coriolis parameter (the β effect) upon the time evolution of vortices. The behavior of isolated, monopolar vortices on the β -plane in the absence of a mean zonal flow has received considerable attention. Using a linearized, quasi-geostrophic, single-layer model, Flierl (1977) found that Rossby wave dispersion will cause vortices to propagate westward and decay in amplitude, with the drift rate approaching the maximum Rossby wave speed at large times. Numerical simulations by McWilliams and Flierl (1979) using a nonlinear, two-mode (the barotropic and one baroclinic mode), quasi-geostrophic model show that nonlinear effects reduce the decay rate and allow meridional propagation of the vortex (equatorward for anticyclonic vortices, poleward for cyclonic vortices). As the nonlinearity increases, or as the size of the vortex relative to the deformation radius increases, the propagation rate of the vortex relative to the fastest linear wave velocity increases; the limiting propagation speed is the maximum Rossby wave group velocity ($-\beta/\lambda_1^2$ in the zonal direction, $-\beta/4\lambda_1^2$ in the meridional direction). They also found that with a purely baroclinic initial vortex, a vortex pair (dipole) spins up in the barotropic mode, resulting in a structure similar to the dipole modon with baroclinic rider found by Flierl *et al.* (1980). This can slow down the westward propagation of the baroclinic vortex or result in eastward propagation.

Calculations with a two-layer primitive equation model (Mied and Lindemann 1979) give similar results. More recent results with single layer shallow water mod-

els show that anticyclonic vortices propagate westward faster than cyclonic vortices (Davey and Killworth 1984; Williams and Yamagata 1984; McWilliams *et al.* 1986; Williams and Wilson 1988); differences between cyclones and anticyclones cannot occur in a quasi-geostrophic model, as the quasi-geostrophic equations are invariant under the transformation $(x, y, \psi) \leftrightarrow (x, -y, -\psi)$.

We have examined the effect of our fluid lower boundary on the behavior of an isolated vortex on a quasi-geostrophic β plane. An example is shown in Fig. 2.21a for a purely first baroclinic mode vortex with $\alpha = 0.0$, $\lambda_1^2 = 1.0$, $U_0 = 0.0$ and $\beta = 0.3$. The anticyclonic vortex drifts westward and equatorward and the peak amplitude of the streamfunction decays, with a weak radiation field forming east of the vortex. The zonal and meridional drift rates are -0.162 and -0.073 respectively, which can be compared to the maximum amplitude Rossby wave group velocities of $-\beta/\lambda_1^2 = -0.3$ zonally and $-\beta/4\lambda_1^2 = -0.075$ meridionally. The meridional drift rate of the vortex is very close to the maximum meridional Rossby wave speed, while the zonal drift rate of the vortex is only about half of the maximum zonal Rossby wave speed. This is similar to what was observed by McWilliams and Flierl (1979) for an equivalent barotropic model vortex in the same parameter regime. In contrast to the two mode model of McWilliams and Flierl (1979), our model does not allow a dipole to spin up in the barotropic mode since for a Jovian atmosphere, with a deep fluid interior, the barotropic mode is not affected by the baroclinic modes. We also do not see a spin-up of a dipole in the second baroclinic mode; while a small disturbance forms in the second mode, its amplitude is two orders of magnitude smaller than the amplitude of the first baroclinic mode vortex.

When a mean zonal shear flow is present, the westward propagation still occurs, but the southward propagation and the amplitude decay are inhibited if the shear is sufficiently strong relative to the vorticity of the vortex (or the beta effect is sufficiently

Figure 2.21a. Behavior of a vortex on a β -plane with no mean zonal shear flow.

Time evolution of the streamfunction at 690 mbar of an f -plane vortex with $\alpha = 0.0$, $\lambda_1^2 = 1.0$, $U_0 = 0.0$ and $\beta = 0.3$ at times 5.94, 11.87, 17.81 and 23.75. The contour interval is 0.25 and negative contours are dashed.

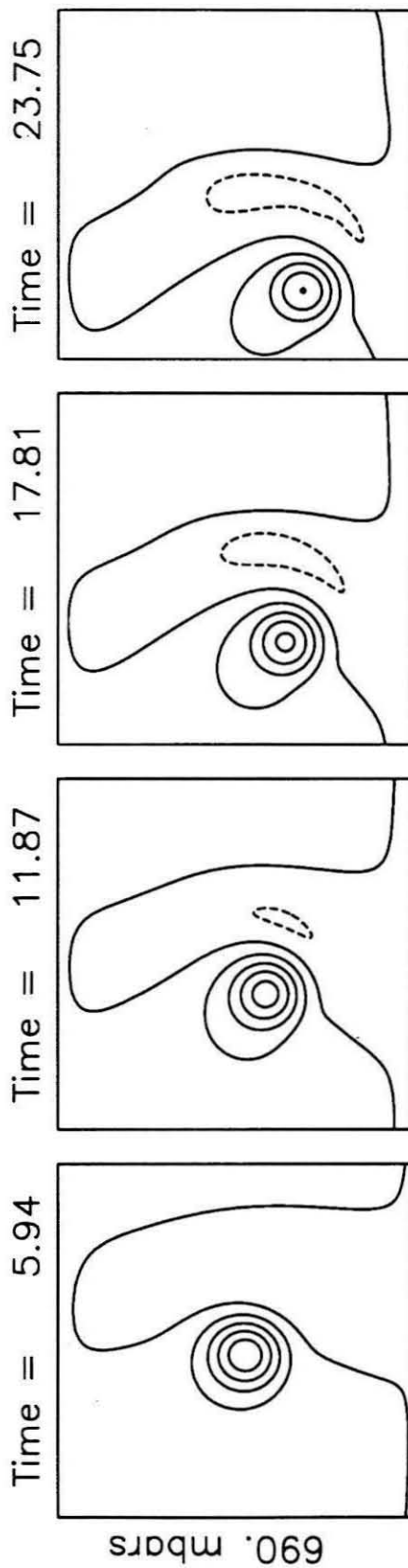


Figure 2.21b. Behavior of a vortex on a β -plane with a mean zonal shear flow.

Time evolution of the streamfunction at 690 mbar of an f -plane vortex with $\alpha = 0.0$, $\lambda_1^2 = 1.0$, $U_0 = 0.5$ and $\beta = 0.3$ at times 5.94, 23.75, 41.56 and 59.37. The contour interval is 0.25 and negative contours are dashed. Contours for $\psi < -2.0$ are not shown.

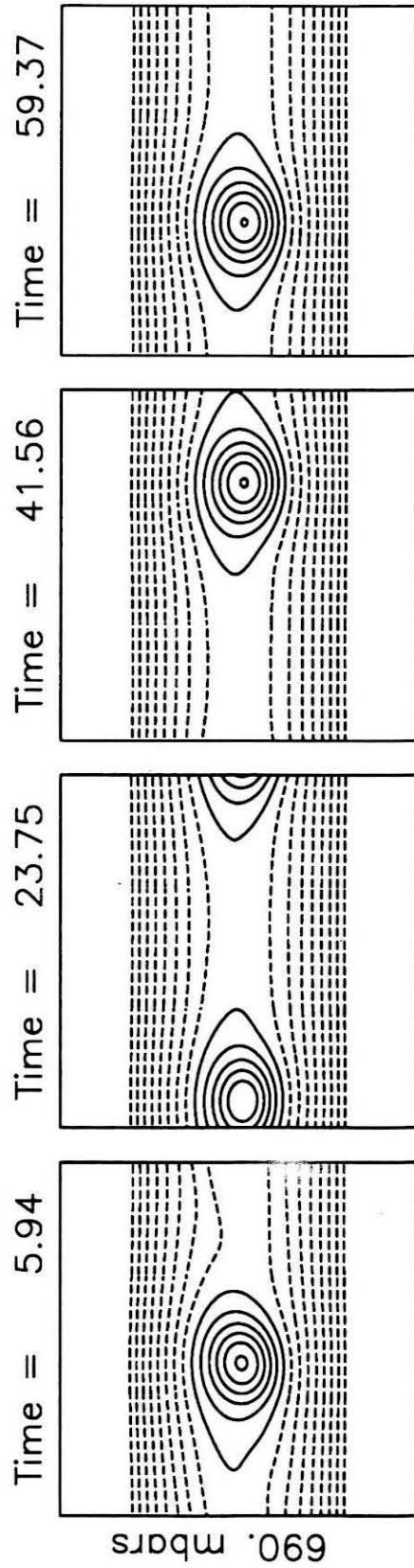
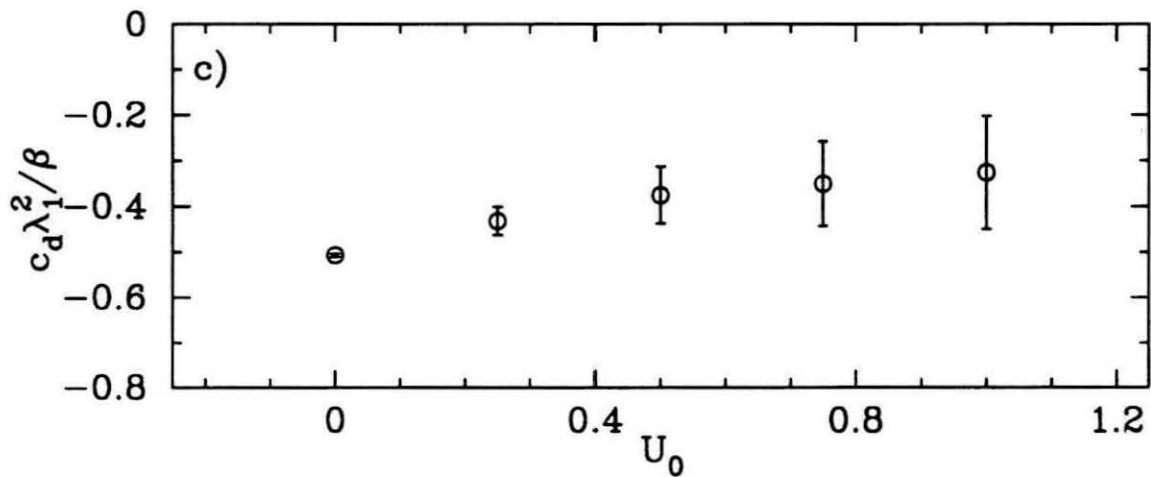
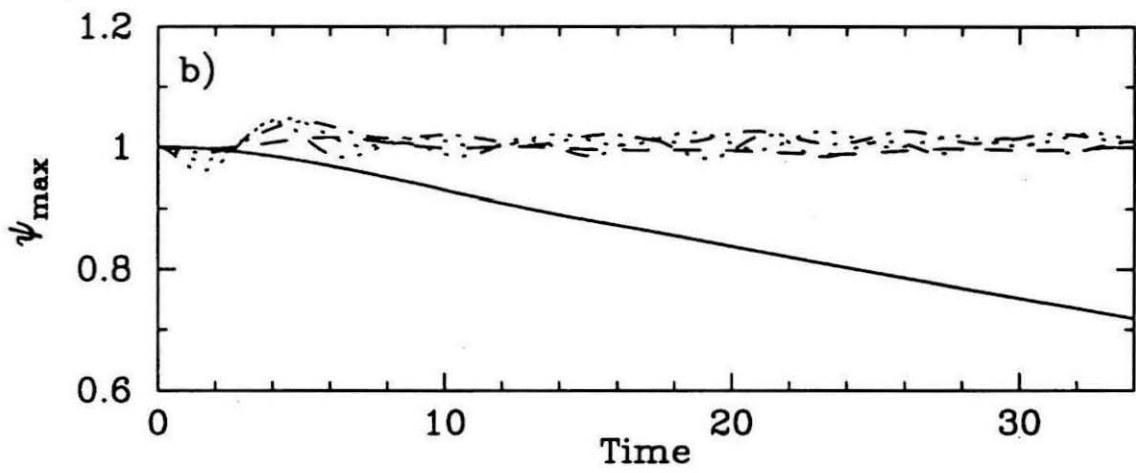
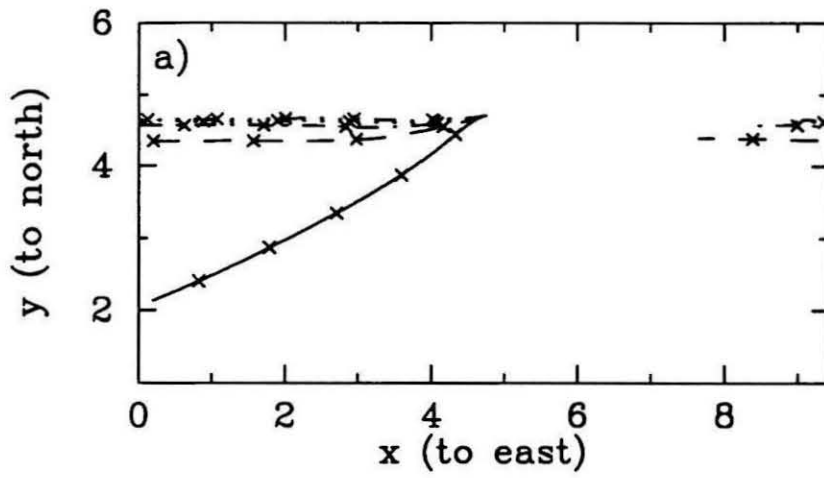


Figure 2.22. Effect of changing U_0 on the propagation and decay of vortices with $\alpha = 0.0$, $\lambda = 1.0$ and $\beta = 0.3$. a) Trajectories of the vortex from times $0 \leq t \leq 34$. for $U_0 = 0$ (solid lines), $U_0 = 0.25$ (dashed lines), $U_0 = 0.5$ (dot-dashed lines), $U_0 = 0.75$ (dotted line) and $U_0 = 1.0$ (dot-dot-dot-dashed line). The crosses are at time intervals of 5.96. b) Maximum of the perturbation streamfunction amplitude at 690 mbar ($\psi(z = 690\text{mbar}) - \psi_0$) as a function of time for $U_0 = 0$ (solid lines), $U_0 = 0.25$ (dashed lines), $U_0 = 0.5$ (dot-dashed lines), $U_0 = 0.75$ (dotted line) and $U_0 = 1.0$ (dot-dot-dot-dashed line). c) Drift rate of the vortex relative to the mean zonal flow at the latitude of the maximum of the vortex streamfunction, normalized by the maximum Rossby wave speed $\beta\lambda_1^{-2}$, as a function of the strength of the mean zonal shear U_0 . The errors are caused primarily by the uncertainty in the latitude of the vortex of plus or minus one-half of the grid spacing.



weak). This is demonstrated in Fig. 2.22, where the trajectories, peak amplitudes as a function of time, and zonal drift rates relative to the mean zonal flow at the latitude of the extrema of the streamfunction are shown for vortices with $\alpha = 0$, $\beta = 0.3$, $\lambda_1^2 = 1.0$ and various values of U_0 . In the presence of a mean zonal flow, the meridional propagation rate rapidly decreases to zero, and the amplitude of the vortex oscillates instead of slowly decaying (the small amplitude oscillations also occur when $\beta = 0$, and are the result interactions with the mean zonal flow; they are accompanied by quasi-periodic oscillations in the aspect ratio and orientation of the vortex similar to those discussed in Section 2.4 for stable vortices in shear). Increasing the strength of the zonal flow decreases the meridional drift of the vortex, and may also slightly decrease the zonal drift rate relative to the mean flow, although this is unclear due to the uncertainties in the drift rate. These uncertainties are primarily due to the uncertainty in the latitude of the vortex, which creates an uncertainty in the mean zonal flow speed at the center of the vortex.

The role of the mean zonal flow in preventing the decay of the vortex can be understood by calculating the contributions to the time derivative of the streamfunction from each of the terms in (2.6), in a reference frame moving with the vortex. This is shown in Fig. 2.23 for the case $\alpha = 0$, $\lambda_1^2 = 1$, $U_0 = 0.5$ and $\beta = 0.3$ at time 37.5. Since the amplitude of the second baroclinic mode is much smaller than the amplitude of the first baroclinic mode, only the terms involving the contributions of the barotropic and first baroclinic modes to the evolution of the first baroclinic mode are shown. The linear dispersion term is approximately balanced by the net advection of first mode potential vorticity. Advection of the first mode potential vorticity both by the mean zonal flow (the barotropic mode, in this case) and by the vortex itself are necessary for the advection to balance the dispersion; both nonlinearity and a mean zonal flow play a role in preventing the decay of the vortex. Malanotte-Rizzoli

(1982) has shown that either a mean zonal shear or variable bottom topography are necessary for the existence of steady solutions on the quasi-geostrophic β -plane. (For our Jovian models, variable bottom topography is equivalent to a flow in the deep interior, i.e., a non-trivial barotropic mode).

The dependence of vortex decay and propagation on β is shown in Fig. 2.24, for vortices with $\alpha = 0.0$, $\lambda_1^2 = 1.0$ and $U_0 = 0.5$. We have shown the meridional positions as a function of time instead of the trajectories because the trajectories are dominated by the zonal motions. As β is increased, the distance which the vortex drifts meridionally before assuming predominantly zonal motion becomes greater, and the amount by which the amplitude of the vortex decreases also becomes greater.

When β becomes large enough, the zonal flow is no longer able to prevent the meridional propagation and decay of the vortex, as the interaction between the vortex and the mean zonal flow is no longer strong enough to balance the linear dispersion. The drift rate of the vortex relative to the mean zonal flow is a roughly constant fraction of the maximum Rossby wave speed as β varies. Since the Rossby wave speed is proportional to β , the drift rate of the vortex in dimensional units is also roughly proportional to β .

Figure 2.25 shows the dependence of vortex decay and propagation on the size of the vortex relative to the first internal deformation radius, for vortices with $\alpha = 0.0$, $\beta = 0.3$, and $U_0 = 0.5$. Decreasing the size of the vortex (or increasing the deformation radius) results in a greater meridional propagation of the vortex before its drift becomes zonal. The amplitude behavior as λ_1^2 changes is more complicated. For values of $\lambda_1^2 \geq 0.1$, the amplitude of the vortex oscillates but does not decay. At smaller values of λ_1^2 , there is a gradual decay in amplitude, as well as short period oscillations in amplitude (with periods roughly of order of the vortex turnaround time) superimposed on longer period variations in the vortex amplitude. These longer

Figure 2.23. Dominant terms contributing to the time rate of change of the first mode streamfunction $(\partial\psi_1/\partial t)$ for the stable vortex on a β -plane with $\alpha = 0.0$, $\lambda_1^2 = 1.0$, $\beta = 0.3$ and $U_0 = 0.5$ at time $t = 37.5$. a) linear dispersion term $(\nabla^2 - \lambda_1^2)^{-1} (\beta d\psi/dx)$. b) Advection of first baroclinic mode potential vorticity by the barotropic flow $(\nabla^2 - \lambda_1^2)^{-1} J(\psi_0, \nabla^2\psi_1 - \lambda_1^2\psi_1)$. c) Advection of first baroclinic mode potential vorticity by the first baroclinic mode $\gamma_{111} (\nabla^2 - \lambda_1^2)^{-1} J(\psi_1, \nabla^2\psi_1 - \lambda_1^2\psi_1)$. d) Net advection of first baroclinic mode potential vorticity (b) + (c). The contour interval is 0.02 and negative contours are dashed.

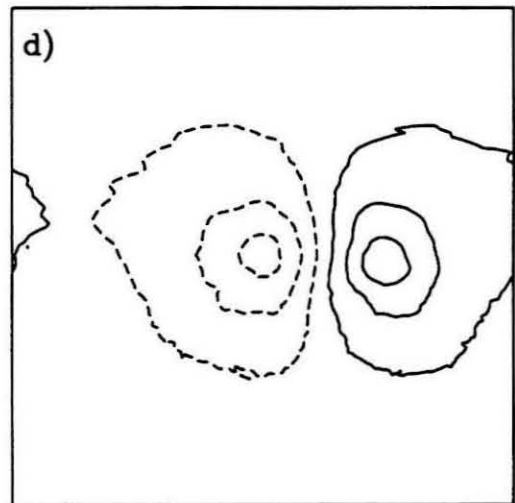
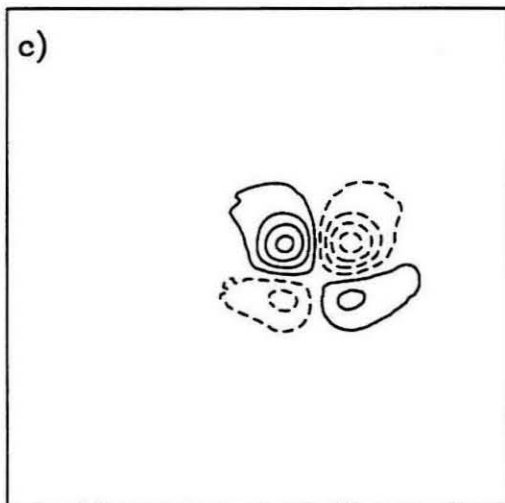
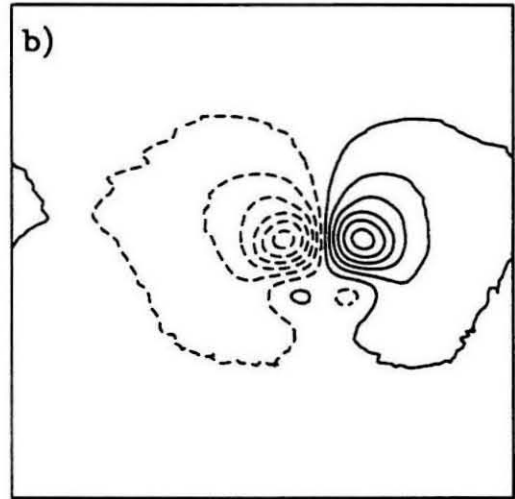
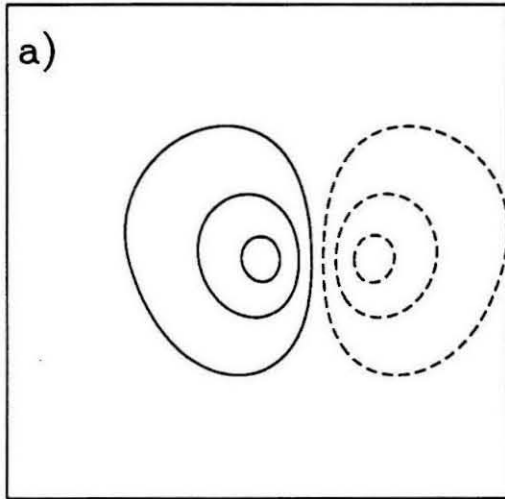


Figure 2.24. Effect of changing β on the propagation and decay of vortices with $\alpha = 0.0$, $\lambda = 1.0$ and $U_0 = 0.5$. a) Latitude as a function of time and b) peak perturbation streamfunction amplitudes $\psi(z = 690\text{mbar}) - \psi_0$ as a function of time for $\beta = 0.25$ (solid lines), $\beta = 0.5$ (dashed lines), $\beta = 0.75$ (dot-dashed lines), $\beta = 1.0$ (dotted line) and $\beta = 1.5$ (dot-dot-dot-dashed line). c) Drift rate of the vortex relative to the mean zonal flow at the latitude of the peak of the vortex streamfunction, normalized by the maximum Rossby wave speed $\beta\lambda_1^{-2}$, as a function of β .

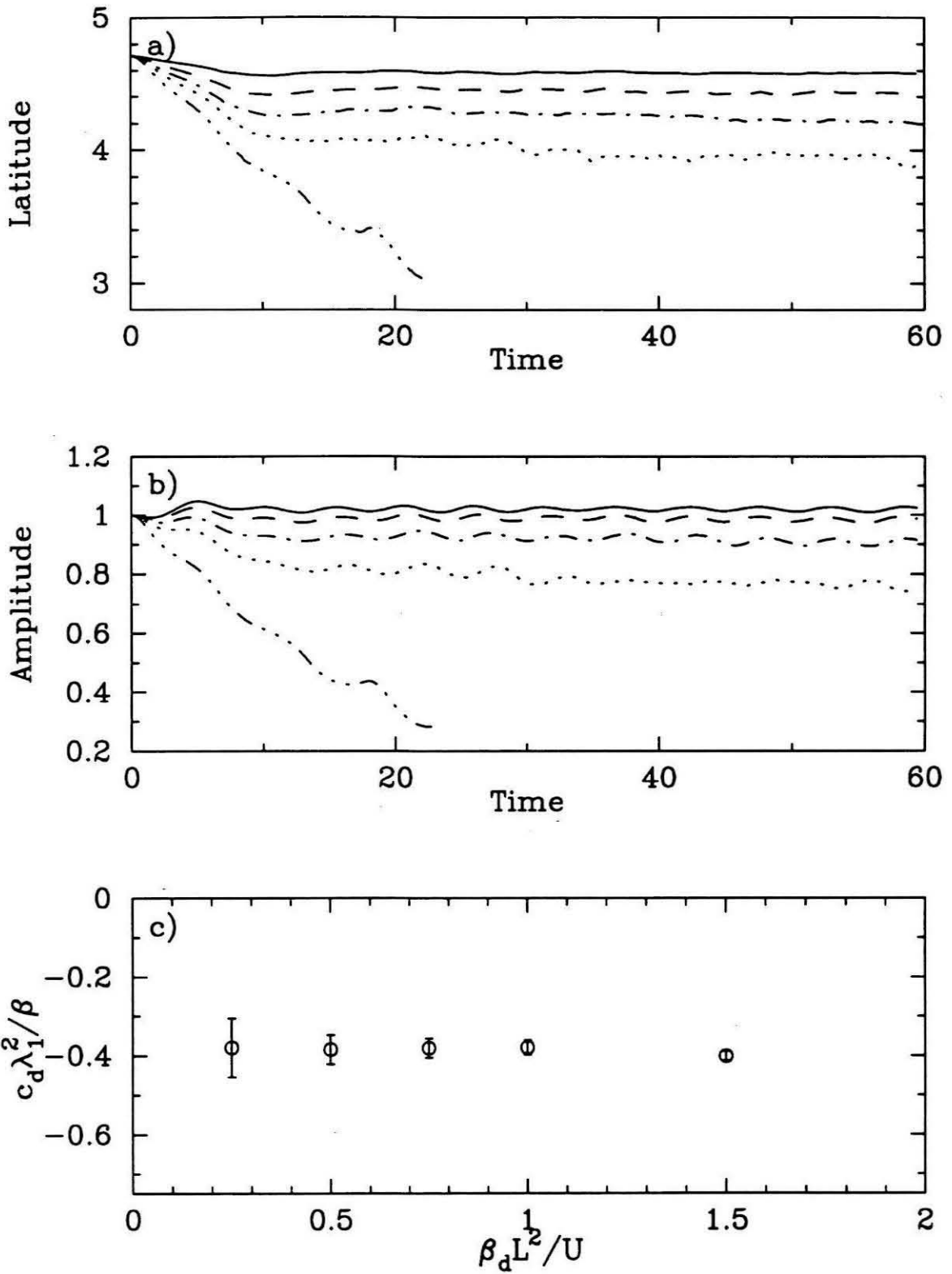
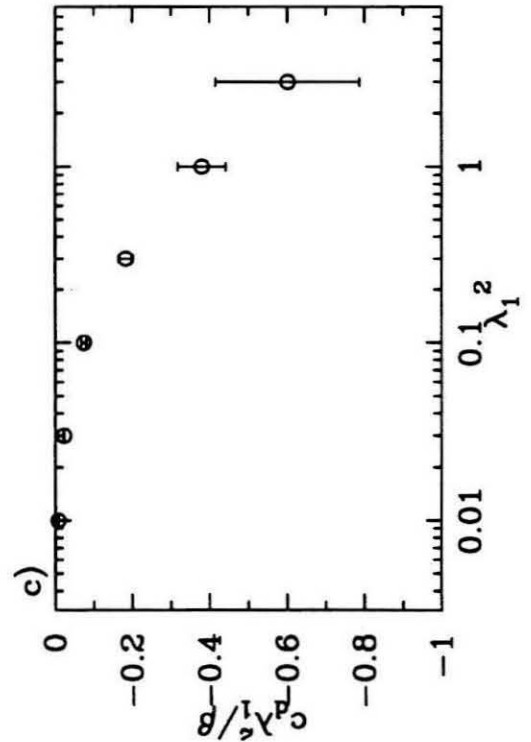
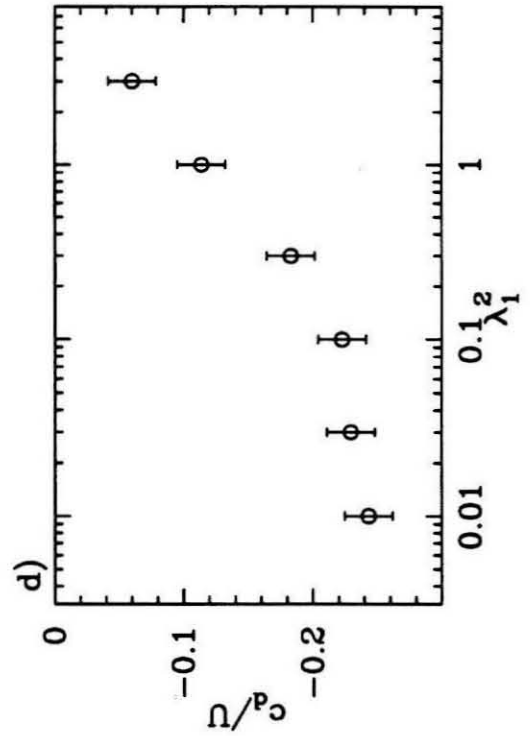
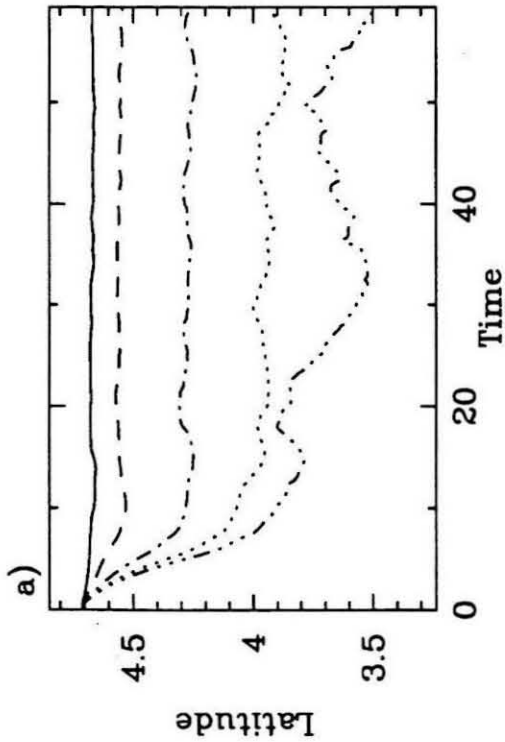
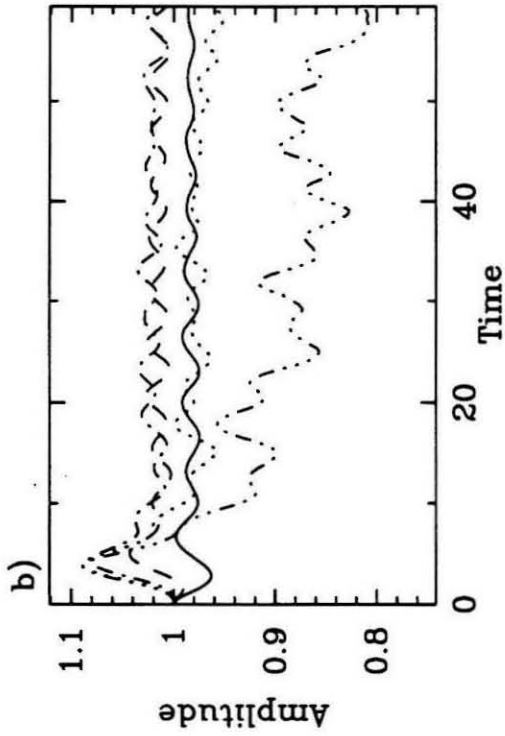


Figure 2.25. Effect of changing λ_1^2 on the propagation and decay of vortices with $\alpha = 0.0$, $U_0 = 0.5$ and $\beta = 0.3$. a) Latitude as a function of time and b) peak perturbation streamfunction amplitudes $\psi(z = 690\text{mbar}) - \psi_0$ as a function of time for $\lambda_1^2 = 3.0$ (solid lines), $\lambda_1^2 = 1.0$ (dashed lines), $\lambda_1^2 = 0.3$ (dot-dashed lines), $\lambda_1^2 = 0.1$ (dotted line) and $\lambda_1^2 = 0.3$ (dot-dot-dot-dashed line). c) Drift rate of the vortex relative to the mean zonal flow at the latitude of the peak of the vortex streamfunction, normalized by the maximum Rossby wave speed $\beta\lambda_1^{-2}$, as a function of λ_1^2 . d) Drift rate of the vortex relative to the mean zonal flow at the latitude of the peak of the vortex streamfunction, normalized by the velocity scale of the vortex, as a function of λ_1^2 .



period amplitude oscillations correspond with oscillations in the latitude of the vortex, and are the result of the vertical fragmentation of the vortex by internal barotropic instability resulting in oscillations in the latitude and longitude of the vortex, as was discussed in Section 2.4. The drift rate of the vortex relative to the zonal flow becomes much smaller relative to the maximum Rossby wave speed as the size of the vortex relative to the radius of deformation decreases. This happens because the maximum Rossby wave speed is proportional to the square of the deformation radius; the drift rate non-dimensionalized by the velocity scale of the vortex actually increases as the size of the vortex relative to the deformation radius decreases (Fig. 2.25d).

We have also examined the effects of non-zero β term on the stability of vortices. The $U_0 = 0.5$ experiments of Section 2.4 were repeated using $\beta = 0.3$. For the baroclinically driven instabilities, the main effect of a nonzero β is westward propagation of the vortex as the instability occurs, and the decay with time of any small or weak vortices produced by the instability. The effect of β on internal barotropic instability (vertical fragmentation) is much more pronounced: increasing the β term causes the growth rate of the instability to increase. Figure 2.26 shows the longitudinal and latitudinal positions of the vortex (in a reference frame moving at the average velocity of the upper layer vortex) for $\alpha = 0.5$, λ_1^2 , $U_0 = 0.5$ and two values of β : $\beta = 0.1$ and $\beta = 0.2$. These can be compared to Fig. 2.18, which shows the position for the same parameters, except that $\beta = 0.0$. Increasing β results in more rapid growth of the instability: final breakup of the vortex occurs at $t \approx 350$ for $\beta = 0.0$, at $t \approx 200$ for $\beta = 0.1$, and at $t \approx 100$ for $\beta = 0.2$. With $\beta = 0.3$ we also find weak oscillations in latitude and longitude for some vortices with $\lambda_1^2 = 0.3$ which are stable when $\beta = 0.0$. However, the amplitude of the oscillations is only one or two times the grid spacing, and may not be real. As discussed earlier in this section, vortices which are stable on the f -plane can also be stable and long-lived on the β -plane, provided

that the mean zonal shear flow is strong enough for the non-linear interaction between the vortex and the shear flow to balance linear Rossby wave dispersion.

2.6. Application to Jovian Planets

We now wish to compare the results of our numerical models to observations of vortices on the Jovian planets, and to use these comparisons to infer information about the vertical structure of Jupiter's atmosphere. In particular, we will use observations of longitudinal oscillations in the positions of vortices to estimate lower limits on the deformation radii of Jupiter and Neptune. We will also discuss the possibility of using measurements of vortex drift rates to place constraints on Jupiter's mean zonal flow below the level of the observed clouds.

One important result of our models is that vortices which are stable, or which appear to be stable when seen only from the cloud tops, exist over the range of sizes examined, with radii varying from one-tenth the deformation radius to about twice the deformation radius. Although we did not model larger vortices for computational reasons (the number of grid points required to adequately resolve the deformation radius of the second mode becomes prohibitively large for big vortices), previous studies show that barotropic vortices larger than twice the deformation radius are linearly stable in a two-layer model (Flierl 1988) and are non-linearly stable in a barotropic model (e.g., Williams and Wilson 1988; Dowling and Ingersoll 1989). Furthermore, the decay of vortices due to Rossby wave radiation can be inhibited by a mean zonal flow, so that long-lived vortices can exist in the presence of a β -effect.

2.6.1 Longitudinal Oscillation of Vortex Positions

Vertical fragmentation by internal barotropic instability in the presence of a mean zonal shear results in oscillations of the latitude and longitude of the vortex. Several examples of vortices which oscillate in longitude are known. The most famous is the

Figure 2.26a. Latitude and longitude of the vortex for $\alpha = 0.5$, $\lambda_1^2 = 0.03$, $U_0 = 0.5$ and $\beta = 0.1$ as a function of time evaluated at 690 mbar (solid line) and 3962 mbar (dotted line). The longitude is measured in a reference frame moving at the average zonal velocity of the 690 mbar component of the vortex.

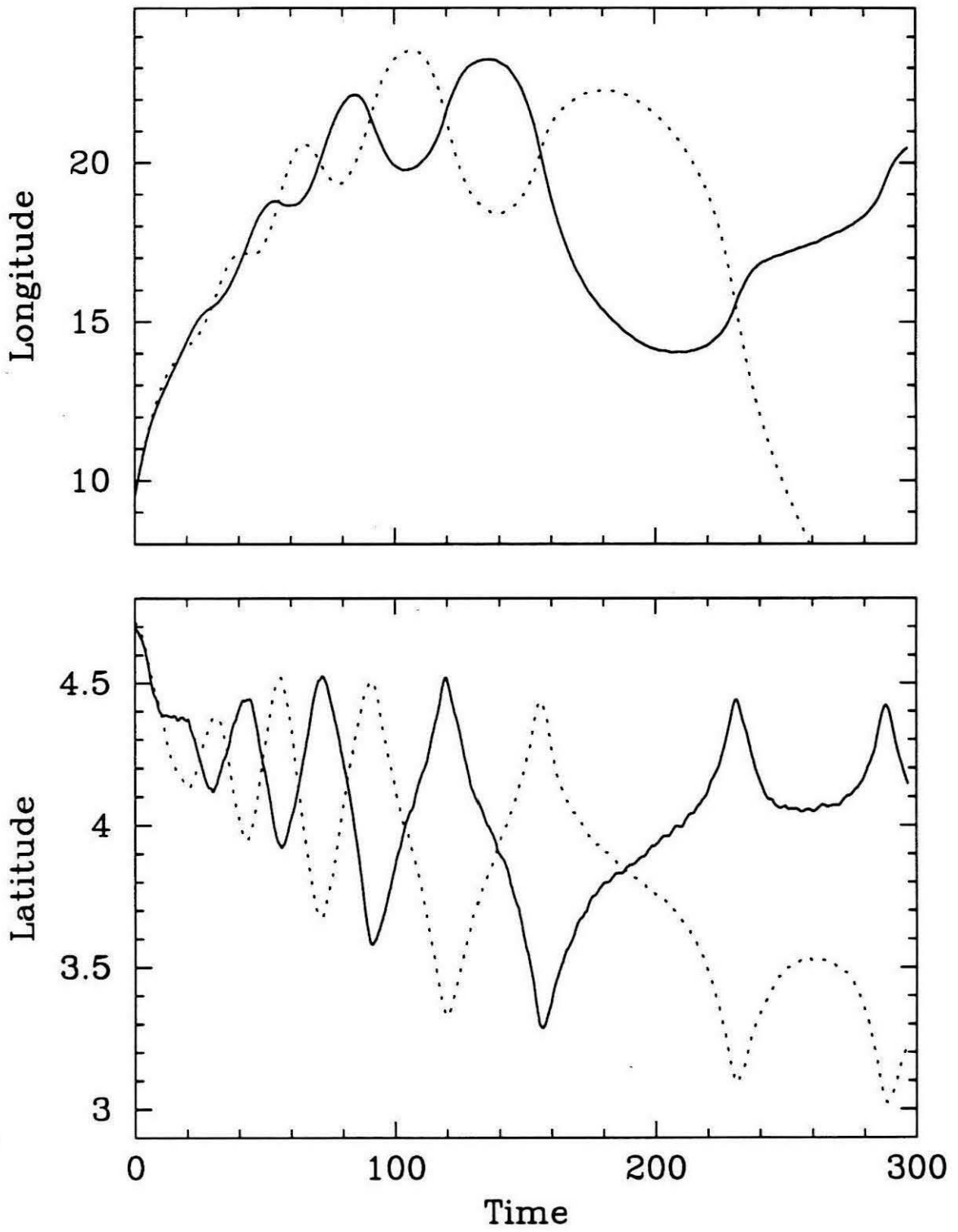
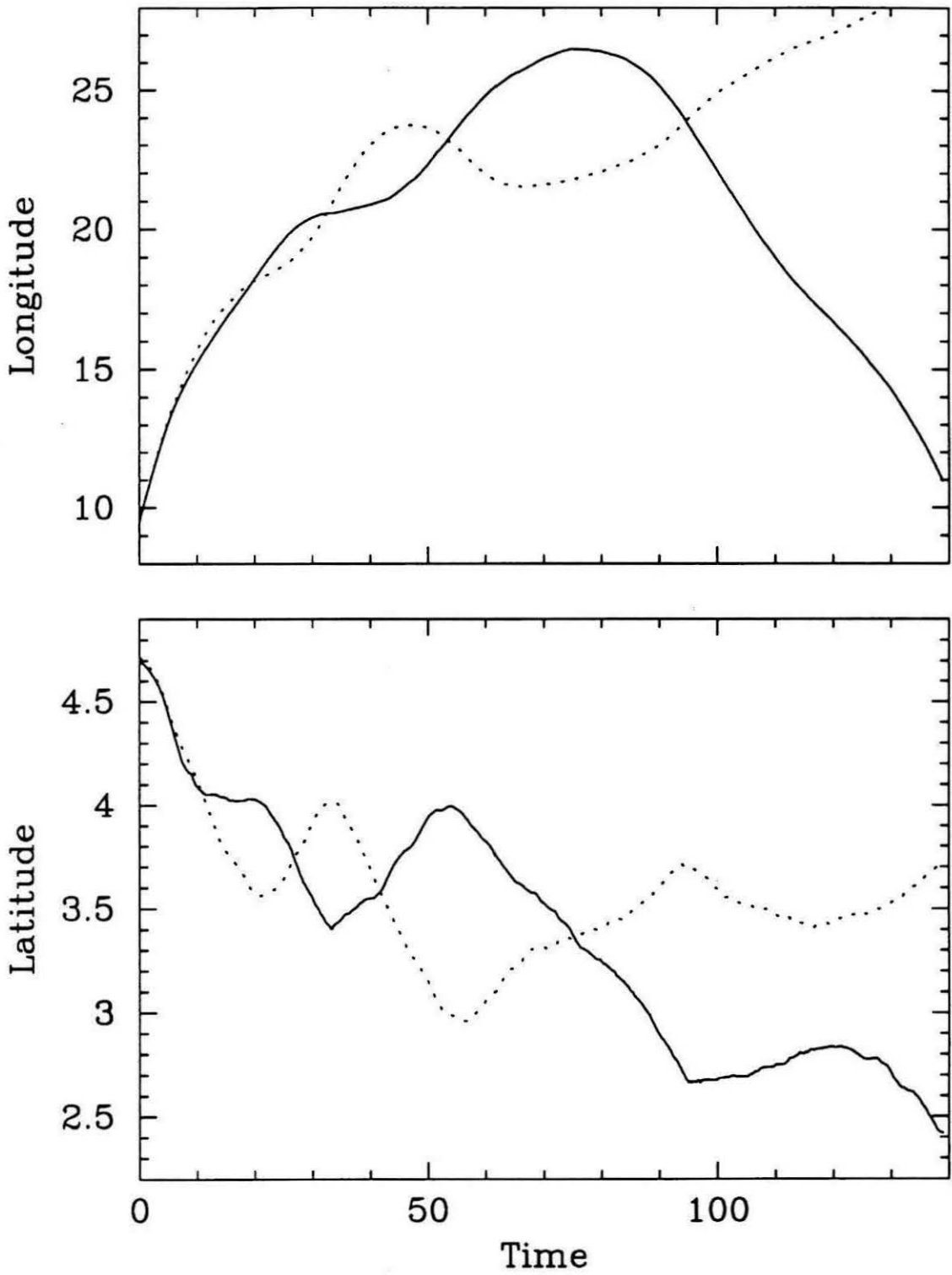


Figure 2.26b. Latitude and longitude of the vortex for $\alpha = 0.5$, $\lambda_1^2 = 0.03$, $U_0 = 0.5$ and $\beta = 0.2$ as a function of time evaluated at 690 mbar (solid line) and 3962 mbar (dotted line). The longitude is measured in a reference frame moving at the average zonal velocity of the 690 mbar component of the vortex.



Great Red Spot, whose longitude oscillates with a period of 89.89 ± 0.11 days and a mean amplitude of $0^\circ.77$ (Reese 1972) The oscillations persist even when the long term drift of the GRS changes. Other examples include observations by Reese and Smith (1966) of a spot in Jupiter's North Temperate belt that oscillated in longitude with a period of 300 days and an amplitude of 4° ; an observation by Reese (1971) of a spot on Saturn which oscillated with a period of 169 days and a peak-to-peak amplitude of 16° which decayed over time; two spots observed by Peek (1958) in 1940-41 and 1941-42, the first of which had a period of 72 days and a peak-to-peak amplitude of 20° and the second of which had a similar period and amplitude but which increased with time, and the second dark spot (D2) seen by Voyager 2 on Neptune (Hammel *et al.* 1989; Smith *et al.* 1989) which oscillated with a period of 25 days and an amplitude of about 50° in longitude and 5° in latitude.

The oscillating spot of 1941-42 (Peek, 1958, whose Fig. 9 shows the longitude of the spot as a function of time) shows the increase of period and amplitude with time which is seen with internal barotropic instability in a shear flow (e.g., Fig. 2.18b). Peek gives the size of the spot as "about the size of a satellite disk", which is 3000 to 5000 km depending upon the satellite, so we can estimate the length scale of the spot as ≈ 2000 km. Using a typical velocity in Jupiter's atmosphere of 50 m s^{-1} , this gives a timescale of $L/U = 4 \times 10^4$ s. The observed period of the oscillation is on the order of 45 days, which gives a non-dimensional period for the longitudinal oscillation of approximately 90, which is in the range of periods seen in our models (e.g., Fig 2.18b. which has a period of around 90 for the later oscillations). A detailed fit of the data to our models is not practical as the number of model parameters which affect the amplitude and period of the oscillation (vortex size, strength of the shear flow relative to the vortex, β and vertical structure of the vortex; also the amplitude and period of oscillation changes with time for any given vortex) is larger than the number of

observables. If the oscillation in longitude of this spot is due to internal barotropic instability, then the diameter of the spot is a rough lower limit on the first internal radius of deformation, giving a lower limit to the deformation radius on Jupiter of 3000 to 5000 km. This is at the upper end of the range of expected values for the deformation radius calculated by Ingersoll and Cuong (1981). Assuming that the deformation radius scales roughly as the square root of the water abundance as was found by Achterberg and Ingersoll (1989), this would imply a water abundance in the interior relative to hydrogen on the order of twenty times the solar oxygen to hydrogen ratio. We note also that this gives static stabilities a few times larger than those assumed in calculating the mode structures and interaction coefficients used in our numerical model.

The other spot whose oscillations in position are most consistent with internal barotropic instability is the Second Dark Spot on Neptune, also called D2. Figure 2.27 shows the time variations in the latitude and longitude of D2 as measured by Hammel *et al.* (1989) from *Voyager 2* observations, compared with one and one-half periods of a positional oscillation seen in our model for $s = 0.5$, $\lambda_1^2 = 0.03$, $U_0 = 0.5$ and $\beta = 0.0$. The observed amplitude of the oscillation in latitude is roughly one-half the latitudinal extent of the spot, and the amplitude of oscillation in longitude is about twenty times larger, and out of phase with the latitude oscillations by about 90 degrees. The observed period of 25 days is also consistent with our models: using the vorticity of the zonal flow, estimated at about $1 \times 10^{-5} \text{ s}^{-1}$ by Polvani *et al.* (1990), as an inverse timescale (U/L) gives a non-dimensional period for the positional oscillations of D2 of 22, consistent with what is observed in our models near the maximum value of λ_1^2 for which the instability occurs. The observations cover only one oscillation, so it cannot be determined if the amplitude and period are growing with time. The size of D2, as estimated from Fig. 2 of Smith *et al.* (1989) is approximately 7000 km in

longitude by 3000 km in latitude, which again indicates a large value for the first internal deformation radius on Neptune if the oscillations of position for D2 are in fact caused by internal barotropic instability. Polvani *et al.* (1990) estimated that the deformation radius must be larger than 7000 km at the latitude of the Great Dark Spot (GDS), 20°S, based on their model for the shape oscillations of the GDS. Since the deformation radius scales as the inverse of the Coriolis parameter, this implies that the radius of deformation at the latitude of D2 (55°S) must be greater than 3000 km, which is consistent with D2 being small enough for internal barotropic instability if the latitudinal extent of the vortex is the proper length scale. It should be emphasized that the parameters of our numerical model were derived from a model of Jupiter's atmosphere, that has a vertical thermal structure different from Neptune's, which will likely affect the instability boundaries.

The rest of these oscillations in position cannot directly be explained by vertical fragmentation due to internal barotropic instability. The Great Red Spot is much too large (it is almost certainly larger than the radius of deformation so that $\lambda_1^2 > 1$) and the amplitude of the oscillations too small. The oscillations of the spot on Saturn seen by Reese (1971) and of the vortex of 1940-41 seen by Peek (1958) decay with time instead of growing. The 300 day period of the spot seen by Reese and Smith (1966) is much longer than any of the oscillation periods found in our models; the longest periods in our models are around $150(L/U)$, occurring for vortices with diameters around one-fifth of the radius of deformation, which would require $L/U \approx 2$ days for a 300 day oscillation period. Since the length of the spot is about 6000 km (or $L \approx 3000$ km), this would require $U \approx 15 \text{ m s}^{-1}$, which is somewhat small compared to typical flow velocities on Jupiter.

Although many of the observed oscillations in longitude cannot be explained directly as internal barotropic instability, it is interesting to speculate that a tilt in

the vertical axis of a vortex (i.e., variations with altitude of the location of the vortex) may cause oscillations in the position of an otherwise stable vortex as seen at one altitude (such as the cloud tops).

We have made preliminary attempts to model the behavior of stable vortices which have been strongly perturbed so that the upper and lower layer portions of the vortex are offset. The results show oscillations in the latitude and longitude of the vortex. The amplitude of the oscillations decays to below the resolution of the model after a few times the oscillation period. Some examples are shown in Fig. 2.28 for $s = 0.5$, $U_0 = 0.5$ and $\beta = 0.0$ with $\lambda_1^2 = 1.0$ and $\lambda_2^2 = 0.3$.

This could explain some of the observations of vortices which show decaying longitudinal oscillations, although it appears that matching the observed oscillation periods could be a problem. Polvani (1991) considered the problem of vortex alignment in a two-layer, f -plane, contour dynamics model with no mean zonal flow, in which he examined the evolution of an initial condition with two patches of constant vorticity, one in each layer. He found that if the distance between the centers of the upper and lower vortex is large enough or *small enough*, or if the radius of the vortex is smaller than the deformation radius, that the vortices will rotate around each other without their centers moving closer together (see e.g., Polvani's Fig. 4), resulting in oscillations in the position of the vortex. At intermediate separations, the distance between the centers of the upper and lower vortices decreases while the vortices rotate around each other, resulting in oscillations in position which decrease with time. This suggests that, in the context of a two-layer model, if some process causes a vortex to become tilted so that its position is different in the two layers, the latitude and longitude of the vortex in each layer will oscillate with time due to advection by the displaced vorticity in the other layer, and the oscillations may or may not damp with time depending upon the size of the vortex and the amount by which

Figure 2.27. Positional oscillations of Neptune's Second Dark Spot, compared with a model vortex. a) Planetographic latitude (*) and longitude (x) of Neptune's Second Dark Spot as a function of time. Longitude is plotted in a reference frame with a rotational period of 16.07 hours, which minimizes the variations in longitude. b) Latitude and longitude of a vortex for $s = 0.5$, $\lambda_1^2 = 0.03$, $U_0 = 0.5$ and $\beta = 0.0$, evaluated at 690 mbar. Because D2 is an anticyclone, while the model corresponds to a cyclonic vortex in the Southern hemisphere, the phase shift between the latitude and longitude oscillations is 180 different between D2 and the model vortex.

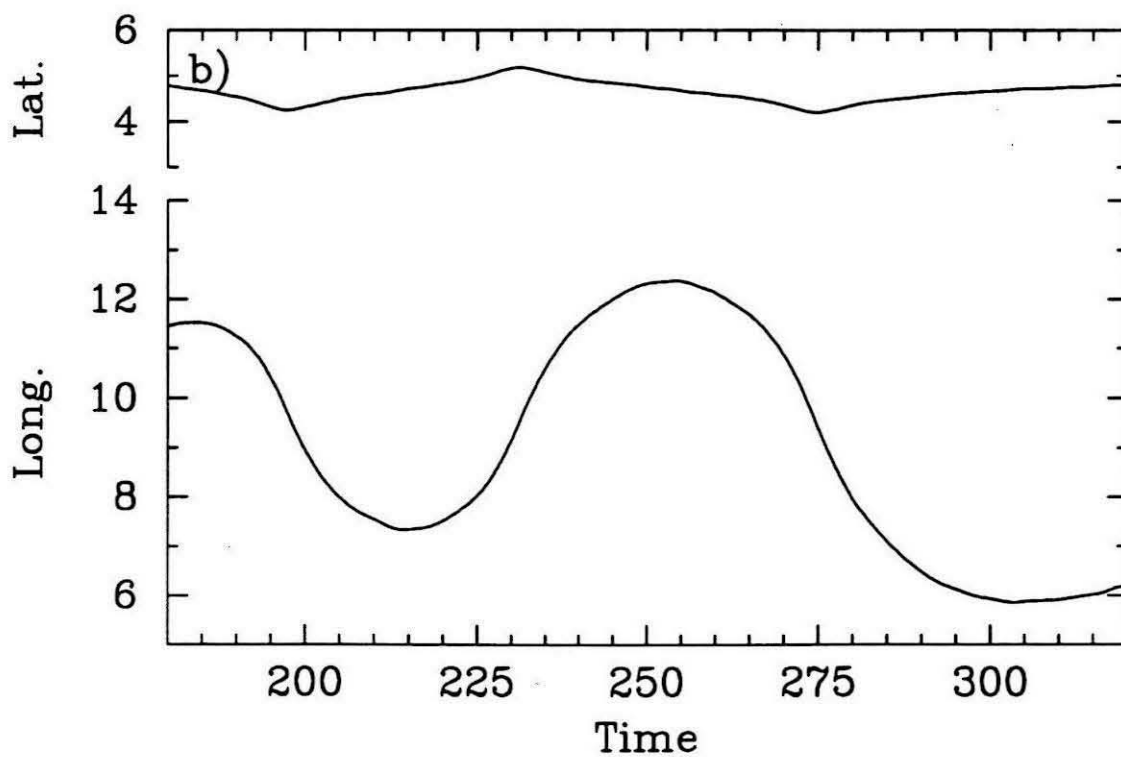
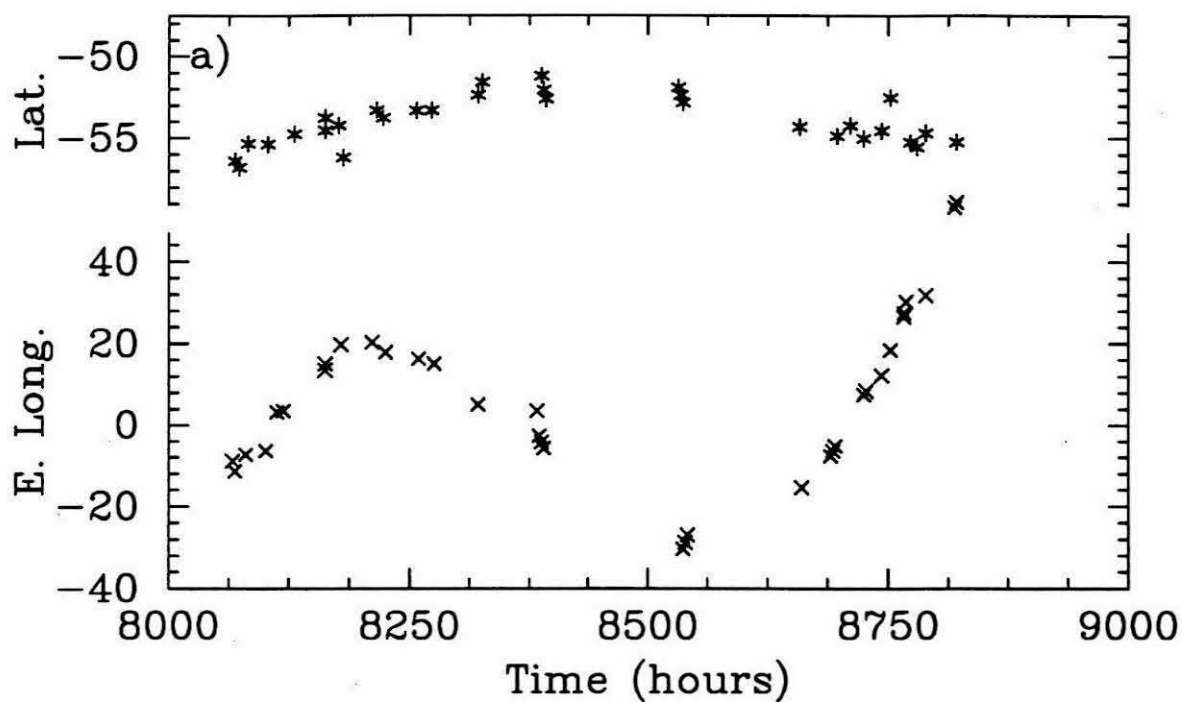


Figure 2.28a. Positional oscillations of a perturbed vortex. Latitude and longitude of a vortex for $s = 0.5$, $\lambda_1^2 = 1.0$ and $U_0 = 0.5$, evaluated at 690 mbar (solid line) and 3962 mbar (dotted line). The initial vortex was perturbed so that the center of the vortex at 690 mbar and the center of the vortex at 3962 mbar were separated by approximately 0.6 times the vortex radius. The upper panel shows the longitude as a function of time, and the lower panel shows the latitude as a function of time.

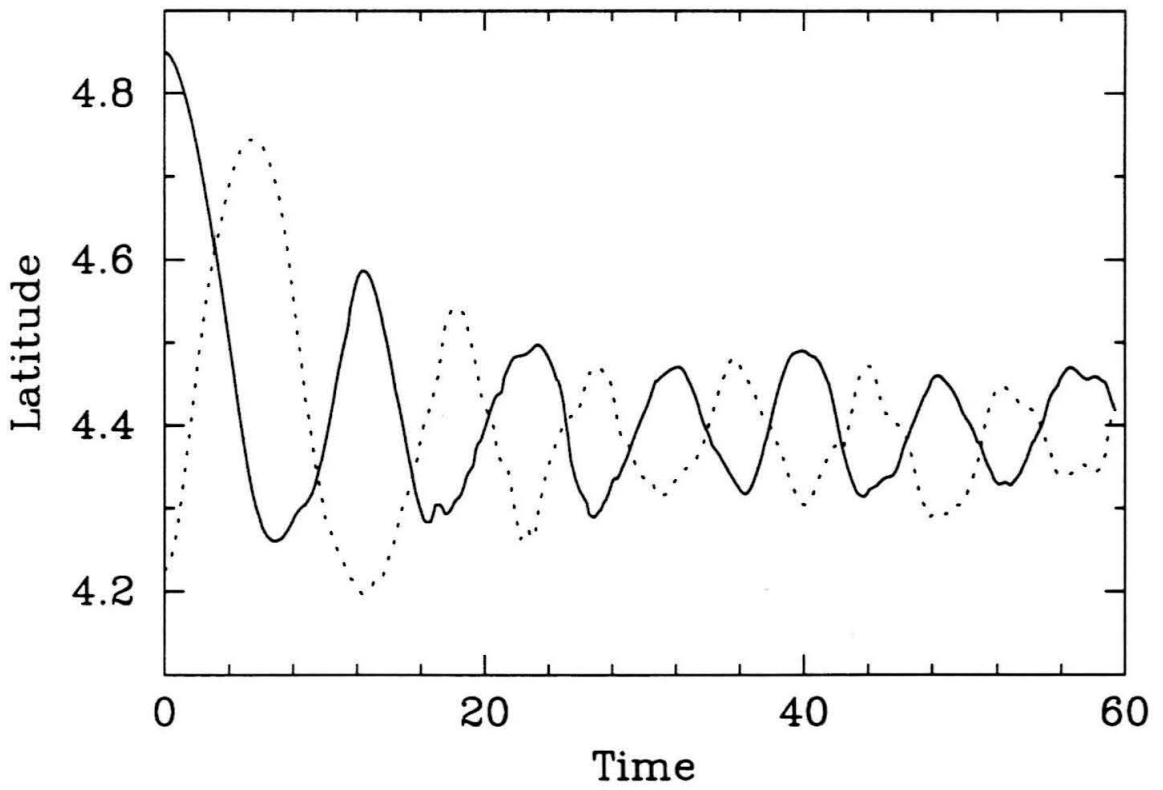
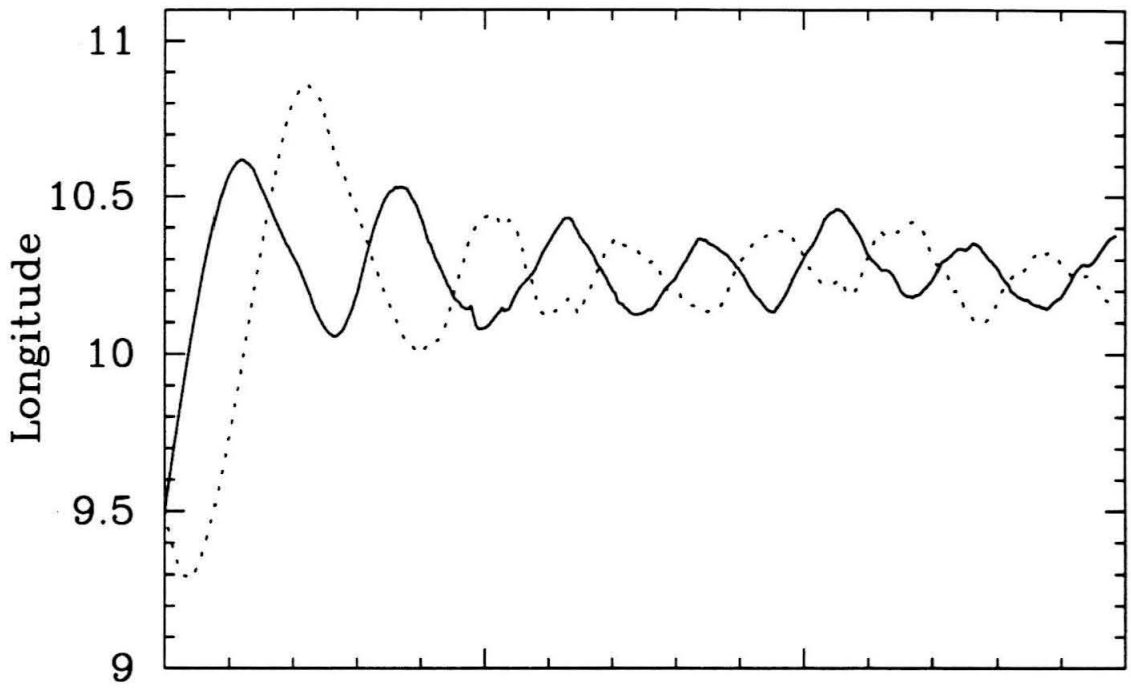
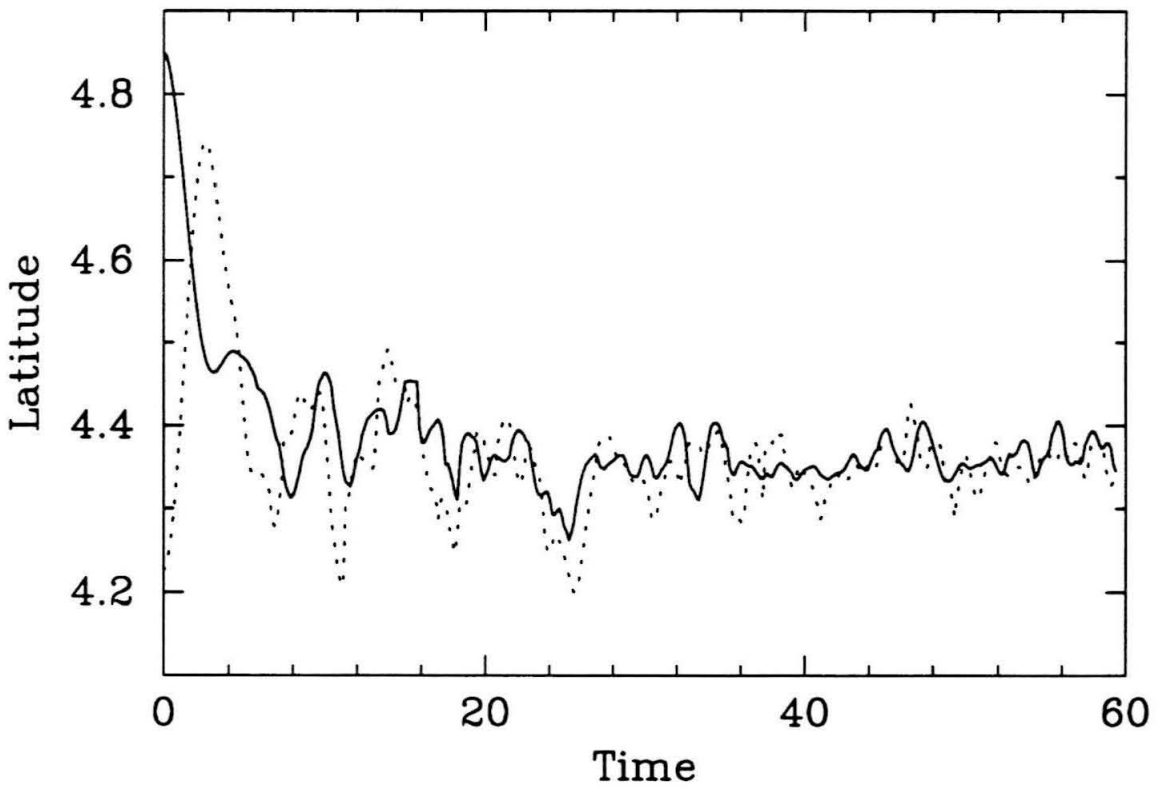
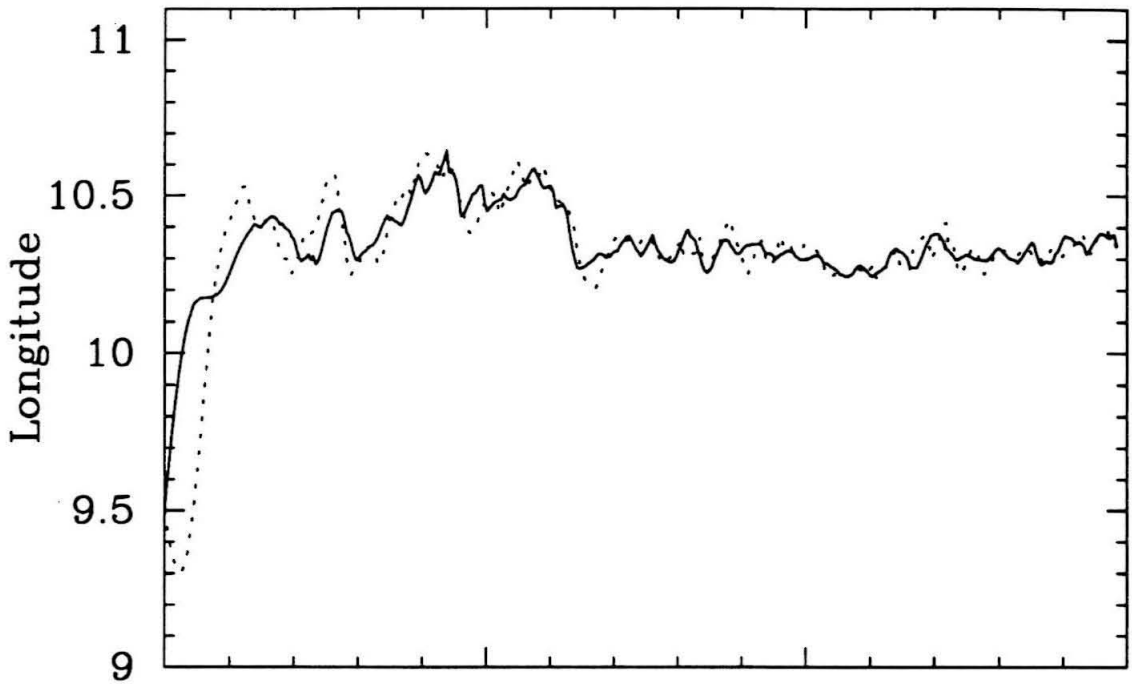


Figure 2.28b. As Fig. 2.28a, but with $\lambda_1^2 = 0.3$.



the components of the vortex in each layer are offset relative to each other. Whether or not this will work with continuous vorticity distributions and with a mean zonal flow, and mechanisms for causing the tilting of the vortex, is an interesting topic for future research.

2.6.2 Propagation of Vortices

In Section 2.5 we found that the β effect results in the westward propagation of vortices relative to the mean zonal flow. Determinations of the drift rates of vortices have been measured from groundbased observations since the late 1800's (Peek 1958), but the drift rates cannot be compared to the velocity of the mean zonal flow since the propagation rates of the vortices themselves (along with the velocities of any other features seen in the clouds) are used in determining the mean zonal flow velocity. Our models show that vortices can drift relative to the mean zonal flow by velocities on the order of the maximum Rossby wave speed. This will introduce errors when using the vortices to determine the velocity of the mean zonal flow. The error introduced by assuming that the vortices are simply advected by the zonal flow can be estimated by comparing the maximum Rossby wave speed to the observed mean zonal flow velocities. The maximum Rossby wave speed is given by β/λ_1^2 , which is simply β times the square of the internal radius of deformation. On Jupiter, $\beta \approx 4.5 \times 10^{-12} \text{ m}^{-1} \text{ s}^{-1}$ at midlatitudes, and the radius of deformation has been estimated in the range 500 km to 5000 km (Ingersoll and Cuong 1981). This gives a maximum Rossby wave speed, and hence an estimate of maximum vortex drift rate relative to the zonal flow, in the range of 1 m s^{-1} to 100 m s^{-1} . The peak flow velocities in Jupiter's zonal jets vary from a few tens of meters per second to over 100 m s^{-1} . Thus, if Jupiter's radius of deformation is near the lower end of the estimated range, the maximum speed at which vortices drift relative to the zonal flow is only a few percent of the mean zonal velocity. If, however, the radius of deformation is fairly large, it is possible for

vortices to drift relative to the mean zonal flow at a large fraction of the mean zonal flow velocity.

Using observations from the *Voyager* imaging experiment, it is possible to measure the mean zonal flow velocities with good latitudinal resolution by tracking individual small cloud features (Ingersoll *et al.* 1981; Limaye 1986) instead of spots. Dowling and Ingersoll (1988) measured the drift rates of the GRS and White Oval BC over the time interval between the *Voyager 1* and *Voyager 2* encounters. They obtained drift rates relative to System III of -3.49 m s^{-1} and 4.84 m s^{-1} respectively. The mean zonal flow velocities in System III at the latitudes of the peaks in the streamfunction of the GRS (about 22.5°S planetographic latitude) and the White Oval BC (about 33.5°S) as measured by Limaye (1986) are -25 m s^{-1} and -10 m s^{-1} respectively, which implies that both the GRS and BC are propagating eastward with respect to the mean zonal flow! This contrasts with the results of our model that the β effect results in westward propagation of vortices.

Using the Limaye (1986) zonal wind profile, the mean zonal flow speed is the same as the drift rate of the GRS at 23.5°S , and the same as the drift rate of White Oval BC at 34.6°S . The former is still within the latitude range of the quiescent central part of the GRS (see e.g., Fig. 2a of Dowling and Ingersoll 1989), which makes locating the latitude of the streamfunction peak somewhat difficult, so that although the GRS may be moving eastward relative to the mean zonal flow, the data are inconclusive. However, the latitude at which the mean zonal flow has the same velocity as the drift rate of White Oval BC is clearly south of the peak in the streamfunction of the White Oval BC (see e.g., Fig. 2b of Dowling and Ingersoll 1989). Thus it appears that White Oval BC propagates to the east with respect to the mean zonal flow.

There are at least two possible explanations for the eastward drift of White Oval BC. First, there is a class of known steady solutions to the quasi-geostrophic

equations on the β -plane which have eastward propagation speeds – the “dipolar modon with baroclinic rider” discussed by Flierl *et al.* (1980). However, these solutions were obtained in the absence of a mean zonal flow, and involve a dipolar structure in one of the vertical modes, which is unlikely to survive in a shear flow. Also, the numerical solutions by McWilliams and Flierl (1979) suggest that the modon with rider solutions are not stable for long periods. Another possible explanation is that the meridional gradient of the background (mean zonal) potential vorticity is negative. In general, either vertical shear or meridional curvature of the mean zonal flow, both of which create a background potential vorticity gradient, can create effects similar to those caused by meridional variations of the Coriolis parameter, such as Rossby waves (Gill 1982). The important parameter is the meridional gradient of the background potential vorticity, which reduces to β in the absence of a mean zonal flow.

To determine if potential vorticity gradients from curvature of the zonal flow have a similar effect upon vortex propagation as latitudinal gradients in the Coriolis parameter, we performed two simulations with a flow in the barotropic mode of the form

$$\psi_0(y) = -\left(\frac{U_0}{2}\right)y^2 + \left(\frac{B}{6}\right)y^3,$$

which has a meridional potential vorticity gradient of B . We performed simulations with $\alpha = 0.0$, $\lambda_1^2 = 1.0$, $\beta = 0.0$, $U_0 = 0.5$ and $B = \pm 0.3$. The trajectories of these two solutions at the cloud top level are shown in Fig. 2.29. The vortex with $B = 0.3$ propagates south and west, while the vortex with $B = -0.3$ propagates to the north and east. The drift rates (nondimensionalized by the velocity scale U) of the vortex relative to the mean zonal flow are -0.13 ± 0.03 for $B = 0.3$ and $+0.13 \pm 0.03$ for $B = -0.3$, which can be compared to the value of -0.11 ± 0.02 for the case with $\beta = 0.3$ and $B = 0$. Thus we see that a meridional potential vorticity

gradient caused by curvature of the mean zonal flow has approximately the same effect on the propagation of a vortex as does a potential vorticity gradient caused by the latitudinal variation of the Coriolis parameter. Furthermore, a negative meridional potential vorticity gradient will give vortices which propagate eastward relative to the mean zonal flow. If we allow that the eastward drift of White Oval BC is indicative of a negative mean meridional potential vorticity gradient, we have a potential test of assumptions about the zonal flow in Jupiter's interior. Consider the commonly used $1\frac{1}{2}$ -layer model, with a thin upper layer (representing the visible atmosphere) over an infinitely deep lower layer (representing the deep interior). In the quasi-geostrophic approximation, the potential vorticity in the upper layer is given by (Ingersoll and Cuong, 1981)

$$q = \nabla^2 \psi + \beta y - \lambda^2 (\psi - \psi_0), \quad (2.8)$$

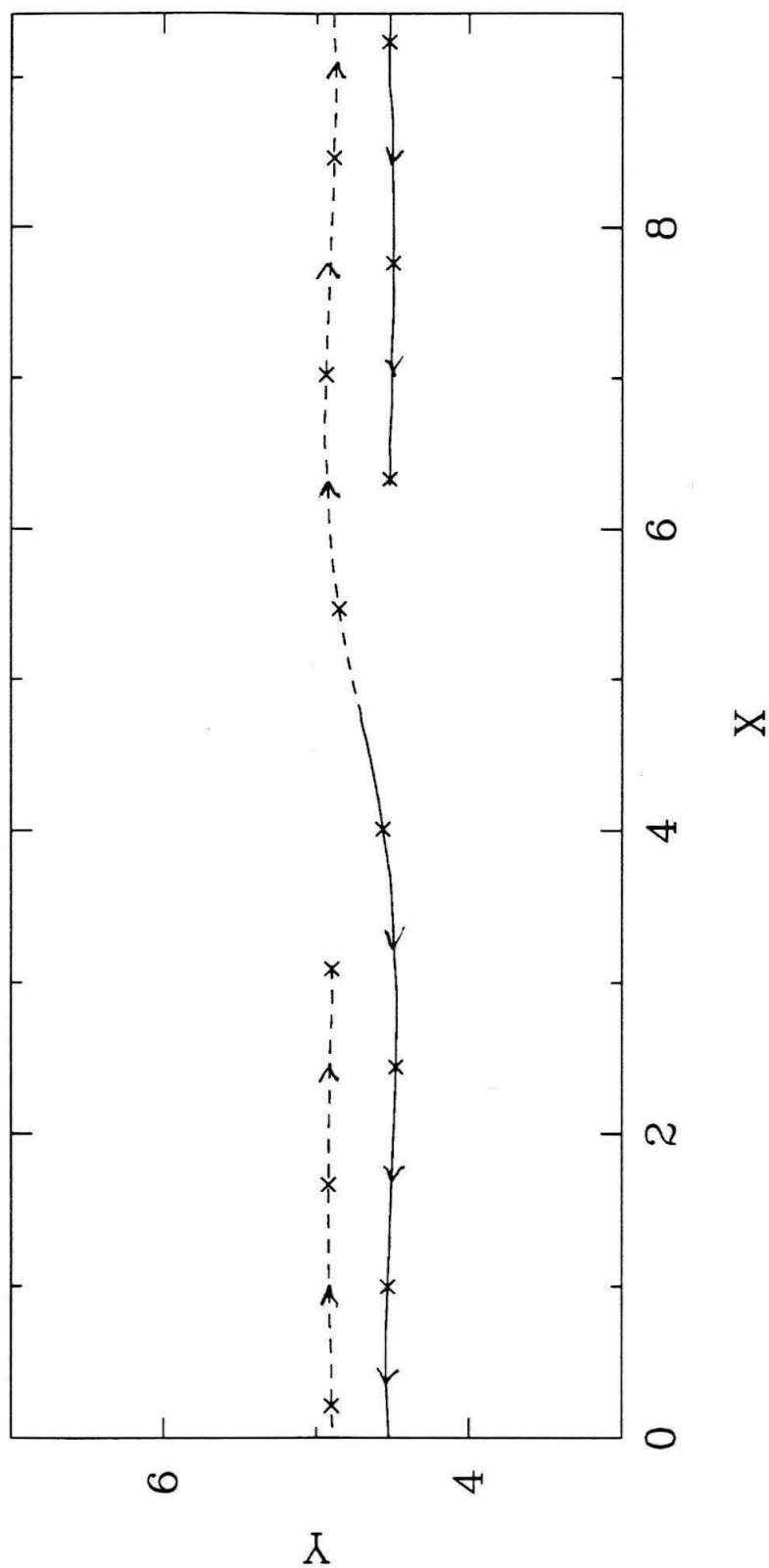
where ψ is the streamfunction in the upper layer, ψ_0 is the streamfunction in the deep interior, and λ^{-1} is the radius of deformation. The derivative in the y direction of the zonally averaged form of (2.8) gives us the zonal mean meridional potential vorticity gradient:

$$\frac{d\bar{q}}{dy} = \beta - \frac{d^2\bar{U}}{dy^2} + \lambda^2 (\bar{U} - U_0), \quad (2.9)$$

where the overbar indicates a zonal average. Since the mean zonal flow \bar{U} is observed (Ingersoll *et al.* 1981; Limaye 1986), we can make various assumptions about the flow in the deep interior $U_0(y)$, and see if they give $\bar{q}_y < 0$ at the latitude of White Oval BC. The easiest assumption to test is constant background potential vorticity, the assumption used by Marcus (1988) model of the GRS, which trivially leads to $\bar{q}_y = 0$. In this case all vortices will simply be advected by the mean flow (Marcus 1990). The eastward propagation of White Oval BC therefore indicates that the background potential vorticity is not constant in the latitude range around 33°S .

Another assumption for U_0 is that the flow in the deep interior is the same

Figure 2.29. Trajectories of vortices in a mean zonal flow with curvature. Trajectory from times $0 \leq t \leq 36.$ for vortices with $\alpha = 0.$, $\lambda_1^2 = 1.0$, $\beta = 0.0$, and $U_0 = 0.5$ with $B = 0.3$ (solid line) and $B = -0.3$ (dashed line). The crosses are at time intervals of 5.96. The two lines meet at the initial position of each vortex. The vortex with $B = 0.3$ drift westward and south from this initial position, while the vortex with $B = -0.3$ drifts eastward and north. For times $t > 36.$, the $B = 0.3$ vortex continues to drift westward at a constant rate, while the $B = -0.3$ vortex continues to drift eastward at a constant rate.



as the mean flow in the observed atmosphere, $U_0(y) = \bar{U}(y)$; this assumption was used in the model of Ingersoll and Cuong (1981). For this case, $\bar{q}_y = \beta - \bar{U}_{yy}$, which requires $\bar{U}_{yy} > \beta$ to have $\bar{q}_y < 0$. \bar{U}_{yy} has been calculated for Jupiter by Ingersoll *et al.* (1981) and Limaye (1986). Both of them find that $\bar{U}_{yy} > \beta$ in the latitude range between about 31°S and 33°S, just north of White Oval BC, with $\bar{U}_{yy} \approx \beta$ at the latitude of the center of the oval. Within the uncertainty in the data, \bar{q}_y could be of either sign given the assumption that $U_0 = \bar{U}$.

A third assumption, used by Williams and Yamagata (1984; also Williams and Wilson 1988) to study vortices on Jupiter, is solid body rotation in the interior ($U_0 = 0$), for which $\bar{q}_y = \beta - \bar{U}_{yy} + \lambda^2 \bar{U}$. This requires $\bar{U}_{yy} - \lambda^2 \bar{U} > \beta$ to get $\bar{q}_y < 0$. Since $\bar{U}_{yy} \approx \beta$ and $\bar{U} < 0$ at the latitude of White Oval BC, unless the radius of deformation is fairly large, it is likely that a model with solid body rotation in the interior has $\bar{q}_y < 0$ at the latitude of White Oval BC. Another interesting assumption for the flow in the interior was proposed by Dowling (1990): $\bar{U}(y) = \bar{q}_y(q)^{-2}$ in the shallow water equations, or $\bar{U}(y) = \lambda^{-2} \bar{q}_y$ in the quasi-geostrophic limit (the interior flow is hidden in the $\lambda^2 U_0$ term in the expression for \bar{q}_y), so that the zonally averaged meridional potential vorticity gradient is proportional to the observed mean zonal flow velocity. This assumption is based on an empirical fit to the interior flow derived by Dowling and Ingersoll (1989) from an analysis of observed vorticity, and the observation that unstable flows in a numerical shallow water model adjust to meet this criterion. This assumption gives $\bar{q}_y = \lambda^2 \bar{U}$, so that the sign of \bar{q}_y is the same as the sign of the observed zonal flow \bar{U} , which is negative at the latitude of White Oval BC. Thus this assumption for the interior flow is consistent with the observed eastward propagation of White Oval BC. In fact, the only assumption discussed above that is clearly inconsistent with the observed drift of White Oval BC is constant potential vorticity of the mean flow. The assumption that the flow in the interior is the same

as in the observed atmosphere is marginal; the data for the curvature of the mean flow are too noisy to be conclusive either way.

2.6.3 Conclusions

Numerical simulations of the non-linear stability of baroclinic Jovian vortices on the f -plane indicate that stable vortices, or vortices which appear to be stable when seen only at the level of the observed cloud deck, occur over a large range of sizes. This matches observations of Jupiter, which show vortices with diameters ranging from a few hundred kilometers to over twenty thousand kilometers, and which persist for months to centuries. The tendency of a non-zero β to cause meridional propagation and decay of vortices can be countered by a sufficiently strong mean zonal flow, allowing vortices to persist for fairly long times even in the presence of meridional potential vorticity gradients.

Horizontal fragmentation of vortices due to instabilities is only seen for vortices with diameters larger than the first internal radius of deformation. We should note, however, that vortices of any size with radial streamfunction profiles steeper than the Gaussian profiles used in our model can experience horizontal fragmentation through standard barotropic instability; the result, in the absence of a mean zonal flow, is fragmentation into dipoles, with each component of the dipole having the same vertical structure (Gent and McWilliams 1986). It is interesting to note that the radial structure used by Dowling and Ingersoll (1989) in their numerical simulations of the GRS, a squared Gaussian, was found by Gent and McWilliams (1986) to be barotropically unstable, which suggests that the mean zonal flow may suppress vortex breakup by barotropic instability.

Internal barotropic instability, which occurs for vortices smaller than the deformation radius, can only be detected from observations of cloud top motions by its effect on the position of the vortex. In the presence of a mean zonal flow, it results

in the oscillation of the position of the vortex in both latitude and longitude. This instability may explain some, but not all, observations of vortices which oscillate in longitude, in particular the Second Dark Spot on Neptune, and the oscillating vortex of 1941-42 on Jupiter. If the latter is truly an example of internal barotropic instability, it implies that the deformation radius on Jupiter is near the upper limit of the range estimated by Ingersoll and Cuong (1981), in the range of around 3000 to 5000 kilometers.

The presence of meridional potential vorticity gradients (the beta effect) results in the propagation and decay of vortices. The decay can be inhibited by a sufficiently strong zonal shear, although the vortices will drift zonally relative to the mean flow. If the deformation radius is large, the drift rate relative to the mean flow may possibly be a large fraction of the mean flow velocity, which will introduce errors when using observed vortex drift rates as estimates of the mean zonal flow velocities. The direction which vortices drift relative to the mean flow depends upon the sign of the meridional potential vorticity gradient. Thus measurements of vortex drift rates may be helpful in constraining models for the flow beneath the observed cloud layer; measurement of drift rates for a number of vortices at different latitudes would be useful.

Acknowledgements

The numerical computations for this paper were performed on the Cray Y/MP computer of the San Diego Supercomputer Center. This research was supported by the NASA Planetary Atmospheres program under grant NAGW-1956.

Appendix A: Energy in the Normal-Mode Model

To derive an energy equation in the normal-mode model, we begin with the separate vorticity and energy equations with continuous vertical structure in log-pressure

coordinates (e.g., Pedlosky 1987):

$$\frac{D}{Dt}(\nabla^2\psi + \beta y) - f_0 e^z \frac{\partial}{\partial z}(e^{-z}w) = 0, \quad (\text{A.1})$$

$$\frac{D}{Dt}\left(\frac{\partial\psi}{\partial z}\right) + f_0 L_D^2 w = 0. \quad (\text{A.2})$$

where $w \equiv dz/dt$ is the vertical velocity in log-pressure coordinates, f_0 is the Coriolis parameter, and the other variables are as defined in Section 2.2. We write the streamfunction ψ as a sum over our orthogonal modes $\Phi_n(z)$, and the vertical velocity w as a sum over the vertical derivatives of our modes:

$$\psi(x, y, z, t) = \sum_{n=0}^N \psi_n(x, y, t) \Phi_n(z), \quad (\text{A.3})$$

$$w(x, y, z, t) = \sum_{n=0}^N w_n(x, y, t) \frac{1}{L_D} \frac{d\Phi_n(z)}{dz}. \quad (\text{A.4})$$

Substituting (A.3) and (A.4) into (A.1) and (A.2), multiplying by $e^{-z}\Phi_n(z)$ and integrating over the vertical extent of the model, we obtain the normal-mode versions of the vorticity and energy equations:

$$\frac{\partial}{\partial t}(\nabla^2\psi_n) + \beta \frac{\partial\psi_n}{\partial x} + \sum_{l,m=0}^N \gamma_{lmn} J(\psi_l, \nabla^2\psi_m) = -f_0 \lambda_n^2 w_n, \quad (\text{A.5})$$

$$\lambda_n^2 \frac{\partial\psi_n}{\partial t} + \frac{1}{2} \sum_{l,m=0}^N \gamma_{lmn} (\lambda_m^2 - \lambda_l^2) J(\psi_l, \psi_m) = -f_0 \lambda_n^2 w_n. \quad (\text{A.6})$$

If we subtract the Laplacian of (A.6) from λ_n^2 times (A.5), we obtain an equation for finding the modal components of the vertical velocity w_n from the modal components of the streamfunction ψ_n :

$$f_0 \lambda_n^2 (\nabla^2 - \lambda_n^2) w_n = \lambda_n^2 \beta \frac{\partial\psi_n}{\partial x} + \sum_{l,m=0}^N \gamma_{lmn} \left[\lambda_n^2 J(\psi_l, \nabla^2\psi_m) + \frac{1}{2} (\lambda_l^2 - \lambda_m^2) \nabla^2 J(\psi_l, \psi_m) \right]. \quad (\text{A.7})$$

We can now obtain equations for the time rate of change of the kinetic and potential energy of mode n by multiplying (A.5) and (A.6) by $\psi_n dx dy$ and integrating

over the area of the domain. This gives:

$$\frac{\partial K_n}{\partial t} = f_0 \lambda_n^2 \iint \psi_n w_n dx dy + \sum_{l,m=0}^N \iint \gamma_{lmn} \nabla^2 \psi_m J(\psi_n, \psi_l) dx dy, \quad (A.8)$$

$$\frac{\partial P_n}{\partial t} = -f_0 \lambda_n^2 \iint \psi_n w_n dx dy - \frac{1}{2} \sum_{l,m=0}^N \iint \gamma_{lmn} (\lambda_m^2 - \lambda_l^2) \psi_n J(\psi_l, \psi_m) dx dy, \quad (A.9)$$

where

$$K_n = \iint \frac{1}{2} |\nabla \psi_n|^2 dx dy$$

is the kinetic energy of mode n , and

$$P_n = \iint \frac{1}{2} \lambda_n^2 \psi_n^2 dx dy$$

is the potential energy of mode n . The total energy of the model $E = \sum_{n=1}^N (K_n + P_n)$ is obtained by summing the potential and kinetic energies over all of the baroclinic modes. The time rate of change for the total energy can be calculated by summing (A.8) and (A.9) over the baroclinic modes, giving

$$\frac{dE}{dt} = \sum_{m,n=1}^N \iint \nabla^2 \psi_m J(\psi_n, \psi_0) dx dy. \quad (A.10)$$

We may split the streamfunction into zonal mean and eddy components $\bar{\psi}_n$ and ψ'_n , defined by $\bar{\psi}_n(y, t) = \int \psi_n(y, t) dx / \int dx$ and $\psi'_n(x, y, t) = \psi_n(x, y, t) - \bar{\psi}_n(y, t)$. The vertical velocity can similarly be split into mean and eddy components \bar{w}_n and w'_n . We can then define a mean kinetic energy of mode n

$$\bar{K}_n = \iint \frac{1}{2} |\nabla \bar{\psi}_n|^2 dx dy,$$

an eddy kinetic energy of mode n

$$K'_n = \iint \frac{1}{2} |\nabla \psi'_n|^2 dx dy,$$

a mean potential energy of mode n

$$\bar{P}_n = \iint \frac{1}{2} \lambda_n^2 \bar{\psi}_n^2 dx dy,$$

and an eddy potential energy of mode n

$$P'_n = \iint \frac{1}{2} \lambda_n^2 \psi_n'^2 dx dy.$$

Each of these may be summed over the baroclinic modes to give a total mean kinetic energy \bar{K} , a total eddy kinetic energy K' , a total mean potential energy \bar{P} and a total eddy potential energy P' . After a large amount of algebra similar to that used to calculate the time rate of change of the total energy, we can obtain expressions for the time rate of change of each of the mean and eddy energy terms:

$$\begin{aligned} \frac{d\bar{K}}{dt} &= \{\bar{P} \cdot \bar{K}\} - \{\bar{K} \cdot K'\} \\ \frac{dK'}{dt} &= \{P' \cdot K'\} + \{\bar{K} \cdot K'\} \\ \frac{d\bar{P}}{dt} &= -\{\bar{P} \cdot \bar{K}\} - \{\bar{P} \cdot P'\} \\ \frac{dP'}{dt} &= -\{P' \cdot K'\} + \{\bar{P} \cdot P'\} \end{aligned}$$

where

$$\{\bar{P} \cdot \bar{K}\} = \sum_{n=1}^N f_0 \lambda_n^2 \iint \bar{\psi}_n \bar{w}_n dx dy$$

is the conversion of mean potential energy into mean kinetic energy,

$$\{P' \cdot K'\} = \sum_{n=1}^N f_0 \lambda_n^2 \iint \psi_n' w_n' dx dy$$

is the conversion of eddy potential energy into eddy kinetic energy,

$$\{\bar{K} \cdot K'\} = \sum_{l,m,n=0}^N \iint \gamma_{lmn} \nabla^2 \psi_l' J(\psi_m', \bar{\psi}_n) dx dy$$

is the conversion of mean kinetic energy into eddy kinetic energy, and

$$\{\bar{P} \cdot P'\} = \sum_{l,m,n=1}^N \iint \frac{1}{2} \gamma_{lmn} (\lambda_l^2 + \lambda_m^2 - \lambda_n^2) \psi_n' J(\psi_l', \bar{\psi}_m) dx dy$$

is the conversion of mean potential energy into eddy potential energy.

References

- Achterberg, R. K. and A. P. Ingersoll, 1989: A normal-mode approach to Jovian atmospheric dynamics. *J. Atmos. Sci.* **46**, 2448–2462.
- Arakawa, A., 1966: Computational design for long-term numerical integrations of the equations of atmospheric motion. *J. Comput. Phys.* **1**, 119–143.
- Davey, M. K. and P. D. Killworth, 1984: Isolated waves and eddies in a shallow water model. *J. Phys. Oceanogr.* **14**, 1047–1064.
- Dowling, T. E., 1990: A new constraint on Jupiter's winds (abstract). *Bull. Amer. Astron. Soc.* **22**, 1065.
- Dowling, T. E. and A. P. Ingersoll, 1988: Potential vorticity and layer thickness variations in the flow around Jupiter's Great Red Spot and White Oval BC. *J. Atmos. Sci.* **45**, 1380–1396.
- Dowling, T. E. and A. P. Ingersoll, 1989: Jupiter's Great Red Spot as a shallow water system. *J. Atmos. Sci.* **46**, 3256–3278.
- Flierl, G. R., 1977: The application of linear quasigeostrophic dynamics to Gulf Stream Rings. *J. Phys. Oceanogr.* **7**, 365–379.
- Flierl, G. R., 1988: On the instability of geostrophic vortices. *J. Fluid Mech.* **197**, 349–388.
- Flierl, G. R., V. D. Larichev, J. C. McWilliams and G. M. Reznik, 1980: The dynamics of baroclinic and barotropic solitary eddies. *Dyn. Atmos. Oceans* **5**, 1–41.
- Gent, P. R. and J. C. McWilliams, 1986: The instability of barotropic circular vortices. *Geophys. Astrophys. Fluid Dyn.* **35**, 209–233.
- Gill, A. E., 1982: *Atmosphere–Ocean Dynamics*. Academic Press, New York.
- Haltiner, G. J. and R. T. Williams, 1980: *Numerical prediction and dynamic meteorology, second edition*. John Wiley and Sons.

- Hammel, H. B., R. F. Beebe, E. M. DeJong, C. J. Hansen, C. D. Howell, A. P. Ingersoll, T. V. Johnson, S. S. Limaye, J. A. Magalhães, J. B. Pollack, L. A. Sromovsky, V. E. Suomi and C. E. Swift, 1989: Neptune's wind speeds obtained by tracking clouds in *Voyager* images. *Science* **245**, 1367-1369.
- Hatzes, A., D. D. Wenkert, A. P. Ingersoll and G. E. Danielson, 1981: Oscillations and velocity structure of a long-lived cyclonic spot. *J. Geophys. Res.* **86**, 8745-8749.
- Helfrich, K. R. and U. Send, 1988: Finite-amplitude evolution of two-layer geostrophic vortices. *J. Fluid Mech.* **197**, 331-348.
- Hide, R., 1961: Origin of Jupiter's Great Red Spot. *Nature* **190**, 895-896.
- Ingersoll, A. P., 1969: Inertial Taylor columns and Jupiter's Great Red Spot. *J. Atmos. Sci.* **26**, 744-752.
- Ingersoll, A. P., R. F. Beebe, B. J. Conrath and G. E. Hunt, 1984: Structure and dynamics of Saturn's atmosphere. In *Saturn* (T. Gehrels and M. S. Matthews, eds.) pp. 195-238. University of Arizona Press, Tucson.
- Ingersoll, A. P., R. F. Beebe, J. L. Mitchell, G. W. Garneau, G. M. Yagi and J.-P. Müller, 1981: Interaction of eddies and mean zonal flow on Jupiter as inferred from *Voyager 1* and *2* images. *J. Geophys. Res.* **86**, 8733-8743.
- Ingersoll, A. P. and P. G. Cuong, 1981: Numerical model of long-lived Jovian vortices. *J. Atmos. Sci.* **38**, 2067-2076.
- Ikeda, M., 1981: Instability and splitting of mesoscale rings using a two-layer quasi-geostrophic model on an f -plane. *J. Phys. Oceanogr.* **11**, 987-998.
- Kida, S., 1981: Motion of an elliptic vortex in a uniform shear flow. *J. Phys. Soc. Japan* **50**, 3517-3520.
- Limaye, S. S., 1986: Jupiter: new estimates of the mean zonal flow at the cloud level. *Icarus* **65**, 335-352.

- Mac Low, M.-M. and A. P. Ingersoll, 1986: Merging of vortices in the atmosphere of Jupiter: an analysis of Voyager images. *Icarus* **65**, 353-369.
- Malanotte Rizzoli, P., 1982: Planetary solitary waves in geophysical flows. *Adv. Geophys.* **24**, 147-224.
- Marcus, P. S., 1988: A numerical simulation of the Great Red Spot of Jupiter. *Nature* **331**, 693-696.
- Marcus, P. S., 1990: Vortex dynamics in a shearing zonal flow. *J. Fluid Mech.* **215**, 393-430.
- Maxworthy, T. and L. G. Redekopp, 1976: A solitary wave theory of the Great Red Spot and other observed features in the Jovian atmosphere. *Icarus* **29**, 261-271.
- McWilliams, J. C. and G. R. Flierl, 1979: On the evolution of isolated, nonlinear vortices. *J. Phys. Oceanogr.* **9**, 1155-1182.
- McWilliams, J.C., P. R. Gent and N. J. Norton, 1986: The evolution of balanced, low-mode vortices on the β -plane. *J. Phys. Oceanogr.* **16**, 838-855.
- Meacham, S. P., G. R. Flierl and U. Send, 1990: Vortices in shear. *Dyn. Atmos. Oceans* **14**, 333-386.
- Meyers, S. D., J. Sommeria and H. L. Swinney, 1989: Laboratory study of the dynamics of Jovian-type vortices. *Physica D* **37**, 515-530.
- Mied, R. P., and G. J. Lindemann, 1979: The propagation and evolution of cyclonic Gulf Stream Rings. *J. Phys. Oceanogr.* **9**, 1183-1206.
- Mitchell, J. L., R. F. Beebe, A. P. Ingersoll and G.W. Garneau, 1981: Flow fields within Jupiter's Great Red Spot and White Oval BC. *J. Geophys. Res.* **86**, 8751-8757.

- Moore, D. W. and P. G. Saffman, 1971: Structure of a line vortex in an imposed strain. In *Aircraft Wake Turbulence and its Detection* (J. H. Olsen, A. Goldburg and M. Rogers, ed.) pp. 339-354. Plenum, New York.
- Nezlin, M. V., A. Yu. Rylov, A. S. Trubnikov and A. V. Khutoretskii, 1990: Cyclonic-anticyclonic asymmetry and a new soliton concept for Rossby vortices in the laboratory, oceans and the atmospheres of the giant planets. *Geophys. Astrophys. Fluid Dyn.* **52**, 211-247.
- Pedlosky, J., 1987: *Geophysical Fluid Dynamics, Second Edition*. Springer-Verlag, New York.
- Peek, B. M., 1958: *The Planet Jupiter*. Faber and Faber, London.
- Polvani, L. M., 1991: Two-layer geostrophic vortex dynamics. Part 2. Alignment and two-layer V-states. *J. Fluid Mech.* **221**, 241-270.
- Polvani, L. M., J. Wisdom, E. DeJong and A. P. Ingersoll, 1990: Simple dynamical models of Neptune's Great Dark Spot. *Science* **249**, 1393-1398.
- Read, P. L., 1986: Stable, baroclinic eddies on Jupiter and Saturn: A laboratory analog and some observational test. *Icarus* **65**, 304-334.
- Read, P. L. and R. Hide, 1983: Long-lived eddies in the laboratory and in the atmospheres of Jupiter and Saturn. *Nature* **302**, 126-129.
- Read, P. L. and R. Hide, 1984: An isolated baroclinic eddy as a laboratory analogue of the Great Red Spot on Jupiter. *Nature* **308**, 45-48.
- Reese, E. J., 1971: Recent photographic measurements of Saturn. *Icarus* **15**, 466-479.
- Reese, E. J., 1972: Jupiter: its red spot and disturbances in 1970-1971. *Icarus* **17**, 57-72.
- Reese, E. J. and B. A. Smith, 1966: A rapidly moving spot on Jupiter's north temperate belt. *Icarus* **5**, 248-257.

- Smith, B. A., L. A. Soderblom, T. V. Johnson, A. P. Ingersoll, S. A. Collins, E. M. Shoemaker, G. E. Hunt, H. Masursky, M. H. Carr, M. E. Davies, A. F. Cook II, J. Boyce, G. E. Danielson, T. Owen, C. Sagan, R. F. Beebe, J. Veverka, R. G. Strom, J. F. McCauley, D. Morrison, G. A. Briggs, and V. E. Suomi, 1979a: The Jupiter system through the eyes of *Voyager 1*. *Science* **204**, 951–971.
- Smith, B. A., L. A. Soderblom, R. Beebe, J. Boyce, G. Briggs, M. Carr, S. A. Collins, A. F. Cook II, G. E. Danielson, M. E. Davies, G. E. Hunt, A. P. Ingersoll, T. V. Johnson, H. Masursky, J. McCauley, D. Morrison, T. Owen, C. Sagan, E. M. Shoemaker, R. Strom, V. E. Suomi, J. Veverka, 1979b: The Galilean satellites and Jupiter: *Voyager 2* imaging science results. *Science* **206**, 927–950.
- Smith, B. A., L. A. Soderblom, D. Banfield, C. Barnet, A. T. Basilevsky, R. F. Beebe, K. Bollinger, J. M. Boyce, A. Brahic, G. A. Briggs, R. H. Brown, C. Chyba, S. A. Collins, T. Colvin, A. F. Cook II, D. Crisp, S. K. Croft, D. Cruikshank, J. N. Cuzzi, G. E. Danielson, M. E. Davies, E. DeJong, L. Dones, D. Godfrey, J. Gougen, I. Grenier, V. R. Haemmerle, H. Hammel, C. J. Hansen, C. P. Helfenstein, C. Howell, G. E. Hunt, A. P. Ingersoll, T. V. Johnson, J. Kargel, R. Kirk, D. I. Kuehn, S. Limaye, H. Masursky, A. McEwen, D. Morrison, T. Owen, W. Owen, J. B. Pollack, C. C. Porco, K. Rages, P. Rogers, D. Rudy, C. Sagan, J. Schwartz, E. M. Shoemaker, M. Showalter, B. Sicardy, D. Simonelli, J. Spencer, L. A. Sromovsky, C. Stoker, R. G. Strom, V. E. Suomi, S. P. Synott, R. J. Terrile, P. Thomas, W. R. Thompson, A. Verbiscer and J. Veverka, 1989: *Voyager 2* at Neptune: imaging science results. *Science* **246**, 1422–1449.

-
- Sommeria, J., S. D. Meyers and H. L. Swinney, 1988: A laboratory simulation of the Great Red Spot of Jupiter. *Nature* **331**, 689–693.
- Stevenson, D. J., 1982: Interiors of the giant planets. *Ann. Rev. Earth Planet. Sci.* **10**, 257–295.
- Williams, G. P. and R. J. Wilson, 1988: The stability and genesis of Rossby vortices. *J. Atmos. Sci.* **45**, 207–241.
- Williams, G. P. and T. Yamagata, 1984: Geostrophic regimes, intermediate solitary vortices and Jovian eddies. *J. Atmos. Sci.* **41**, 453–478.

